



Università degli Studi di Cagliari

## **DOTTORATO DI RICERCA**

Scuola di dottorato in Scienze e Tecnologie Chimiche e Farmaceutiche

Indirizzo/corso in Scienze e Tecnologie Chimiche

Ciclo XXIII

### **TITOLO TESI**

**Monoolein-based cubic liquid crystals:  
specific interactions, evolutions and applications**

Settore scientifico disciplinare di afferenza

CHIM/02 Chimica Fisica

Presentata da: Sandrina Lampis

Coordinatore Dottorato: Prof. Mariano Casu

Tutor: Prof.ssa Maura Monduzzi, Dr. Sergio Murgia

Esame finale anno accademico 2009 - 2010



# Table of Contents

LIST OF PUBLICATIONS	v
INTRODUCTION	1
1 GENERAL BACKGROUND	3
1.1 Surfactants	3
1.2 The Packing Parameter	4
1.3 Liquid Crystalline Phases	7
1.4 Liquid Crystalline Nanoparticles	10
1.5 The monoolein-water system	12
1.6 Cubic phases in nature	13
1.7 Nucleotides and nucleolipids	14
2 THEORETICAL BACKGROUND	17
2.1 Optical microscopy	17
2.2 Nuclear Magnetic Resonance (NMR)	18
2.2.1 <sup>31</sup> P Chemical Shift Anisotropy (CSA) in anisotropic LC	18
2.2.2 <sup>2</sup> H NMR Quadrupolar Splittings in anisotropic LC	20
2.2.3 NMR Relaxation	21
2.2.4 NMR Self Diffusion	23
2.3 Small Angle X-Ray Scattering (SAXS)	28
2.4 Fourier transform Infrared Spectroscopy (FT-IR)	31
2.4.1 Attenuated Total Reflection Infrared Spectroscopy (ATR-IR)	32
2.5 Transmission Electron Microscopy (TEM)	33
2.5.1 Cryo-TEM	34
3 MATERIALS AND METHODS	35
3.1 Materials	35
3.2 Synthesis of the Nucleolipids	35

3.3	Sample preparation	36
3.4	Optical microscopy	36
3.5	NMR experiments	36
3.6	SAXRD experiments	38
3.7	FT-IR experiments	39
3.8	Cryo-TEM	39
3.9	Cryo-TEM image analysis	39
3.10	Cell cultures	40
3.11	Image analysis on 3T3 cells	40
3.12	Alamar blue Assay on HeLa and HEK 293T Cells	41
3.13	Statistical Analysis	42
4	EFFECT OF NUCLEOTIDES AND NUCLEOLIPIDS ON THE PHASE BEHAVIOR OF THE MO/W SYSTEM	43
4.1	Introduction	43
4.2	Results and discussion	44
4.2.1	Pseudobinary phase diagrams	44
4.2.2	The lamellar phases	45
4.2.3	The cubic phases	50
4.3	Conclusions	54
5	TEMPERATURE- AND PRESSURE-DEPENDENT PHASE BEHAVIOR OF MO/W/XMP CUBIC PHASES	55
5.1	Introduction	55
5.2	Analysis of structural parameters	56
5.3	Results and discussion	58
5.3.1	<i>Ia3d</i> cubic phase	59
5.3.2	<i>Pn3m</i> cubic phase	62
5.4	Conclusions	68
6	HYDROLYSIS OF NUCLEOTIDES AT THE <i>Ia3d</i> CUBIC INTERFACE. PART 1	69
6.1	Introduction	69
6.2	Results and discussion	70
6.3	Conclusions	77

7	HYDROLYSIS OF NUCLEOTIDES AT THE <i>la3d</i> CUBIC INTERFACE. PART 2	79
	7.1 Introduction	79
	7.2 Results and discussion	80
	7.2.1 Mechanism of the Hydrolysis Reaction	92
	7.3 Conclusions	95
8	NANOPARTICLES FROM MO-BASED LIQUID CRYSTALS: RMULSIFIER INFLUENCE ON MORPHOLOGY AND CYTOTOXICITY	97
	8.1 Introduction	97
	8.2 Results	98
	8.2.1 Phase behavior of the bulk liquid crystalline phase	98
	8.2.2 Characterization of the lipid nanoparticles	99
	8.2.3 Biological assay	104
	8.3 Discussion	108
	8.4 Conclusions	110
	CONCLUDING REMARKS	113
	ACKNOWLEDGEMENTS	115
	REFERENCES	117



# List of Publications

This thesis is based on the following papers:

**1. Orientation and Specific Interactions of Nucleotides and Nucleolipids Inside Monoolein-Based Liquid Crystals.**

Murgia, S.; Lampis, S.; Angius, R.; Berti, D.; Monduzzi, M.  
*J. Phys. Chem. B* **2009**, 113, 9205-9215.

**2. Nucleotide Recognition and Phosphate Linkage Hydrolysis at a Lipid Cubic Interface.**

Murgia, S.; Lampis, S.; Zucca, P.; Sanjust, E.; Monduzzi, M.  
*J.A.C.S.* **2010**, 132, (45), 16176-16184.

**3. Nanoparticles from Lipid-Based Liquid Crystals: Emulsifier Influence on Morphology and Cytotoxicity.**

Murgia, S.; Falchi, A. M.; Mano, M.; Lampis, S.; Angius, R.; Carnerup, A. M.; Schmidt, J.; Diaz, G.; Giacca, M.; Talmon, Y.; Monduzzi, M.  
*J. Phys. Chem. B* **2010**, 114, 3518-3525.

**4. Temperature- and Pressure-dependent phase behavior of MO/W/XMP cubic phases.**

Lampis, S.; Murgia, S.; Mariani, P.; Monduzzi, M.  
*Manuscript*

Other paper not included in the thesis:

**1. Aerosol-OT Forms Oil-in-Water Spherical Micelles in the Presence of the Ionic Liquid bmimBF<sub>4</sub>.**

Murgia, S.; Palazzo, G.; Mamusa, M.; Lampis, S.; Monduzzi, M.  
*J. Phys. Chem. B* **2009**, 113, (27), 9216-9225.





# Introduction

Driven by hydrophobic/hydrophilic intermolecular interactions, several classes of polar lipids such as phospholipids or monoglycerides may self-assemble in water in a variety of smart nanostructured aggregates, such as micellar solution and/or different types of lyotropic liquid crystals, the lamellar, hexagonal and cubic phases being the most common.

Among these self-assembled nanostructures, the bicontinuous cubic phases possibly represent the most outstanding. These liquid-crystalline phases are constituted by curved, triply periodic non-intersecting bilayers organized to form two disjoint continuous water channels. Because of their peculiar bilayer structure which closely resembles that of cell membranes, since their discovery in the early 1980s, lipid bicontinuous cubic phases have attracted much attention, especially as biomimetics and drug delivery systems. Particularly significant also are their nanometric dispersions in water solution, known as cubosomes (the nonlamellar analogue of liposomes).

The choice of polar lipid based systems to build nanostructured architectures to entrap, protect, and release therapeutic agents with hydrophilic, lipophilic, or amphiphilic nature, appears a good strategy for two main reasons. Polar lipids such as phospholipids or monoglycerides are generally friendly towards biological membranes, and favor bioadhesion as a consequence of bilayers self-assembly properties. The liquid crystalline (LC) phases formed by polar lipids have been shown able to accommodate biologically active molecules such as vitamins, enzymes, and other proteins.

This thesis deals with investigating phase behaviour and interfacial phenomena of monoolein (MO)-based liquid crystals in the presence of nucleotides and nucleolipids, used as simple models for hydrophilic and hydrophobic drugs.

Firstly, the pseudobinary phase diagrams of the monoolein/water system in the presence of AMP, GMP, CMP and UMP nucleotides along with two different AMP-based nucleolipids (HPA and POPA) were investigated through NMR, SAXRD and optical microscopy under polarized light (chapter 4). An extended study on the *Ia3d* and *Pn3m* bicontinuous cubic phases in the presence of the four nucleotides was performed via temperature and pressure scans followed by SAXRD (chapter 5).

Then the long term stability of MO/W/XMP (HPA and POPA) systems was qualitatively evaluated by means of  $^{31}\text{P}$  and  $^2\text{H}$  NMR, SAXRD and optical microscopy under polarized light, in order to monitor possible phase transitions and modifications at the molecular level (chapter 6).

Finally, the interactions between nucleotides and the monoolein/water interface were investigated. The molecular sites involved were identified and a deeper understanding of the mechanism that drives the hydrolysis of nucleotides inside the *Ia3d* cubic phase was achieved (chapter 7).

The last chapter of this thesis (chapter 8) focuses on monoolein-based nanoparticles, obtained through fragmentation of bulk liquid crystalline phases, and stabilized by two different emulsifiers, namely, Pluronic F127 and Lauroylcholine chloride. They were investigated for structural features and for short-term in vitro cytotoxicity.

# Chapter 1

## General Background

### 1.1 Surfactants

Surfactants are amphiphilic molecules which possess a hydrophilic (water-loving) head group and a hydrophobic (water-hating) tail. The hydrophobic group in a surfactant molecule is usually a hydrocarbon chain but may be a fluorocarbon or siloxane chain. The hydrophilic group is polar and may be either ionic or nonionic. Depending on the nature of the hydrophilic head, major surfactants can be divided into anionic, cationic, catanionic, zwitterionic and nonionic classes.<sup>1,2</sup> Some examples are reported in figure 1.1.

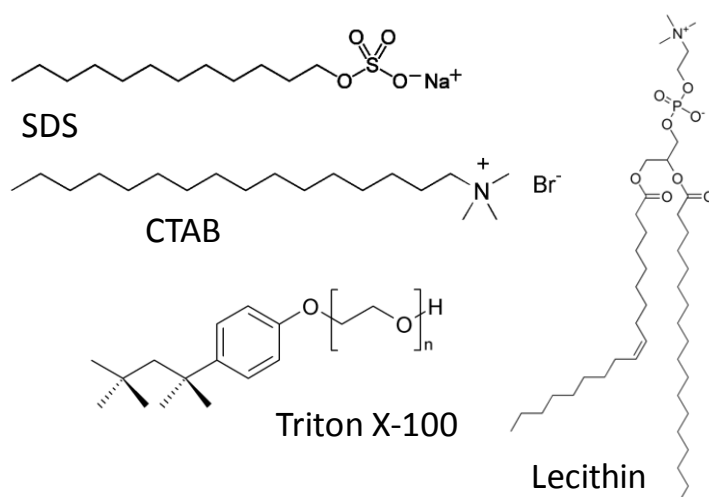
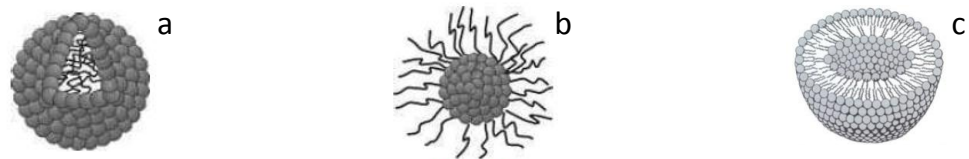


Figure 1.1 Some examples of surfactants molecules

Due to hydrophobic/hydrophilic competitions, surfactant molecules tend to migrate to interfaces or surfaces and orientate so that the polar group lies in water and the apolar group is placed out of it, and eventually in oil. In this way surfactants are able

to lower the surface tension of a liquid;<sup>3</sup> that is why the surfactant name: "**surface active agent**".

Surfactant molecules can also assemble in the bulk solution thus forming aggregates such as micelles and vesicles (see fig. 1.2). Depending on temperature, type and concentration of the solvents, there may exist direct or inverted molecular aggregates. In direct systems, the polar solvent is a continuous medium, while in the case of inverted systems, the polar solvent is confined in closed regions.



**Figure 1.2 Structure of direct (a) and inverted (b) micelles and a cross section of a liposome (c)**

The concentration at which surfactants begin to form micelles is known as the critical micelle concentration (CMC). At a concentration very close to the CMC the micelles are in general spherical. As the concentration is increased, the micelles may remain spheroidal or grow and become elongated, cylindrical or disk like. In fact, rod-like or disk-like micelles are commonly observed.<sup>4</sup> Surfactants may also form liquid crystalline phases (LC).

### **1.2 The Packing Parameter**

The self-assembly of surfactants in solutions has been widely investigated both experimentally and theoretically, because numerous practical applications take advantage of the resulting aggregates. The structure of these aggregates influences the properties of surfactant solutions, such as, for example, their solubilization capacity for hydrophobic substances or their viscous and viscoelastic properties, and consequently, the performance of surfactants in various applications. To select molecules that would yield desired structures such as spherical, globular or rodlike

micelles, or spherical bilayer vesicles, it is necessary to know how the molecular structure of the surfactant controls the shape and size of the resulting aggregate. The molecular packing parameter<sup>5</sup> allows a simple and intuitive insight into the self-assembly phenomenon. The molecular packing parameter  $P$  is defined as:

$$P = \frac{v}{al} \quad \text{eq. 1.1}$$

where  $v$  and  $l$  are the volume and the length of the surfactant tail and  $a$  is the surface area of the hydrophilic head group. The magnitude of this parameter can be estimated for simple hydrocarbon amphiphiles from molecular dimensions, by using Tanford's formulae.<sup>4</sup> For a saturated chain with  $n$  carbon atoms, volume and lengths are given by the following relationships:

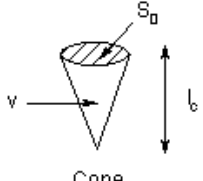
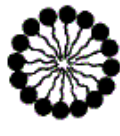
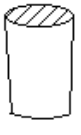
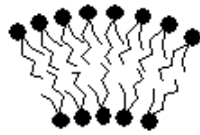
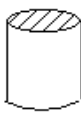
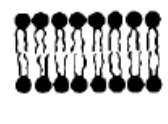
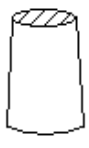
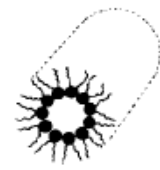
$$v = (27.4 + 26.9 n) \text{Å}^3 \quad \text{eq. 1.2}$$

$$l_{max} = (1.5 + 1.26 n) \text{Å} \quad \text{eq. 1.3}$$

while the magnitude of the head-group area depends on the amphiphile, as well as the degree of hydration and temperature. The packing parameter is related to the mean and Gaussian curvatures of the aggregate, respectively  $H$  and  $K$ , on the basis of the following equation derived from the differential geometry:<sup>6</sup>

$$\frac{v}{al} = 1 + Hl + \frac{Kl^2}{3} \quad \text{eq. 1.4}$$

Depending on the  $P$  value, different arrangements can arise from the surfactants' molecules into structured aggregates. The following table shows the expected structure for different  $P$  values.

Packing shape	Packing parameter	Phase formed	Lipid examples
 <p>Cone</p>	$< 1/3$ (spheres) $1/3 - 1/2$ (rods)		Lysophospholipids Free fatty acids
 <p>Truncated cone</p>	$1/2 - 1$ (lamellar, vesicles)		Double-chained lipids with large head group areas and fluid chains
 <p>Cylinder</p>	$\sim 1$ (lamellar, planar bilayers)		Double-chained lipids with small head group areas, anionic lipids and saturated chains
 <p>Inverted truncated cone</p>	$> 1$ (hexagonal $H_{II}$ )		Double-chained lipids with small head group areas, non-ionic lipids and polyunsaturated chains

**Table 1.1 Molecular shapes and association structures of surfactants**

Which structure is formed depends not only by the molecular structure of the lipid, in fact it is possible to affect the phase behavior by mixing different lipids, by changing the hydration level and environmental conditions, such as temperature, pressure, pH, ionic strength and by the presence of additives.

### 1.3 Liquid crystalline phases

Liquid crystals can be divided into thermotropic and lyotropic phases. The phase transitions of thermotropic liquid crystals depend on temperature, while those of lyotropic liquid crystals depend on both temperature and concentration. A brief overview of lyotropic liquid crystals will be given here.

**LAMELLAR PHASES.** In the lamellar phase, amphiphilic molecules are arranged in bilayer sheets separated by layers of water (see fig. 1.3). Different types of lamellar phases, such as  $L_\alpha$ ,  $L_\beta$ ,  $L_c$  have been observed in lyotropic mixtures. The lamellar phase is characterized by a one-dimensional periodicity. The  $L_\beta$  phase differs from the  $L_\alpha$  phase by the state of the carbonic chains. In fact, in the  $L_\alpha$  phase the hydrophobic chains are molten, while in the  $L_\beta$  phase they possess a partial crystallinity which induces long-range ordering between lamellae. The  $L_c$  phase has the chains of each surfactant molecule "frozen" into specific lattice sites and is the most ordered of the three lamellar phases.

Like all anisotropic phases, lamellar mesophases exhibit distinct optical textures, when confined in thin slabs between crossed polarizers and viewed through an optical microscope. Typically the texture is mosaic-like, often accompanied by "Maltese crosses" (see fig. 1.3).

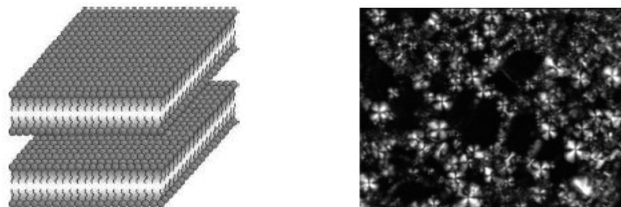
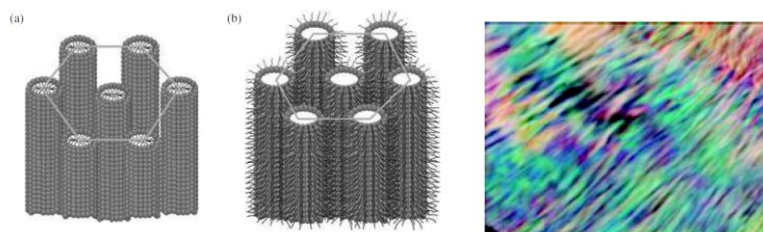


Figure 1.3 Schematic representation of a lamellar phase (left) and its typical "maltese crosses" in the polarizing microscope (right)

**HEXAGONAL PHASES.** The standard picture of a hexagonal mesophase consists of a dense packing of cylindrical micelles, arranged on a 2D hexagonal lattice (see fig. 1.4 a,b). In normal topology the hydrocarbon chains are contained within the cylindrical aggregates such that the polar-apolar interface has a direct mean curvature. Inverse topology hexagonal phases have water within the cylindrical aggregates and the hydrocarbon chains fill the voids between the hexagonally packed cylinders. Normal topology hexagonal phases are denoted by  $H_I$ , while inverse topology hexagonal phases are denoted by  $H_{II}$ . When viewed under a polarizing microscope hexagonal phases exhibit birefringence, giving rise to characteristic optical textures. Typically these textures are smoke-like, fan-like or mosaic in appearance (see fig. 1.4 c). The hexagonal phases are highly viscous.



**Figure 1.4** Schematic representation of a direct (a), and an inverted (b) hexagonal phase and their typical pattern in the polarizing microscope

**CUBIC PHASES.** Cubic phases are structures which possess three-dimensional periodicity. There are two types of molecular aggregates, micellar and bicontinuous structures: in the cubic micellar phase, micelles are packed on a cubic (face-centered or body-centered) lattice, while bicontinuous cubic structures consist of a curved bilayer lying on an Infinite Periodic Minimal Surface (IPMS).

Infinite Periodic Minimal Surface (IPMS) are surfaces entirely composed of saddle points, showing zero mean curvature. These minimal surfaces are generally located at the lipid bilayer midplane (reversed phases) or in the middle of the water layer (normal phases).



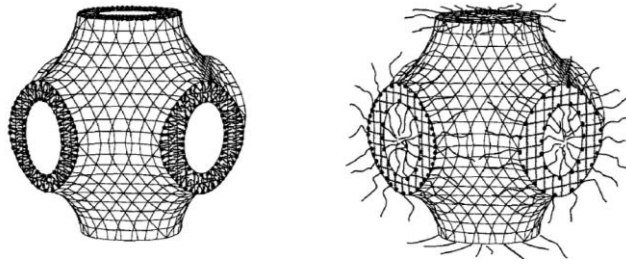


Figure 1.5 Schematic picture of one possible bicontinuous cubic phase of symmetry  $Im3m$ . (Left) A reversed and (right) a direct cubic phase

Three types of bicontinuous cubic mesophases have been identified in lyotropic mixtures, belonging to space groups  $Pn3m$ ,  $Im3m$ , and  $Ia3d$ , as sketched in figure 1.6.

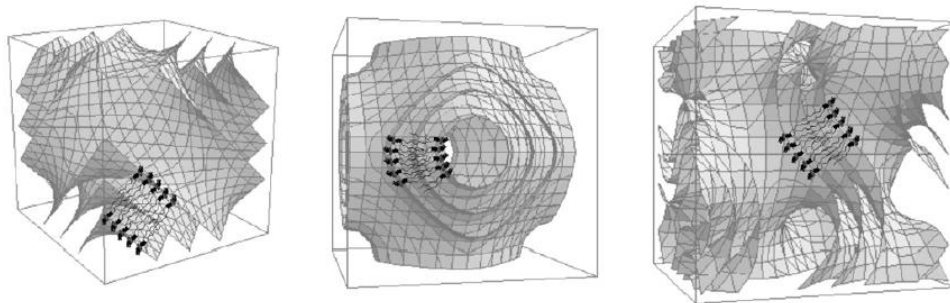


Figure 1.6 The three minimal surfaces, D, P, and G, which sit at the bilayer mid-plane and underlie the bicontinuous cubic phases  $Pn3m$ ,  $Im3m$ , and  $Ia3d$

**SPONGE PHASE ( $L_3$ ).** It consists of a spatially disordered hyperbolic amphiphilic bilayer in water, and can be viewed as a lamellar phase break-up, in which channels connect only locally ordered bilayers (see fig. 1.7). Sponge mesophases are characterized by flow birefringence (giving anisotropic optical textures) while they are isotropic at rest. Sponge phases can also be considered to be a melt of bicontinuous cubic phase.

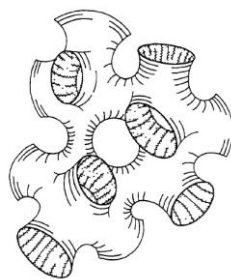


Figure 1.7 Schematic of the  $L_3$  phase (sponge) structure

**INTERMEDIATE PHASES.** There are experimental evidences of the existence of lyotropic phases with lower symmetries, which are sometimes called “intermediate phases”. Usually, they are observed in mixtures with long chain amphiphiles or amphiphiles with restricted flexibility. Examples are the rhombohedral phase and the “mesh” phase in which the lamellae present pores or holes filled up with the solvent (see fig. 1.8). These holes may or may not be correlated from one layer to the other.

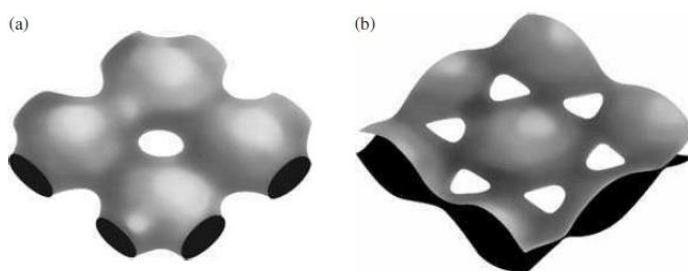


Figure 1.8 (a) sketch of one layer of the centered tetragonal mesh structure and (b) sketch of one layer of the rhombohedral mesh structure

#### 1.4 Liquid Crystalline nanoparticles

Liquid crystalline nanoparticles are receiving much attention because of their potential applications in various areas, including the formulation of functional food and drug nanocarriers.<sup>7-10</sup> The category of nanoparticulate carriers includes liposomes, cubosomes (aqueous dispersions of inverted-type bicontinuous cubic phases)<sup>11-15</sup> hexosomes (aqueous dispersions of inverted-type hexagonal phase)<sup>16,17</sup>

and dispersed sponge phases<sup>11,18</sup>. Cryo-TEM images of liposomes, cubosomes, hexosomes and dispersed sponge phase are reported in figure 1.9.

Lipid liquid crystalline nanoparticles are commonly prepared using either a bottom-up or a top-down approach. In general, a hydrophilic polymeric stabilizer is used to efficiently cover the outer surface of the dispersed particles and to retain the structures of these. The bottom-up approach is mainly accomplished by diluting and then homogenizing a liquid mixture of the emulsifier and lipid in water (nanoparticles form by nucleation in the aqueous solution),<sup>19-21</sup> while the latter implies the fragmentation of a massive LC phase in an aqueous solution of the emulsifier.<sup>22</sup> The top-down approach allows, in principle, for the entrapment of hydrophilic drugs (oligonucleotides, peptides, and proteins) that, on the contrary, cannot be easily introduced when preparing the dispersions directly from the components as previously reported.<sup>11,23,24</sup>

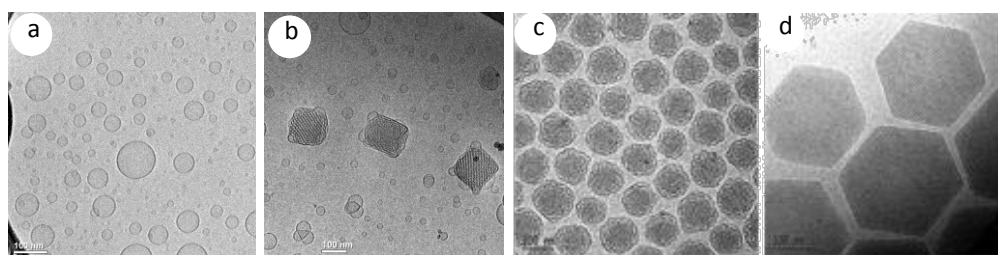


**Figure 1.9 Cryo-TEM images of liposomes, cubosomes, a dispersed sponge phase and hexosomes**

## 1.5 The monoolein (MO) - water system

Monoolein (MO), or glycerol monooleate, is a well known polar, nonionic lipid commonly used as an emulsifying agent and as a food additive since the 1950s.<sup>25</sup>

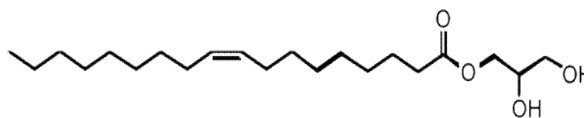


Figure 1.10 Monoolein structure

MO swells in water, giving rise to several lyotropic liquid crystalline structures,<sup>26-32</sup> as shown in its phase diagram in figure 1.11.

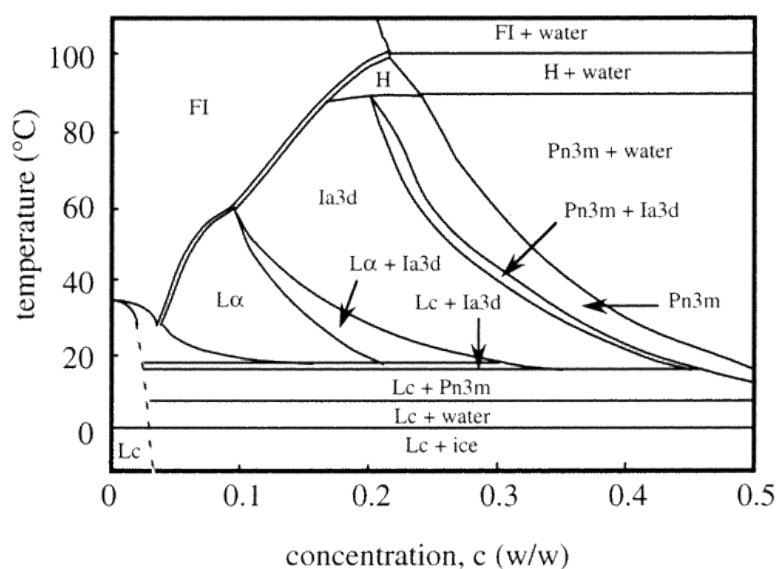


Figure 1.11 Phase diagram of the MO/W system at ambient pressure. The concentration is expressed as weight of water per weight of the mixture. Phases are labeled as given in the text. FI stands for fluid isotropic phase

Upon increasing the water content the MO/W binary system shows a small region of reverse micellar ( $L_2$ ) phase followed by a lamellar ( $L_\alpha$ ) phase, and by a  $C_G$  ( $Ia3d$  space group) and a  $C_D$  ( $Pn3m$  space group) bicontinuous cubic phase. The  $C_G$  phase evolves

towards a reverse hexagonal ( $H_{II}$ ) phase above 80 °C, whereas the  $C_D$  phase can coexist with water excess.

From a pharmaceutical standpoint, MO shows a number of interesting properties. MO is nontoxic, biodegradable, and biocompatible material classified as GRAS (generally recognized as safe), and is included in the FDA Inactive Ingredients Guide and in nonparental medicines licensed in the UK. Its biodegradability comes from the fact that monoolein is subject to lipolysis due to diverse kinds of esterase activity in different tissues.

The use of MO-based systems, in particular bicontinuous cubic and hexagonal LC phases, in the drug delivery field is reported in several works.<sup>26-32</sup> These LC phases have the potential for control over release rates, low toxicity, and versatility in application across a range of administration regimes, including oral,<sup>33</sup> transdermal,<sup>34,35</sup> and parenteral delivery.<sup>36-38</sup> An important attribute of cubic and hexagonal LC systems is that they are thermodynamically stable in excess water. This property allows for the pre-dispersion of liquid crystalline systems in aqueous vehicles in the form of sub-micron particles suitable for intravenous drug delivery.<sup>13</sup>

### **1.6 Cubic phases in nature**

Biological membranes are among the most fascinating assemblies of biomolecules: a bilayer less than 10 nm thick, composed of rather small lipid molecules that are held together simply by noncovalent forces, defines the cell and discriminates between "inside" and "outside", survival, and death. Intracellular compartmentalization, governed by biomembranes as well, is a characteristic feature of eukaryotic cells, which allows them to fulfill multiple and highly specialized anabolic and catabolic functions in strictly controlled environments.

Although cellular membranes are generally visualized as flat sheets or closely folded isolated objects, multiple observations also demonstrate that membranes may fold into "unusual", highly organized structures with 2D or 3D periodicity. The major

experimental limitations of identifying 2D periodic hexagonal or 3D periodic cubic membrane morphologies in (living) cells are caused by the dimensions of these structures and by limited analysis tools at this size range in vivo. In vitro, complex lyotropic liquid crystalline phases, i.e., lamellar, hexagonal or cubic structures, are readily amenable to a range of experimental techniques, such as Nuclear Magnetic Resonance, Small-Angle X-ray Scattering, and Differential Scanning Calorimetry. These techniques, however, are not feasible in whole cells because of limited resolution power and background noise.

Currently, the only direct way to characterize cellular membrane architecture is by transmission electron microscopy (TEM). However, deciphering the spatial architecture solely based on two-dimensionally projected TEM images is a challenging task and prone to artifacts.

Among the nonlamellar cell membranes, especially cubic membrane organizations attract great attention<sup>6,39-41</sup> because of their unique feature of 3D periodicity in TEM micrographs and great similarity to the bicontinuous lipid cubic phases.<sup>26,42-44</sup> Cubic membranes have therefore often been compared to self-assembled cubic lipid phases in aqueous dispersions that are well characterized in vitro, with several applications. Indeed, the efforts toward understanding formation and functional roles of cubic membranes in biological systems have been paralleled by the efforts in investigating cubic phases formation and their behavior in lipid-water systems.

### **1.7 Nucleotides and nucleolipids**

Nucleotides are molecules that, when joined together, make up the structural units of RNA and DNA. In addition, nucleotides play central roles in metabolism. In that capacity, they serve as sources of chemical energy (adenosine triphosphate and guanosine triphosphate), participate in cellular signaling (cyclic guanosine monophosphate and cyclic adenosine monophosphate), and are incorporated into

important cofactors of enzymatic reactions (coenzyme A, flavin adenine dinucleotide, flavin mononucleotide, and nicotinamide adenine dinucleotide phosphate).

Nucleoside and nucleotide analogues have great therapeutic potential for the treatment of viral diseases and cancer.<sup>45-48</sup> The area of nucleotide analogues has received a lot of attention due to the discovery of nucleotides with potent antiviral activities.<sup>49</sup> Nucleotides are natural substrates of transcriptase or reverse transcriptase. Accordingly, many analogs have been designed to block the enzymatic elongation of RNA chains and are utilized as anti-tumor or antiviral drugs.

Nucleolipids, are hybrid molecules composed of a nucleobase, a nucleoside, a nucleotide or an oligonucleotide (either DNA or RNA), and a lipophilic moiety, which might be either simply a single- or double-chained alkyl (or alkenyl) moiety or a carbocyclic hydrocarbon such as cholesterol, a vitamin, or a bile acid. The lipid derivatization of the phosphate group of the active nucleotide decrease the usually severe cytotoxic side-effects of nucleoside and nucleotide analogues, particularly myelotoxicity.

By direct incorporation of lipophilic prodrugs into lipid nanoparticles, it is possible to establish a slow-release drug carrier system with the following advantages: i) the efficiency of incorporation of the prodrug into the lipid bilayer matrix is quantitative due to its lipophilic property; ii) leakage into the aqueous environment is negligible, and iii) protection of the drug against metabolic degradation is improved, and longer-lasting therapeutic drug levels can be achieved.

Moreover, the inclusion of nucleoside and nucleotide analogues into drug delivery systems can constitute a promising choice to promote molecular recognition towards purine and pyrimidine receptors.

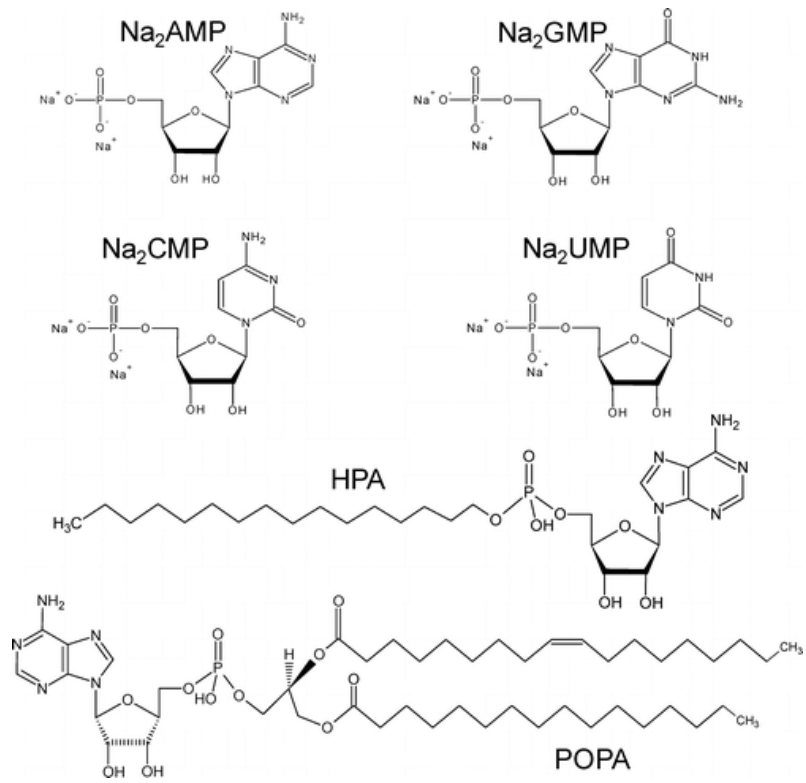


Figure 1.12 Mononucleotides disodium salts and nucleolipids



## Chapter 2

### Theoretical background

Results presented in the thesis were collected by using different techniques. In this chapter only noteworthy topic, which are essential to understand experimental data, are reported.

The structural characterization of liquid-crystalline phases was performed via optical microscopy and SAXS techniques, whereas interactions at the molecular level were studied with NMR and FTIR-ATR spectroscopy. Basic information is also given for the Cryo-TEM technique used to visualize the morphology of liquid crystalline nanoparticles.

#### 2.1 Optical Microscopy

Liquid crystals are found to be birefringent, due to their *anisotropic* nature. That is, they demonstrate double refraction (having two indices of refraction). Light polarized parallel to the director has a different index of refraction (that is to say it travels at a different velocity) than light polarized perpendicular to the director. When light enters a birefringent material, the process is modeled in terms of the light being broken up into the fast (called the ordinary ray) and slow (called the extraordinary ray) components.

Because the two components travel at different velocities, the waves get out of phase. When the rays are recombined as they exit the birefringent material, the polarization state has changed because of this phase difference.

For monochromatic light (single frequency), the magnitude of the phase difference is determined by the length and the birefringence of the material. If the sample is very thin, the ordinary and extraordinary components do not get very far out of phase. Likewise, if the sample is thick, the phase difference can be large. If the phase

difference equals 360 degrees, the wave returns to its original polarization state and is blocked by the second polarizer. The size of the phase shift determines the intensity of the transmitted light. In a typical liquid crystal, the birefringence and length are not constant over the entire sample. This means that some areas appear light and others appear dark, taken between crossed polarizers. The light and dark areas that denote regions of differing director orientation, birefringence, and length. Due to their different microscopic arrangements, every lyotropic liquid crystalline phase possesses a typical pattern under polarized light visible with the help of an optical microscope. Lamellar and hexagonal phases are birefringent, while cubic and micellar phases are optically isotropic. Lamellar phases show a typical mosaic-like texture often accompanied by "Maltese crosses" (see fig. 1.3), whereas hexagonal phases display a fan-like pattern (see fig. 1.4).

## **2.2 Nuclear Magnetic Resonance (NMR)**

### *2.2.1 <sup>31</sup>P Chemical Shift Anisotropy (CSA) in Anisotropic LC*

In molecules containing the phosphate moiety, due to the asymmetric electron distribution around the phosphorus nucleus, the <sup>31</sup>P NMR chemical shift is a tensor, generally expressed through its main components  $\sigma_{11}$ ,  $\sigma_{22}$ , and  $\sigma_{33}$ . Therefore it depends on the phosphate group orientation with respect to the external magnetic field. Particularly, the <sup>31</sup>P NMR signal may fall in a narrow range of frequencies depending on the angle ( $0^\circ \leq \theta \leq 90^\circ$ ) between the tensor and the magnetic field.

In the case of anisotropic (lamellar or hexagonal) "powder" samples consisting of randomly oriented crystalline domains, the NMR spectrum shows a feature resulting by the superimposition of the signals belonging to all the possible  $\theta$ . Typically, in liquid crystalline samples the effective chemical shift tensor is cylindrically symmetric because of the cylindrical symmetry about the normal to the surfactant aggregate, namely, the director. As a consequence, in such a kind of system the NMR spectrum consists of a broad asymmetric signal showing a high-intensity peak and a low-

intensity shoulder. The distance between the shoulder and the peak, at the extreme values of  $\theta$ , is called the chemical shift anisotropy (CSA) that, for molecules having one of the  $\sigma_{ii}$  components lying along the director, is defined as  $\Delta\sigma = \sigma_{\parallel} - \sigma_{\perp}$ , where  $\sigma_{\parallel}$  and  $\sigma_{\perp}$  represent the main components of the shielding tensor parallel and perpendicular to the director, respectively. As exemplified in the figure 2.1, for statistical reasons<sup>50</sup> and apart from shear-induced alignments,<sup>51</sup>  $\sigma_{\perp}$  shows the highest intensity and  $\sigma_{\parallel}$  the lowest, while the rule that dictates  $\Delta\sigma_{\text{lam}} \approx -2\Delta\sigma_{\text{hex}}$  always applies. It should also be remarked that for lamellar phases an upfield peak and a downfield shoulder is observed (negative  $\Delta\sigma$  values). Plainly, the opposite situation holds for hexagonal phases. Finally, in the same way as in solution, in isotropic systems such as micellar or cubic phases the CSA interaction will be averaged out and the  $^{31}\text{P}$  NMR spectrum will result in a single symmetric peak.

The  $^{31}\text{P}$  CSA is evaluated from the distance (ppm) between half-height of the shoulder and the peak of the NMR signal.

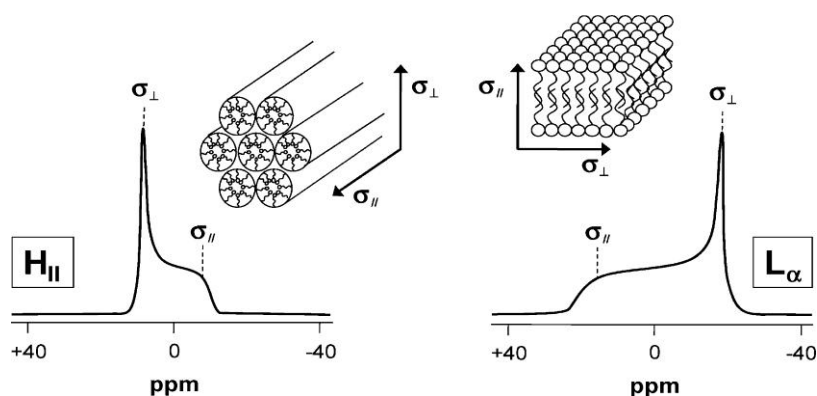


Figure 2.1  $^{31}\text{P}$  CSA in hexagonal ( $H_{II}$ ) and lamellar ( $L_{\alpha}$ ) liquid crystalline phases

### 2.2.2 $^2\text{H}$ NMR Quadrupolar Splittings in Anisotropic LC

Nuclei with a spin quantum number  $I \geq 1$ , such as  $^2\text{H}$ , have an electric quadrupolar moment that can interact with nonzero net electric field gradients giving multiple resonance of  $2I$  peaks.<sup>52</sup> If we consider the static  $^2\text{H}$  NMR spectrum of an anisotropic liquid crystalline sample prepared in heavy water these peaks would be separated by the splitting:

$$\Delta\nu_q = \frac{3}{m} P_b \chi S_b \quad \text{eq. 2.1}$$

where  $m = 4$  and  $8$  for the lamellar and hexagonal phase, respectively.  $P_b$  is the fraction of the observed nucleus in the bound state,  $\chi$  is the quadrupolar coupling constant, and  $S_b = 1/2(3 \cos^2 \theta_D - 1)$  is the order parameter related to the average time orientation ( $\theta_D$ ) of the nucleus with respect to the surfactant chain axis. For water molecules,  $P_b$  is linearly dependent on the surfactant/water (S/W) molar ratio, and on the number of bound water molecules per polar head  $n_b$ . Then eq 2.1 can be rewritten as<sup>52</sup>

$$\Delta\nu_q = \frac{3}{m} n_b \frac{S}{W} \chi S_b \quad \text{eq. 2.2}$$

Lamellar and hexagonal phases are uniaxial phases with a symmetry axis (usually called the director) that lie along the cylinder-axis in  $H_{II}$  phases while it is perpendicular to the bilayer planes in  $L_\alpha$  phases. It is possible to demonstrate that the  $\theta_D = 90^\circ$  orientation of the director axis with respect to the main magnetic field would have a splitting of one-half that obtained at the  $\theta_D = 0^\circ$  orientation. Furthermore, the intensity of the  $\theta_D = 90^\circ$  peak would decline steadily to the  $\theta_D = 0^\circ$  peak which would have the least intensity.

Conversely, if a phase is isotropic (cubic or micellar), on the relevant NMR timescale, static quadrupolar interactions are averaged to zero by molecular motion ( $S_b = 0$ ) and the spectrum, from equation 2.2, would have a single resonance. However, it should

be possible to distinguish between diverse phases taking into account their different rheological properties. Indeed,  $L_2$  phases possess a low viscosity, while cubic phases are characterized by a high stiffness.

Finally, it is worth noticing that the observation of different quadrupolar splittings or the superimposition of an isotropic and an anisotropic signal leads to identify multiphase systems.

### 2.2.3 NMR Relaxation

Nuclear magnetic resonance relaxation is a powerful tool for study surfactant aggregation in both liquid solutions and liquid crystalline phases. The experiment yields information on the local dynamics and the conformational state of the hydrocarbon chain of the amphiphile and on its polar head.

When a RF pulse is applied to a spin system the state of the spins is perturbed away from equilibrium distribution. The term relaxation describes several processes by which nuclear magnetization return to the thermal equilibrium. Phenomenologically, relaxation is categorized into:

1. Longitudinal relaxation (or  $T_1$  relaxation) that describes the return of the z-component of longitudinal z-magnetization to its equilibrium value. The corresponding time constant of that process is called  $T_1$ .
2. Transverse relaxation (or  $T_2$  relaxation) that describes the decay of transverse relaxation (x, y) magnetization. Analogously, the corresponding time constant is called  $T_2$ .

The common NMR methods for measuring  $T_1$  and  $T_2$  are, respectively, the *inversion recovery* and the *Carr Purcell Meiboom Gill Spin Echo* (CPMGSE) sequences.

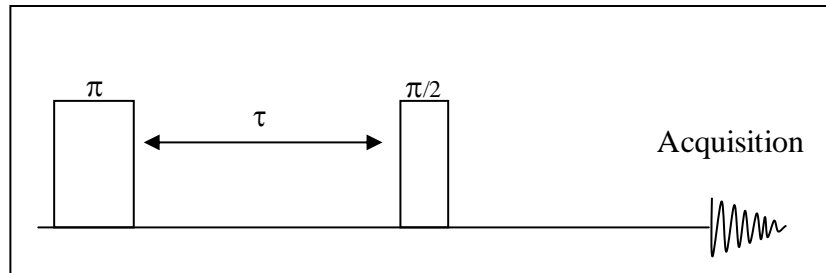


Figure 2.2 The inversion recovery NMR pulse sequence for measuring  $T_1$

In the inversion recovery sequence (fig. 2.2), magnetization is inverted by the application of a  $180^\circ$  pulse. A delay follows during which  $T_1$  relaxation takes place bringing the  $-z$  magnetization back towards  $+z$ . Afterwards a  $90^\circ$  pulse along  $y$  turns the magnetization onto the  $x$  axis into observable signal.

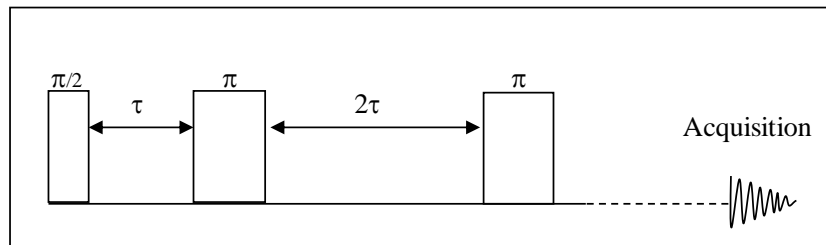


Figure 2.3 The CPMGSE NMR pulse sequence for measuring  $T_2$

In the CPMGSE sequence after the  $90^\circ$  pulse,  $180^\circ$  pulses are applied during the  $T_2$  relaxation delay equally spaced by delay periods.

For both experiments, the inversion recovery and the CPMGSE sequence, a set of spectra is recorded with different relaxation periods. The intensities of the remaining signal is measured and plotted against the relaxation delay. Mostly these plots yield decaying exponentials and by fitting procedures it is possible to extract the time constants for the decay.

The  $T_1$  and  $T_2$  relaxation times are obtained by a three-parameter (for  $T_1$ , equation 2.3) and by a two-parameter (for  $T_2$ , equation 2.4) non-linear fit of the partially relaxed NMR signal intensities obtained at 14–18 different  $\tau$  values:

$$I(t) = A - B \exp(-\tau T_1^{-1}) \quad \text{eq. 2.3}$$

$$I(\tau)_{echo} = C \exp(-\tau T_2^{-1}) \quad \text{eq. 2.4}$$

#### 2.2.4 NMR self-diffusion

Molecular motion is usually partitioned into internal motions (rotation about bonds and vibration) and overall reorientation and translational diffusion. The latter can be further divided into self-diffusion and mutual diffusion.

In a non-equilibrium two-component system, *mutual diffusion* is characterized by the relaxation of concentration gradients according to Fick's law:

$$J = D_m \times \frac{dc}{dx} \quad \text{eq. 2.5}$$

where  $dc/dx$  is the solute concentration gradient,  $D_m$  is the mutual diffusion coefficient and  $J$  represents the flow of solute molecules per unit cross section area.

Differently, *self-diffusion* is the net result of the thermally induced random-walk (Brownian) motions experienced by molecules in solution. (Please note that the following discussion pertains either to molecules, particles or molecular aggregates, e.g. micelles).

In an isotropic system, in the absence of either thermal or concentration gradients, the average molecule displacement in all three directions is zero, but the mean square displacement is non-zero, as stated by the Einstein equation:

$$\langle r^2 \rangle = 6Dt \quad \text{eq. 2.6}$$

where  $D$  is the so-called self-diffusion coefficient.

Since  $D$  is strongly influenced by the molecular size, the viscosity  $\eta$  of the solvent and the temperature  $T$ , its magnitude is formally given by the Stokes-Einstein relation:

$$D = \frac{K_B T}{6\pi\eta R_H} \quad \text{eq. 2.7}$$

where  $K_B$  is the Boltzmann constant and  $R_H$  represents the hydrodynamic radius of the molecule.

It is worth noticing that equation 2.7 is valid only for rigid, spherical molecules, whereas for other geometries more complex equations describe  $D$ . In addition, real molecules are subjected to tumbling motions and are often hydrated/solvated. Therefore, the radius calculated from the diffusional properties of a molecule is indicative of the *apparent* size of the dynamic hydrated/solvated molecule (see Figure 2.4).

Despite these limitations, as evidenced by the huge number of papers devoted to self-diffusion coefficients measurement, an appropriate use of  $D$  may be very useful in solving different problems, ranging from clarifying the inner structure of colloidal systems<sup>53,54</sup> to the discrimination of complexes or molecular aggregates size.<sup>55</sup> In all these cases the concept that underpins the study of the self-diffusion coefficient is based on the simple observation that the self-diffusion coefficient of a molecule is altered by a specific interaction with another molecule or by a restriction of the molecular displacement.



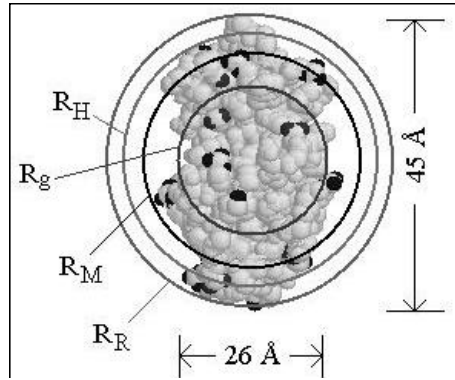


**Figure 2.4 Comparison between different radius of the lysozyme that, from crystallographic structure, is described by an ellipsoid.  $R_M$  represents the equivalent radius of a sphere with the same mass and particle specific volume as lysozyme**

The possibility to label a nuclear magnetic moment (spin) with respect to its position via its precessional frequency allows for the measurement of the self-diffusion coefficient through NMR experiments. In such experiments a linear magnetic-field gradient ( $g_z$ ) is introduced, so that the fundamental NMR equation becomes:

$$\omega(z) = \gamma(B_0 + g_z z) \quad \text{eq. 2.8}$$

where  $B_0$  is the strength of the applied magnetic field and  $\gamma$  is the gyromagnetic ratio. Here, the precessional frequency of the nuclei ( $\omega$ ) depends on their position ( $z$ ). Self-diffusion experiments are based on the pulse sequence of the spin-echo (SE) in which an initial  $\pi/2$  ( $90^\circ$ ) pulse turns the magnetisation of the  $z$ -direction of the static  $B_0$  field into the  $x$ - $y$  plane and creates phase coherence. Subsequently, spins dephase during a time  $\tau$ . One reason for dephasing is an inhomogeneity of the magnetic field. Application of a  $\pi$ -( $180^\circ$ ) inversion pulse reverses the dephasing effect, and the spin phases begin to cluster again. Thus, at time  $2\tau$ , the so-called Hahn spin-echo is observed in signal acquisition. A proper formation of this echo is bound to the constancy of the precession frequency for every spin in the time interval  $2\tau$ . If the nuclei are displaced from their original locations in the inhomogeneous field, their

frequencies vary, and this effect can be monitored *via* the attenuation of the spin-echo signal.

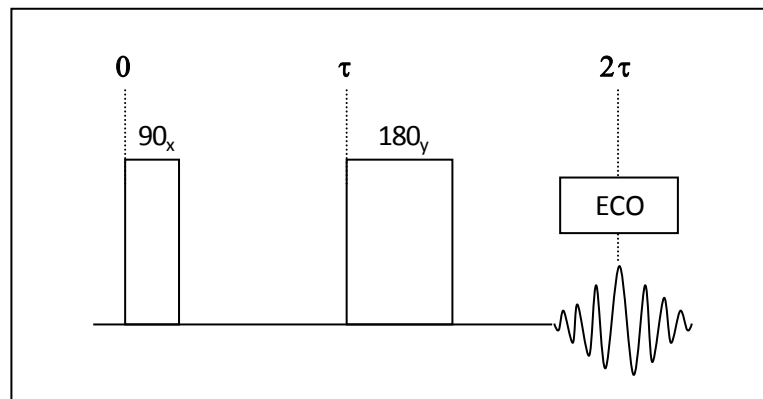


Figure 2.5 The spin-echo experiment

In the original pulsed gradient spin echo (PGSE) NMR sequence, developed by Stejskal and Tanner in 1965, in which the strength of the pulse is increased in successive experiments, the signal attenuation can be described using equation 2.9:

$$A(\delta, \Delta, g, \tau) = A_0 e^{\left(-\frac{2\tau}{T_2}\right)} e^{\left[-(\gamma g \delta)^2 D \left(\Delta - \frac{\delta}{3}\right)\right]} \quad \text{eq. 2.9}$$

where  $A_0$  is the echo signal intensity for  $g=0$ ,  $T_2$  is the spin-spin relaxation time,  $\gamma$  is the magnetogyric ratio,  $g$  is the gradient strength, and  $D$  is the self-diffusion coefficient. The times  $\tau$ ,  $\Delta$  and  $\delta$  are defined in figure 2.6.

From equation 2.9 it is evident that the experiment is easier to perform if  $T_2$  is longer and  $D$  is faster. If this is not the case,  $\Delta$  must be optimized by searching for a compromise between minimizing the  $T_2$  effect (short  $\Delta$ ) and maximizing the decay due to  $D$  (long  $\Delta$  and  $\delta$ ).

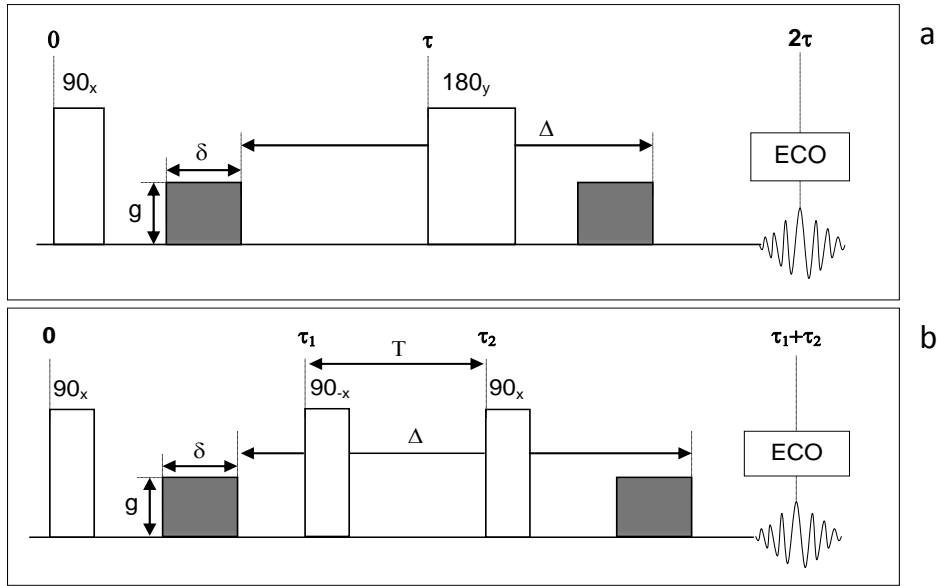


Figure 2.6 Schematic representation of PGSE (a) and PGSTE (b) pulse sequences

If the sample under study contains nuclei with short  $T_2$  the stimulated echo experiment, shown in figure 2.4b, is required. Here, the particular sequence gives the experiment a dependence on  $T_1$ , which is always longer than or equal to  $T_2$ . The pulsed gradient stimulated echo (PGSTE) sequence consists of three  $90^\circ$  pulses. Two magnetic field gradients of amplitude  $g$  and duration  $\delta$  are used to “encode” diffusion.

For the PGSTE sequence the correlation between signal attenuation and self-diffusion coefficient is described by the following equation:

$$A(\delta, \Delta, g, \tau_1, T) = A_0 e^{\left[ \left( -\frac{\tau_1}{T_2} \right) - \left( \frac{T}{T_1} \right) \right]} e^{\left[ -(\gamma g \delta)^2 D \left( \Delta - \frac{\delta}{3} \right) \right]} \quad \text{eq. 2.10}$$

where  $g$  is the (variable) magnetic-field gradient,  $\delta$  and  $\Delta$  are the time length and distance of the two magnetic-field gradients, while  $\tau_1$  and  $T$  are the constant times between the first and the second, and the second and the third  $90^\circ$  pulse, respectively.  $T_1$  is the longitudinal relaxation time.

The PGSE and PGSTE experiments are carried out by varying the gradient strength ( $g$ ) while keeping the gradient pulse length ( $\delta$ ) and the pulse intervals ( $\Delta$ ) constant. For such a case, the echo intensity decay as the value of  $g$  is increased is given by:

$$A(\delta, \Delta, g) = A_0 e^{-\gamma g \delta^2 D \left( \Delta - \frac{\delta^2}{3} \right)} \quad \text{eq. 2.11}$$

In this way a semilogarithmic fit of  $A$  versus  $g$  gives a slope that yields  $D$ .

### 2.3 Small angle X-Ray Scattering (SAXS)

Small-angle X-ray (SAXS) diffraction technique gives essential information on the local ordering and structure of colloidal systems on a scale from 1 to 100 nm.

X-rays are electromagnetic waves with wavelengths of typically few Ångstroms, that can be generated by accelerating electrons towards a metal target (anode) where the kinetic energy possessed by the electrons are converted to quanta of radiation. When reaching certain critical energies an electron in the metal K-shell is excited which causes electrons from the outer shells to jump and fill the void. This results in high intensity spikes of radiation with well defined wavelengths. The Copper-K $\alpha$  ( $\lambda=1.542$  Å) is one of the more common wavelength used.

The basic principle of X-ray diffraction techniques is that an electron present in the path of a X-ray will start to oscillate with same frequency and amplitude as the original beam. The electron is said to scatter radiation. Periodical electron density fluctuations within the sample may thus give rise to constructive interferences in certain discrete angles that appears on the detector as a scattered X-ray beam and thereby giving a diffraction pattern.

In a typical SAXS experiment a monochromatic beam of incident wave vector  $k_i$  is selected and falls on the sample. The scattered intensity is collected as a function of the so-called scattering angle  $2\theta$ . Elastic interactions are characterized by zero energy transfers, such that the final wave vector  $k_f$  is equal in modulus to  $k_i$ . The relevant parameter to analyze the interaction is the momentum transfer or scattering vector

$q = k_f - k_i$ , defined by  $q = (4\pi/\lambda) \sin\theta$ , and  $\theta$  is half the scattering angle. The standard unit for  $q$  is  $\text{\AA}^{-1}$ .

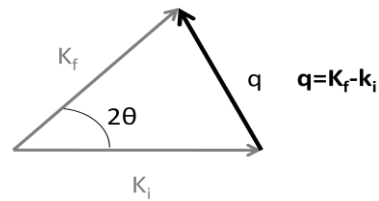


Figure 2.7 schematic representation of the scattering vector

If the scattering object has an ordered structure constructive interference of the outcoming X-rays may occur, giving rise to peaks in the scattering profile as described by Bragg's Law:

$$n\lambda = 2d \sin\theta \quad \text{eq. 2.12}$$

where  $n$  is an integer,  $\lambda$  is the wavelength of the incoming X-rays,  $d$  is the lattice spacing and  $\theta$  is the angle between the incoming X-rays and the scattering planes.

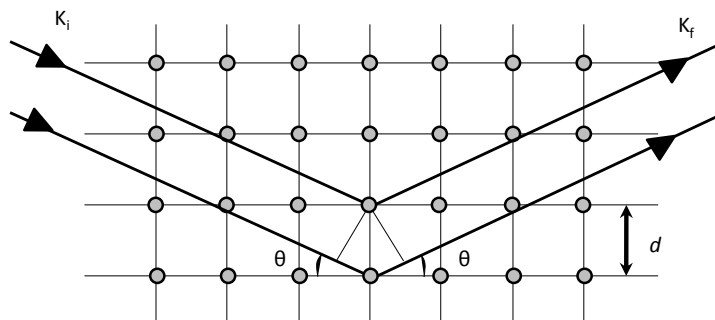


Figure 2.8 Bragg's description of diffraction

Peaks can arise also from non crystalline structures, such as microemulsions and micellar systems, but in this case, broad peaks are commonly observed.

Small angle X-ray scattering (SAXS) is the most recognized method to study the structural features of liquid crystalline mesophases, both in their bulk or dispersed form. There are two regions of the diffraction pattern that are used to identify the

phase structure. The small angle region identifies the symmetry and long range organization of the phase, whereas the wide angle region gives information on the molecular packing.

Expected diffraction patterns may be calculated using the Miller indices:

Phase		Space Group	Miller indices	Ratios
Lamellar	$d = \frac{2\pi}{q} = \frac{a}{\sqrt{h^2}}$		100 200 300 400	1 2 3 4
Hexagonal	$d = \frac{2\pi}{q} = \frac{1}{\sqrt{\frac{4}{3a^2}(h^2 + k^2 + hk)}}$		100 110 200 210 220 300	1 $\sqrt{3}$ 2 $\sqrt{7}$ $\sqrt{12}$ 3
Cubic	$d = \frac{2\pi}{q} = \frac{a}{\sqrt{h^2 + k^2 + l^2}}$	<i>Ia3d</i>	211 220 321 400 420 332	$\sqrt{6}$ $\sqrt{8}$ $\sqrt{14}$ 4 $\sqrt{20}$ $\sqrt{22}$
		<i>Pn3m</i>	110 111 200 211 220 221	$\sqrt{2}$ $\sqrt{3}$ 2 $\sqrt{6}$ $\sqrt{8}$ 3
		<i>Im3m</i>	110 200 211 220 310 222	$\sqrt{2}$ 2 $\sqrt{6}$ $\sqrt{8}$ $\sqrt{10}$ $\sqrt{12}$

## 2.4 Fourier transform infrared spectroscopy (FTIR)

Infrared spectroscopy is based on the interaction of electromagnetic radiation (0.78-1000  $\mu\text{m}$ ) with the molecules' electric dipoles, and the resulting absorption at particular energies. Molecular vibrations in the sample are excited as result of IR absorption at characteristic frequencies which are determined by the properties of the atomic molecular bonds in a sample, with their unique spatial orientations. Hence the sample has unique absorption spectra. This technique is advantageous for its being non-invasive, and enabling to get direct information on bond orders, electrostatic interactions, H-bonding, charge distributions, protonation states, redox states, dynamics and kinetics.

Radiations produced after absorption results in transitions among the vibrational energy levels within a single electronic state, that can be studied by the infrared spectroscopy. Though the region which could be investigated covers the range between 14000 and 20  $\text{cm}^{-1}$ , the mid-infrared region, 200 to 4000  $\text{cm}^{-1}$ , is used for biological materials.

An infrared spectrum is the plot of radiation absorption as a function of wavenumber or frequency ( $\nu \sim 1/\lambda$ , where  $\nu$  is frequency and  $\lambda$  is wavelength). Excited molecular vibrations in a sample give unique absorption bands at almost exactly the same position in varying type of sample possessing the same group in their structure, so called the group frequencies. Therefore, absorption spectra of the compounds are characterized by the functional groups of the molecules. They are sensitive to any environmental changes or the changes in the structures and conformations of the molecules within. Those frequencies are also further characterized by the motions of the nuclei; which are mainly the twisting, bending, rotating and asymmetric/symmetric stretching modes.

Each vibrational modes of a molecule is associated with a characteristic frequency of the vibration. For example the characteristic frequency for the symmetric stretching mode of  $\text{CO}_2$  is at 1288  $\text{cm}^{-1}$  and for the bending mode is at 667  $\text{cm}^{-1}$ , but much

higher for the asymmetric stretch mode, which is at  $2349\text{ cm}^{-1}$ . The energy levels of the vibrational modes are quantized and approximated by the energy expression for the quantum mechanical simple harmonic oscillator. The vibrational frequency,  $\nu_{\text{vib}}$ , is given by the equation:

$$\nu_{\text{vib}} = \frac{1}{2\pi} \sqrt{\frac{k}{\mu}} \quad \text{eq. 2.13}$$

where  $k$  is the force constant of the bond under question and  $\mu$  is the reduced mass of the molecule possessing this bond. The reduced mass is:

$$\frac{1}{\mu} = \frac{1}{M_1} + \frac{1}{M_2} \quad \text{eq. 2.14}$$

Where  $M_1$  and  $M_2$  are the atomic masses of two molecules connected through this bond.

#### 2.4.1 ATR-IR (Attenuated total reflection infrared spectroscopy)

In contrast to transmission IR (T-FTIR) spectroscopy where the IR beam passes directly through the sample, in the ATR mode the IR radiation is reflecting through the internal reflection element (IRE), an IR transparent crystal of high refractive index in contact with the sample. The IR radiation propagates through the IRE at an angle of incidence ( $\theta$ ) larger than the critical angle, such that total reflection occurs at the IRE-sample interface. An evanescent electromagnetic field is generated that penetrates into the sample and is attenuated by the sample, thus producing an IR spectrum. The amplitude of the electric field decays exponentially with the distance from the IRE.

The penetration depth ( $d_p$ ) is the distance from the interface where the intensity of the electric field falls to  $1/e$  of its original value at the interface:

$$d_p = \frac{\lambda_1}{2\pi \sqrt{\sin^2 \theta - n_{21}^2}} \quad \text{eq. 2.15}$$



where  $\lambda_1 = \lambda/n_1$  is the wavelength in the denser medium,  $\lambda$  the wavelength of the incoming radiation and  $n_{21} = n_2/n_1$  (where  $n_1$  is the index of refraction of the IRE,  $n_2$  is the index of the sample). The above equation holds for a two-phase system (IRE/sample). Typically,  $d_p$  is on the order of 1  $\mu\text{m}$ . For bulk materials, the degree of coupling between the evanescent field and the absorbing sample is given by the effective thickness

$$d_e = \frac{n_{21} E_0^2 d_p}{2 \cos \theta} \quad \text{eq. 2.16}$$

where  $E_0$  is the amplitude of the electric field at the interface. The effective thickness expresses the equivalent path length in a hypothetical transmission measurement, which yields the same absorption as in an ATR experiment. The very short path length used in ATR-IR spectroscopy, implicit in  $d_e$ , makes this technique surface sensitive and, hence, suitable for the in situ characterization of heterogeneous catalysts. The sensitivity can be enhanced by using multiple reflection elements. The effective thickness depends on the refractive indices of IRE and sample. For example, by increasing or decreasing  $n_1$  at constant  $\lambda_1$  and  $n_2$ ,  $d_e$  decreases or increases, respectively. Hence, by changing from Ge ( $n_1=4.0$ ) to ZnSe ( $n_1=2.4$ ),  $d_e$  increases, i.e., more sample is probed by the IR radiation.

## 2.5 Transmission Electron Microscopy (TEM)

Considering that light microscopes have limited image resolution that is imposed by the wavelength of visible light, transmission electron microscopy (TEM) is the only technique that provides nanometer-scale resolution real-space images of three-dimensional objects.

Transmission Electron Microscopy (TEM) is a well known technique for imaging solid materials at atomic resolution. Structural information can be acquired both by (high resolution) imaging as well as by electron diffraction.

The design of a transmission electron microscope (TEM) is analogous to that of an optical microscope. In a TEM high-energy (>100 kV) electrons are used instead of photons and electromagnetic lenses instead of glass lenses. The electron beam passes an electron-transparent sample and a magnified image is formed using a set of lenses. This image is projected onto a fluorescent screen or a CCD camera.

### *2.5.1 Cryo-TEM*

The application of TEM to direct visualization of colloidal nanostructures requires rapid vitrification of the samples, and so the technique is referred to as cryogenic TEM or Cryo-TEM.

Cryo-TEM is frequently used to study morphology, size and size distribution of dispersed self-assembly structures. Nowadays, fast Fourier transforms (FFTs) of Cryo-TEM images are often used to get a precise determination of interplanar distances and angles between crystallographic planes.

For the Cryo-TEM specimens are prepared without chemical treatment such as fixation, dehydration and resin embedding which can potentially cause artifacts. Samples are immersed quickly into liquid ethane at its freezing point and then stored in liquid nitrogen and transferred to a TEM. Due to the fast cooling rates occurring during this process the water in the sample is vitrified. Through the vitrification, supramolecular structures such as cubosomes and liposomes are better preserved because the rearrangement of water molecules during formation of ice crystals is mostly prevented.

# Chapter 3

## Materials and methods

### 3.1 Materials

Monoolein (MO, 1-monooleoylglycerol, RYLO MG 90-glycerol monooleate; 98 wt % monoglyceride, also containing 8 wt % of 2-monooleoylglycerol and 5 wt % of monolinoleoylglycerol as ascertained through a quantitative  $^{13}\text{C}$  NMR analysis) was kindly provided by Danisco Ingredients, Brabrand, Denmark. Distearoylphosphatidylcholine (DSPC), the mononucleotides AMP, CMP, GMP, UMP, and the D-ribose-5-phosphate disodium salt dihydrate ( $\geq 99.0\%$ ) are from Sigma whereas 2'-deoxyadenosine 5'- monophosphate, disodium salt (dAMP) is from MP Biomedicals.  $^2\text{H}_2\text{O}$ , purchased from Cambridge Laboratory, Inc. with a purity of 99.9%, was used to prepare all LC samples.

Lauroylcholine chloride and Pluronic F127 (PEO<sub>99</sub>-PPO<sub>67</sub>-PEO<sub>99</sub>), used to prepare monoolein-based nanoparticles, were from Sigma. Distilled water, passed through a Milli-Q water purification system (Millipore), was used to prepare dispersed systems.

### 3.2 Synthesis of the Nucleolipids

1-Palmitoyl-2-oleoyl-sn-glycero-3-phosphocholine and hexadecylphosphocholine were purchased from Avanti Polar Lipids (Alabaster, AL) and their purity checked by thin-layer chromatography (TLC). The lipids were used as received since no oxidation or lyso products could be detected. HCl,  $\text{CHCl}_3$ , MeOH, and  $\text{NH}_3$  (33% aqueous solution) used in the synthesis were purchased from Fluka (Buchs, Switzerland). Phospholipase D from *Streptomyces* sp AA586 was a generous gift from Asahi Chemical Industry Co., Ltd. (Tokyo, Japan). The 1-palmitoyl-2-oleoyl-sn-glycerol-3-

phosphoadenosine (POPA) and the hexadecylphosphoadenosine (HPA) were synthesized starting from the corresponding phosphatidylcholine in a two-phase system according to a modification of the method proposed by Shuto and co-workers, and obtained as an ammonium salt. Separation from the byproduct was achieved by silica-gel flash chromatography. Purity was checked by TLC,  $^1\text{H}$  and  $^{31}\text{P}$  NMR, and elementary analysis.

### 3.3 Sample Preparation

LC samples were prepared by weighing the components into glass tubes that were homogenized by repeated cycles of centrifuging back and forth at 3000 rpm at 25 °C. Homogeneous samples (by visual inspection) used for the phase diagrams characterization were stored at 25 °C in the dark for 2 days before any measurement was taken.

**CHAPTER 6.** LC dispersions were prepared by adding into a water solution of PF127 or LCh an appropriate amount of cubic phase (MO/W = 70/30), which is subsequently fragmented by an Ultra-Turrax T10 (IKA), equipped with a S10N-5G dispersing tool, working at 30.000 rpm for 20 min. In all experiments, the total dispersed phase (LC + emulsifier) was 5 wt %, with 6 wt % of PF127 or LCh with respect to MO/W weight. The sample volume was usually 2.5 mL.

### 3.4 Optical Microscopy

Liquid crystalline phases were observed through the optical microscope Zeiss Axioplan II in polarized light, at 25 °C. The observed patterns were compared with the typical textures of liquid crystals formed by other surfactants.

### 3.5 NMR Experiments

$^1\text{H}$ ,  $^2\text{H}$ ,  $^{13}\text{C}$  and  $^{31}\text{P}$  NMR measurements were carried out through a Bruker Avance 300 (7.05 T) spectrometer at the operating frequencies of 300.131, 46.072, 75.475 and

121.495 MHz, respectively, at 25 °C. A standard variable temperature control unit (with an accuracy of  $\pm 0.5$  °C) was used.  $^1\text{H}$ -decoupling was applied in all  $^{13}\text{C}$  and  $^{31}\text{P}$  NMR experiments.

**CHAPTER 4-5.** Self-diffusion coefficients were determined using a Bruker DIFF30 probe equipped with a specific insert for the  $^1\text{H}$  and  $^{31}\text{P}$  nuclei, and supplied by a Bruker Great 1/40 amplifier that can generate field gradients up to 1.2 T/m. The pulse-gradient stimulated echo (PGSTE) sequence was used.

Self-diffusion coefficients were calculated by means of a two-parameter nonlinear fit of the echo intensity decay measured at 14 different  $g$  values. In self-diffusion NMR experiments the error on the fitting was always less than 1% (standard deviation). Errors in the NMR measurements are reported in terms of standard deviation.

**CHAPTER 5.** Quantitative evaluation of peak areas and  $^{31}\text{P}$  NMR spin-lattice relaxation times ( $T_1$ ) determinations were performed through a 10 mm wide bore multinuclear probe.  $T_1$  were measured by the standard inversion recovery sequence (180- $\tau$ -90) by acquiring the partially relaxed spectra at 14 different  $\tau$  values. Experiments gave  $T_1 = 2.43 \pm 0.08$  s and  $T_1 = 1.50 \pm 0.09$  s for, respectively, the AMP and the dAMP molecular species in freshly prepared samples.

As to the quantitative analysis, conditions adopted were chosen in order to satisfy the rule which dictates that the sum of the acquisition time ( $at = 1$  s) and the delay between two consecutive pulses ( $D1 = 15$  s) must be greater than five times  $T_1$  ( $at + D1 > 5T_1$ ) to allow a complete relaxation of the magnetization. (Repeated experiments using up to  $D1 = 60$  s did not result in significant variation on the measured peak areas).  $^1\text{H}$ -decoupled  $^{31}\text{P}$  NMR spectra were acquired by exploiting an inverse gated pulse sequence to suppress the nuclear Overhauser effect (nOe) and by using a  $90^\circ$  pulse (12.5  $\mu\text{s}$ ). Usually, 256 scans were performed to achieve an optimal signal-to-noise ratio. The quantitative analysis was carried out through an iterative fitting of the spectra (assuming a Lorentzian shape for the  $^{31}\text{P}$  NMR signals) to get the

peak areas by the use of the program Microcal™ Origin™ (version 5.0) from Microcal Software, Inc. (Northampton, MA).

**CHAPTER 5.** <sup>31</sup>P spin-lattice relaxation times were obtained by means of the standard inversion recovery (180-τ-90-acquisition) sequence by acquiring the partially relaxed spectra at 14 different delay values. The error on the fitting was always less than 1% (standard deviation). Errors in the NMR measurements are reported in terms of standard deviation measured over three different experiments for each sample.

### 3.6 SAXRD Experiments

The small-angle X-ray diffraction (SAXRD) was recorded with a S3-MICRO SWAXS camera system (HECUS X-ray Systems, Graz, Austria). Cu K $\alpha$  radiation of wavelength 1.542 Å was provided by a GeniX X-ray generator, operating at 50 kV and 1 mA. A 1D-PSD-50 M system (HECUS X-ray Systems, Graz, Austria) containing 1024 channels of width 54.0 μm was used for detection of scattered X-rays in the small-angle region. The working  $q$ -range (Å<sup>-1</sup>) was  $0.003 \leq q \leq 0.6$ , where  $q = 4\pi \sin(\theta)\lambda^{-1}$  is the modulus of the scattering wave vector. Silver behenate (CH<sub>3</sub>-(CH<sub>2</sub>)<sub>20</sub>-COOAg) with a  $d$  spacing value of 58.38 Å was used as a standard to calibrate the angular scale of the measured intensity. A few milligrams of LC samples were enclosed in a stainless steel sample holder using a polymeric sheet (Bratfolie, Kalle) windows during normal measurements, while pressure dependent experiments were performed with a stainless steel hydrostatic pressure cell with diamond windows. A PC-controlled Peltier element was used for temperature stabilization and control of the sample. To minimize scattering from air, the camera volume was kept under vacuum during the measurements. The lattice parameters were determined from the linear fits of the measured peak position  $q$  versus Miller indexes, using the relations reported in paragraph 2.3. Scattering patterns were usually recorded for 3600 s.

### **3.7 FT-IR experiments**

FT-IR spectra were recorded with a Bruker Tensor 27 spectrophotometer equipped with a BIO-ATR II module and N<sub>2(l)</sub>-cooled MCT detector. For each measurement 64 scans were collected and Fourier transformed to obtain a nominal spectral resolution of 2 cm<sup>-1</sup> over the frequency range 900-4000 cm<sup>-1</sup>. BIO-ATR chamber was heat controlled at 25 ± 0.1 °C. Samples were placed in the BIO-ATR and a 10 min waiting time was used to allow the temperature equilibrium before recording spectra. Before each measurement, ATR crystal was cleaned with 2-propanol, distilled water, and dried with a soft tissue until baseline recorded ensured that no residue of previous sample was retained. OPUS software (Bruker, Milan, Italy) was used for spectra analysis.

### **3.8 Cryogenic-Transmission Electron Microscopy (Cryo-TEM)**

Vitrified specimens were prepared in a controlled environment vitrification system (CEVS), at 25 °C and 100% relative humidity. A drop of the sample was placed on a perforated carbon film-coated copper grid, blotted with filter paper, and plunged into liquid ethane at its freezing point. The vitrified specimens were transferred to an Oxford CT-3500 cooling holder, and observed at 120 kV acceleration voltage in an FEI T12 transmission electron microscope at about -180 °C in the low-dose imaging mode to minimize electron-beam radiation damage. Images were digitally recorded with a Gatan US1000 high-resolution CCD camera.

### **3.9 Cryo-TEM Images Analysis**

Fast Fourier transform and sizing of the nanoparticles were performed by ImageJ 1.42p (NIH, USA) and Image-Pro Express 6.0 (Media Cybernetics, Inc.) software, respectively. The accuracy of the lattice parameter determined from cryo-TEM images analysis was estimated around ±10%.

### 3.10 Cell Cultures

Mouse Swiss 3T3 fibroblasts (ATCC collection), HeLa (human epithelial cervical carcinoma), and HEK 293T (human embryonic kidney) cell lines were grown in Dulbecco's modified Eagle's medium (DMEM, Gibco, Life Technologies, Grand Island, NY) with high glucose, supplemented with 10% (v/v) fetal bovine serum, penicillin (100 U mL<sup>-1</sup>), and streptomycin (100 µg mL<sup>-1</sup>) (Gibco) at 37 °C in a 5% (v/v) CO<sub>2</sub> incubator.

### 3.11 Image Analysis on 3T3 Cells

3T3 cell lines were seeded in number of 10<sup>5</sup> cells/cm<sup>2</sup> in 35 mm glass-bottomed dishes (MatTek, Ashland, MA). One day after seeding, nanoparticle formulations were added to the cells in serum-free medium (to avoid aggregation with serum) at a concentration of 1:200 (10 µL of LNP formulations in 2 mL of cell growth medium). The incubation time was 1 h. After incubation, the cells were washed twice with PBS (to remove all nanoparticles); then, they were supravivally stained for 15 min with the following probes: 300 nM Nile Red (NR, Fluka, Buchs, SG, Switzerland) and 650 nM Hoechst 33258 (Sigma, St. Louis, MO). The excitation and emission filters for NR were as follows: ex 460 ± 25 nm, em 535 ± 20 nm (band-pass) for nonpolar lipids; ex 540 ± 12.5 nm, em > 590 nm (long pass) for polar lipids. The excitation and emission filters for Hoechst 33258 were the following: ex 360 ± 20 nm, em 460 ± 25 nm. The adopted filters allowed for a virtually complete separation of the emission and simultaneous observation of the two probes in live cells. The vehicles were DMSO for NR and water for Hoechst 33258. Stock solutions were 1000-fold concentrated to not exceed the 0.1% vehicle concentration in the medium. All experiments were replicated three times. Observations were made using an Olympus IX 71 inverted microscope (Olympus, Tokyo, Japan) with 20× (0.7 NA) and 60× (1.3 NA/oil immersion) planapochromatic objectives (UPlanSApo series). Images were taken with a 12-bit cooled CCD camera (Sensicam PCO, Kelheim, Germany), coupled to a



mechanical shutter interposed between the 100 W Hg lamp and the microscope, to limit illumination of cells to the time strictly required for acquisition of images. Excitation light was attenuated with a 6% neutral density filter. Image analysis and measurements were performed with the ImagePro Plus package (Media Cybernetics, Silver Springs, MD). In the case of LCh-stabilized NPs, internalization was proved by adding NR in the LC matrix before the dispersion process.

### 3.12 Alamar Blue Assay on HeLa and HEK 293T Cells

For cell viability experiments,  $0.3 \times 10^5$  cells/well were seeded onto 24-well plates, 24 h prior to incubation with the different formulations. Nanoparticle formulations were added to the cells in serum-free medium at a concentration of 1:200 (10  $\mu$ L of LNP formulations in 2 mL of cell growth medium). Cell viability was assessed by a modified Alamar Blue assay. Viable cells cause the reduction of Alamar Blue dye, resulting in a chemical change from a blue form (resazurin) to a red form (resorufin). A decrease in cell viability is determined by a drop in the capacity of cells to reduce the resazurin present in the medium. Briefly, 4 h after incubation with the different formulations, cells were incubated with DMEM containing 10% (v/v) Alamar Blue dye (resazurin). After 1 h of incubation, the absorbance of the medium was measured at 540 and 630 nm. Cell viability was calculated, as a percentage of the untreated control cells, according to eq. 3.1:

$$\text{cell viability (\% of control)} = \frac{A_{540} - A_{630}}{A'_{540} - A'_{630}} \times 100 \quad \text{eq. 3.1}$$

where  $A_{540}$  and  $A_{630}$  are the absorbances of the samples and  $A'_{540}$  and  $A'_{630}$  those of control cells, at the indicated wavelengths.

### **3.13 Statistical Analysis**

All data are presented as mean  $\pm$  standard deviation (SD). Data were analyzed using GraphPad Prism software. The statistical significance of differences between data (each experiment compared to the corresponding control) was evaluated by a two-tailed unpaired *t* test at a 95% confidence level ( $p \leq 0.05$ ).

## Chapter 4

# Effect of Nucleotides and Nucleolipids on the phase behavior of the MO/W system.

### 4.1 Introduction

The particular properties of MO cubic phases such as temperature stability, bicontinuous structures, high internal surface area, solidlike viscosity, together with their biocompatibility and full biodegradability make them interesting candidates for drug delivery. The most popular application of cubic phase is as a delivery vehicle for hydrophobic/hydrophilic molecules that, after solubilization into the cubic gel, diffuse out in a controlled-release manner. For example, a number of proteins, such as lysozyme<sup>56</sup> and cytochrome c<sup>57</sup> have been incorporated into the MO cubic phases. Moreover the enzyme activity of protein kinase C bound to cubic phase membranes is much greater than that bound to phospholipid in the lamellar phase.<sup>58</sup>

Nucleotides and nucleolipids are sensitive molecules that need to be protected since they can be easily recognized and degraded by different extracellular nucleases, resulting in poor *in vivo* pharmacokinetic properties. In order to assess the possible applications of the MO/W LC phases in the drug delivery the incorporation of AMP, GMP, UMP and CMP (XMPs), along with two hydrophobically functionalized nucleotides (nucleolipids), i.e. the 1-palmitoyl-2-oleoyl-sn-glycerol-3-phosphoadenosine (POPA) and the hexadecyl-phosphoadenosine (HPA), in the lamellar and in the cubic phases of the MO/W system is presented. The characterization of the nanostructures of the LC pre-formulations in the presence of the XMPs, POPA and HPA is the main focus of the investigation.

## 4.2 Results and Discussion

### 4.2.1 Pseudo-binary diagrams

All samples for phase diagram characterization were prepared in  $^2\text{H}_2\text{O}$  (D). Figure 4.1 shows the phase diagrams of the different MO/D/XMP systems (where XMP stands for AMP, GMP, CMP and UMP nucleotide) at 25 °C in comparison with the MO/D system. The phase diagrams were characterized by optical microscopy,  $^2\text{H}$  and  $^{31}\text{P}$  NMR, and SAXRD. Due to the small amount of POPA and HPA available, it was not possible to explore the whole MO/D phase diagram in the presence of these molecules. Thus, only few lamellar and cubic MO/D/POPA and MO/D/HPA samples, containing 1.0 wt% of the nucleolipids, were prepared and characterized.

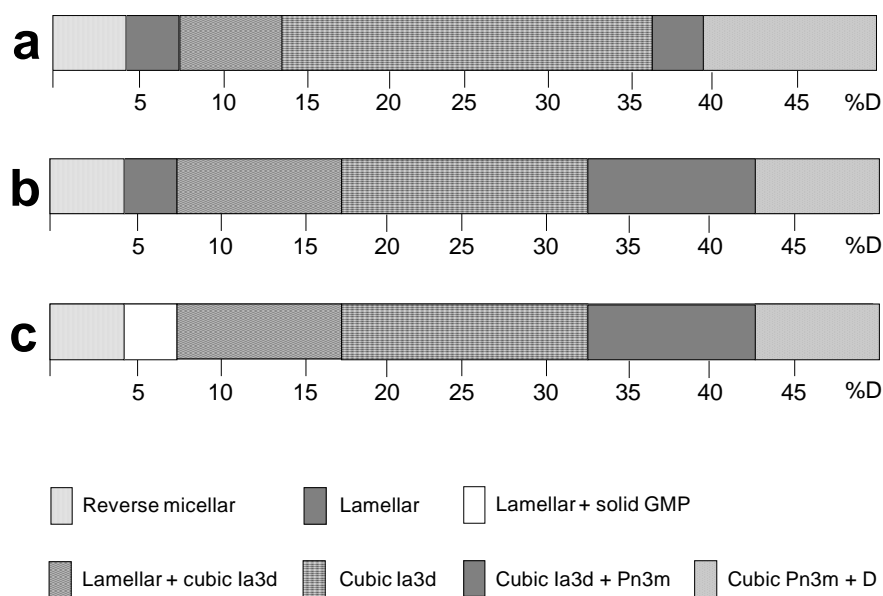


**Figure 4.1** Phase diagrams at 25 °C of (a) MO/D, (b) MO/D/AMP, CMP, UMP and (c) MO/D/GMP systems. Nucleotides content in the pseudo-binary diagrams is 1.5 wt%

The diagrams of the systems containing the XMPs are essentially identical both in terms of phase type and boundary profiles, although some differences in the lamellar region were found. Indeed, as better discussed below, the various lamellar phase

regions here explored (at 25 °C) are characterized by the coexistence of two (MO/D/AMP,CMP,UMP systems) or three (MO/D and MO/D/GMP systems) different lamellar phases, which consist of the crystalline ( $L_c$ ), the gel ( $L_\beta$ ) and the liquid-crystalline ( $L_\alpha$ ) phases.

The same sequence of reverse micellar, lamellar, cubic  $la3d$  and  $Pn3m$  phases which are present in the MO/D system with increasing water content are identified in the presence of 1.5 wt% of XMP. However, phase boundaries, determined with a precision of  $\pm 2$  wt%, are shifted at different water/lipid ratios with respect to the binary system as a consequence of the presence of a hydrophilic additive. Large lamellar-cubic two-phases regions appear in the presence of XMP.

#### 4.2.2 The lamellar phases

The nucleotides and nucleolipids arrangement within the  $L_\alpha$  phase were investigated through SAXRD,  $^2\text{H}$  and  $^{31}\text{P}$  NMR.

As frequently observed in lamellar phases having a low water content, the SAXRD diffractograms (not shown) are characterized by a single, intense peak at low  $q$  values. The bilayer thickness  $2L$  (where  $L$  represents the lipid length), reported in table 4.1, were determined from the lattice parameter  $a$  according to

$$a = \frac{2L}{\Phi_{lip}} \quad \text{eq. 4.1}$$

where  $\Phi_{lip}$  is the lipid volume fraction. The densities used for  $\Phi_{lip}$  calculation were  $0.942 \text{ g/cm}^3$  for MO,<sup>39</sup> and  $1.095 \text{ g/cm}^3$  for D, while for XMPs, POPA and HPA a density of  $1.000 \text{ g/cm}^3$  was assumed.

The  $2L$  values determined from the scattering analysis well agree with those elsewhere reported<sup>59</sup> for the binary MO/water system (small discrepancies, lower than 3%, can be ascribed to the use in this paper of deuterated water) and, on the whole, demonstrate that inclusion of the XMPs, HPA and POPA molecules in such a concentration does not affect significantly the lamellar LC microstructure. More

specifically, both the single-chained and the double-chained negative nucleolipids can be embedded in the MO lamellae, yielding a monophasic system with no appreciable structural variation with respect to the host lipid phase.

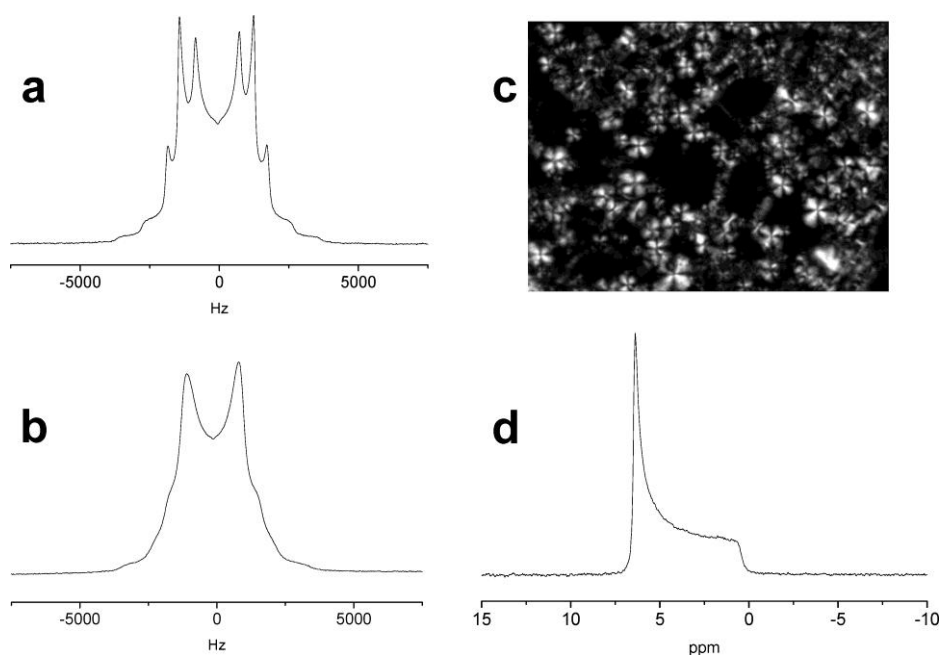


**Figure 4.2** Some NMR spectra along with a micrograph representative of the different MO/D/XMP systems within the lamellar region (5 wt% water content, see also the text): a)  $^2\text{H}$  NMR spectra of MO/D system; b)  $^2\text{H}$  NMR spectra of MO/D/AMP system; c) optical micrograph in polarized light of MO/D/AMP system; d)  $^{31}\text{P}$  NMR spectrum of the MO/D/AMP system.

Figure 4.2 shows the  $^2\text{H}$  NMR spectra of MO/D and MO/D/AMP samples containing 5 wt% of deuterated water, along with the  $^{31}\text{P}$  NMR spectrum of the MO/D/AMP sample and an optical microscopy image representative of all the samples containing the nucleotides at this composition. Concerning the  $^2\text{H}$  NMR spectra, it should be noted that those related to samples where CMP, UMP, POPA and HPA were included display the same feature as the MO/D/AMP sample (figure 4.2b), whereas that

related to the sample containing GMP is not distinguishable from MO/D binary sample (spectrum not shown).

At this low water content in the monoolein/water phase diagram only two different lamellar phases, the coagel or crystalline ( $L_c$ ) and the liquid-crystalline ( $L_\alpha$ ), were reported by Caffrey et al..<sup>60</sup>

However, here the deuterium quadrupolar splittings observed in the NMR spectrum of the MO/D sample confirm the occurrence of three coexisting lamellar spacing originated by the small amount of water (D/MO molar ratio around 1.2) that, in turns, induces an inhomogeneous distribution of the water molecules in the aqueous layers of the different lamellar phases. The third lamellar phase can be ascribed to a gel ( $L_\beta$ ) phase since its occurrence has been occasionally discussed in monoglyceride/water system.<sup>61-63</sup> Its presence is very likely due to the use of both deuterated water and monoolein having a high percentage of 2-monoglyceride (see Materials and Methods).

The broadening in the  $^2\text{H}$  NMR pattern along with the vanishing of the inner splitting induced by the AMP, CMP and UMP addition in the MO/D system is likely to be due to a non homogeneous distribution of the water between the XMP molecules and the MO interface.

On the other hand, the observation that GMP inclusion does not provoke any appreciable change in the  $^2\text{H}$  NMR pattern of the MO/D system may be related to its low solubility at this water content. This hypothesis is also supported by the fact that, in order to achieve a good signal-to-noise (S/N) ratio for the AMP, CMP and UMP  $^{31}\text{P}$  NMR spectra, 1k scans were collected, while the GMP spectrum had to be acquired collecting 20k scans to get a similar S/N.

Regarding the  $^{31}\text{P}$  NMR spectra, all samples containing XMPs show clear CSA with axial symmetry<sup>64</sup> having similar features (see figure 4.2d) although quite different  $\Delta\sigma$ , as reported in table 4.1.

**Table 4.1.** Lipid volume fractions ( $\Phi_{lip}$ ) along with lattice parameters ( $a$ ) and bilayer thickness ( $2L$ ) from SAXRD analysis, and  $^{31}\text{P}$  CSA ( $\Delta\sigma$ ) from NMR analysis, in lamellar MO/D/XMP-POPA-HPA samples with composition 93.5/5.0/1.5 (95/5 for the binary sample).

Sample	AMP	GMP	CMP	UMP	HPA	POPA
$\Phi_{lip}$	0.943	0.943	0.943	0.943	0.957	0.957
$a$ (Å)	36.5	35.7	36.2	35.7	36.2	36.0
$2L$ (Å)	34.4	33.6	34.1	33.6	34.6	34.5
$\Delta\sigma$ (ppm)	$5.3 \pm 0.1$	$6.8 \pm 0.2$	$8.6 \pm 0.1$	$4.9 \pm 0.1$	$-27 \pm 0.5$	$-27 \pm 0.5$

Surprisingly, the displayed CSA orientation appear reversed compared to that typically observed for lamellar assemblies.<sup>50</sup> To shed some light on this unexpected behavior a MO/D/AMP sample with a tiny amount (0.8 wt%) of distearoylphosphatidylcholine (DSPC), also added as a molecular probe, was prepared. The recorded  $^{31}\text{P}$  NMR spectrum, reported in figure 4.3, reveals the two superimposed CSA patterns related to the DSPC and the AMP molecular species, the former showing a downfield shoulder and a  $\Delta\sigma$  value ( $-27 \pm 0.5$  ppm) which is approximately half of that classically detected in fully hydrated  $L_{\alpha}$  phases (around -50 ppm). Remarkably, the  $^{31}\text{P}$  NMR spectra obtained when POPA and HPA are included in the lipid phase at this composition (cfr. Figure 4.3) are very similar, and can hardly be distinguished from the spectrum of the sample containing DSPC. Since the  $\Delta\sigma$  value strongly depends on the wobbling motion of the symmetric tensor component, namely  $\sigma_{11}$ , and particularly it reduces as far as it is moved away from the director, it can be inferred that the small  $\Delta\sigma$  observed is caused by a torsion of  $\sigma_{11}$  towards the bilayer plane.<sup>65</sup> This model, which holds for the DSPC as well as for the POPA and the HPA, can be envisaged simply thinking that the very small thickness (1-2 Å) of the water layer does not allow the full extension of the phosphocholine moiety out from the glycerol backbone.



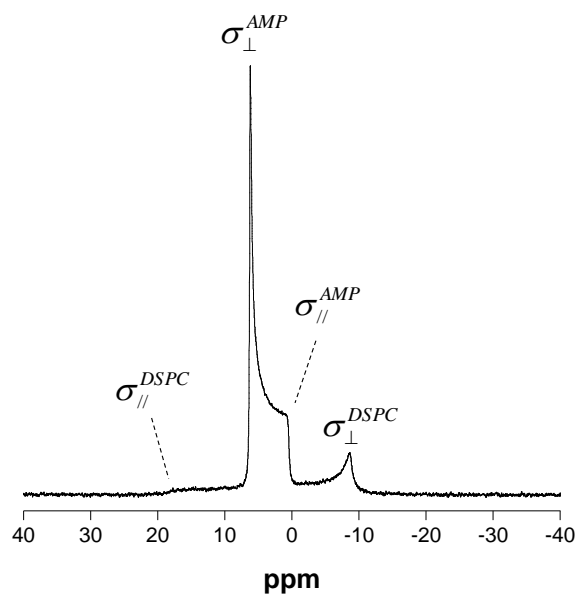


**Figure 4.3.**  $^{31}\text{P}$  NMR spectrum of a MO/D/AMP sample having the same composition as in figure 2d where 0.8 wt % of DSPC was also added.

Similarly, the reason for the “anomalous”  $^{31}\text{P}$  CSA patterns has to be found in the XMPs orientation with respect to the director. Indeed, again bringing into play the thin water layer in the lamellar phases under study, the XMP molecules ought to lay down the bilayer plane and their  $\sigma_{11}$  components are evidently oriented perpendicularly with respect to the director. This is the opposite condition to that pertaining to classically observed phosphate bearing molecules, like phospholipids, arranged in lamellar phases, and therefore embedded in the bilayer palisade with their symmetric axis oriented parallel to the director. The small  $\Delta\sigma$  detected for the nucleotides can be justified observing that XMPs molecular motion within the water layer is much less hindered than that of DSPC, POPA and HPA and therefore the CSA can be partially averaged out.

These features will be further considered below.

### 4.2.3 The cubic phases

The cubic phase regions were investigated through SAXRD and NMR. Four different water contents were examined for each ternary system. Table 4.2 summarizes the compositions and the results obtained from SAXRD data analysis.

Samples in the range 15-30 wt% of water belong to the  $Ia3d$  ( $C_G$ ) space group, whereas samples containing around 40 wt% of water show the typical pattern of the  $Pn3m$  ( $C_D$ ) space group. Examples of SAXRD patterns for MO/D/AMP samples are reported in figure 4.4. In particular, figures 4.4 a, b, and c show respectively the  $C_G$  pattern observed for a D content of 29.6 wt%, the  $C_G+C_D$  overlapped patterns of the two-phase sample with a D content of 37.4 wt% and the  $C_D$  pattern for a D content of 39.4 wt%.

Table 4.2. SAXRD data of samples in the cubic region: sample composition (X here stands for XMP, POPA and HPA), lipid volume fraction ( $\Phi_{lip}$ ), lattice parameter ( $a$ , errors are reported in terms of standard deviation based on the observed peak's position) and radius of the water channels ( $r_w$ ), calculated using equations 4.2 and 4.3.

	MO/D/X	$\Phi_{lip}$	Space group	$a$ (Å)	$r_w$ (Å)
AMP	80.9/17.6/1.5	0.841	<i>Ia3d</i>	107.9 ± 0.2	9.8
	76.8/21.7/1.5	0.804	<i>Ia3d</i>	111.3 ± 0.3	10.6
	74.7/23.8/1.5	0.774	<i>Ia3d</i>	119.3 ± 0.1	12.6
	72.8/25.7/1.5	0.756	<i>Ia3d</i>	125.7 ± 0.2	14.2
	70.8/27.7/1.5	0.737	<i>Ia3d</i>	129.1 ± 0.1	15.0
	68.9/29.6/1.5	0.730	<i>Ia3d</i>	131.6 ± 0.2	15.6
	59.9/39.4/1.5	0.611	<i>Pn3m</i>	95.1 ± 0.3	20.2
GMP	76.8/21.7/1.5	0.804	<i>Ia3d</i>	113.3 ± 0.3	11.1
	75.0/23.5/1.5	0.776	<i>Ia3d</i>	119.3 ± 0.1	12.6
	72.9/26.5/1.5	0.767	<i>Ia3d</i>	122.9 ± 0.3	13.5
	70.7/27.8/1.5	0.736	<i>Ia3d</i>	125.7 ± 0.2	14.2
	68.9/29.6/1.5	0.730	<i>Ia3d</i>	125.2 ± 0.2	14.0
	59.9/39.4/1.5	0.630	<i>Pn3m</i>	94.3 ± 0.3	19.9
CMP	80.8/17.7/1.5	0.841	<i>Ia3d</i>	107.7 ± 0.3	9.7
	76.8/21.7/1.5	0.805	<i>Ia3d</i>	112.6 ± 0.2	10.9
	75.2/23.3/1.5	0.778	<i>Ia3d</i>	117.1 ± 0.3	12.0
	72.2/26.2/1.5	0.750	<i>Ia3d</i>	124.0 ± 0.2	13.7
	70.8/27.6/1.5	0.736	<i>Ia3d</i>	129.1 ± 0.1	15.0
	69.4/29.1/1.5	0.735	<i>Ia3d</i>	137.4 ± 0.6	17.1
	51.9/46.6/1.5	0.623	<i>Pn3m</i>	95.1 ± 0.1	20.2
UMP	80.8/17.7/1.5	0.841	<i>Ia3d</i>	105.8 ± 0.3	9.2
	76.8/21.7/1.5	0.804	<i>Ia3d</i>	113.0 ± 0.2	11.0
	74.6/23.9/1.5	0.772	<i>Ia3d</i>	120.8 ± 0.2	12.9
	72.8/25.7/1.5	0.756	<i>Ia3d</i>	124.7 ± 0.1	13.9
	70.7/27.8/1.5	0.736	<i>Ia3d</i>	126.6 ± 0.2	14.4
	68.5/29.6/1.5	0.734	<i>Ia3d</i>	118.8 ± 0.6	12.5
	59.9/39.4/1.5	0.621	<i>Pn3m</i>	96.0 ± 0.3	21.5
HPA	69.3/29.7/1.0	0.723	<i>Ia3d</i>	137.9 ± 0.3	17.2
POPA	69.3/29.7/1.0	0.723	<i>Ia3d</i>	134.0 ± 0.2	16.2

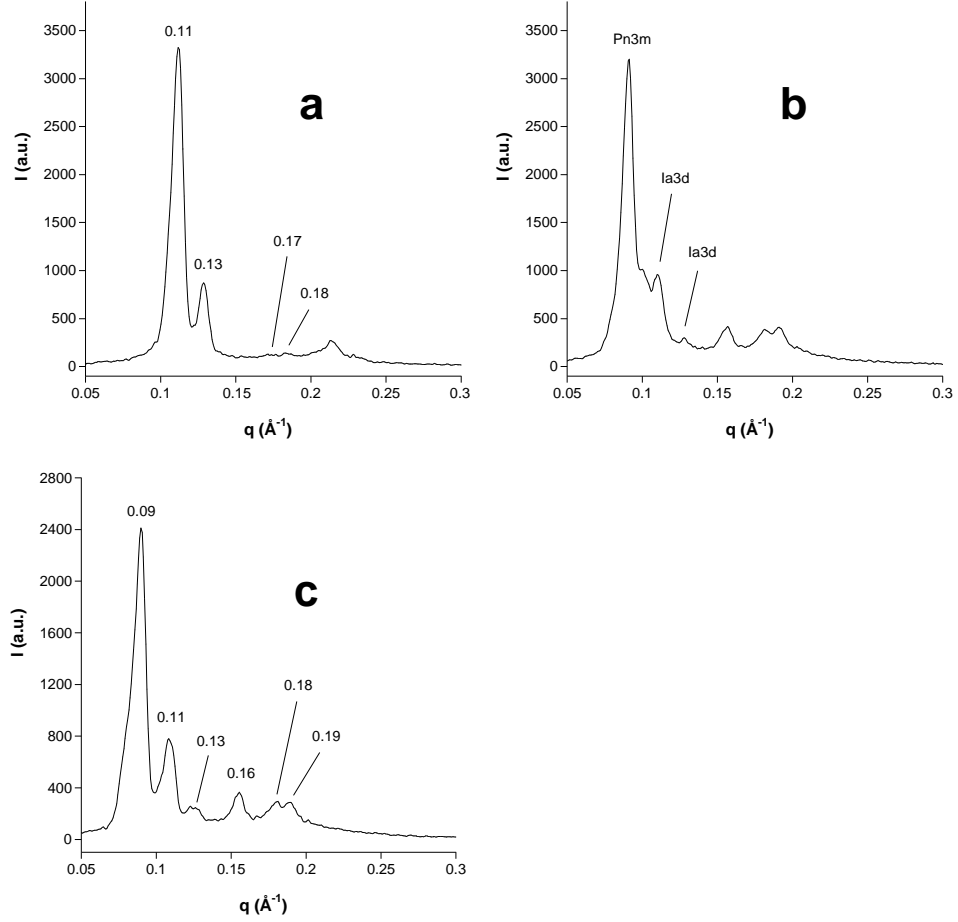


**Figure 4.4** SAXRD patterns at 25 °C of MO/D/AMP samples, containing 1.5 wt% of AMP, at different water content: a) 29.6 wt%; b) 37.4 wt%; c) 39.4 wt%.

For cubic phases, the lipid length value ( $L$ ) should verify the swelling law according to eq 2:<sup>59</sup>

$$\Phi_{lip} = 2A_0 \left( \frac{L}{a_{cub}} \right) + \frac{4\pi\chi}{3} \left( \frac{L}{a_{cub}} \right)^3 \quad \text{eq. 4.2}$$

where  $a$  is the lattice parameter obtained from the SAXRD analysis, while  $A_0$  and  $\chi$  are the surface area and the Euler characteristic of the IPMS geometries (*la3d*:  $A_0 = 3.091$ ,  $\chi = -8$ ; *Pn3m*:  $A_0 = 1.919$ ,  $\chi = -2$ ).

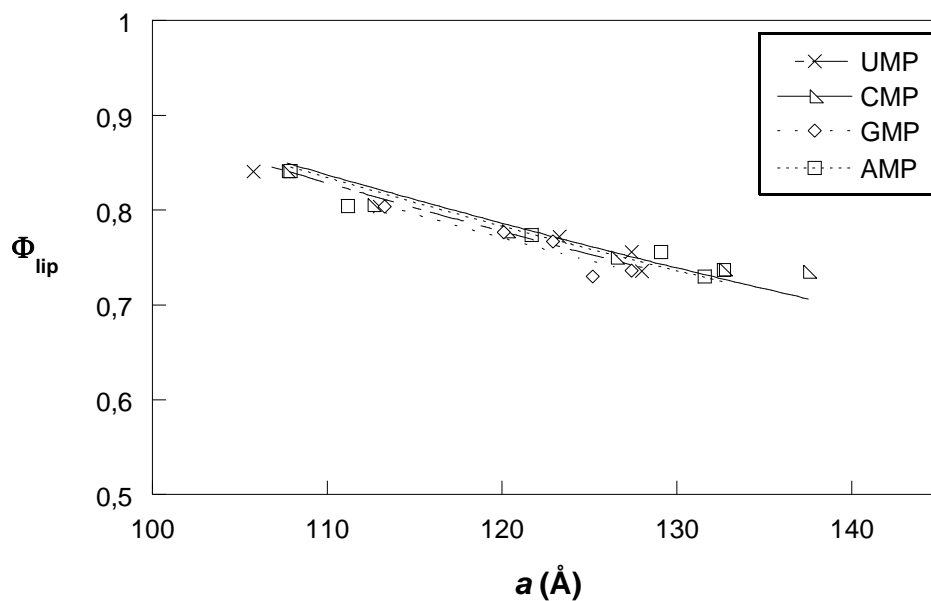


Figure 4.5 Lipid volume fraction ( $\Phi_{lip}$ ) vs. XMPs lattice parameter ( $a$ ) for  $1a3d$  cubic samples.

Figure 4.5 shows the lipid volume fraction reported as a function of the XMPs lattice parameters. The lines represent the fit of data to eq 4.2 from which the  $L$  value is calculated.

The fittings are fairly satisfying and the obtained lipid length values, 17 Å with errors smaller than 2%, are in excellent agreement with values usually reported for the MO.<sup>6</sup>

Table 4.2 also reports the water channels radii,  $r_w$ , calculated according to eq 4.6:<sup>6,59,66</sup>

$$r_w = \left( \frac{A_o}{-2\pi\chi} \right)^{1/2} a - L \quad \text{eq. 4.3}$$

### 4.3 Conclusions

The potentiality of the MO/D system as a matrix for the solubilization of nucleotides and nucleolipids has been investigated at 25 °C. The study of the phase behavior of the various pseudo-binary systems shows that both kind of additives can be entrapped inside the various LC phases without significant alterations of the lipid nanostructure. Moreover, it was shown that the MO/D cubic samples where POPA and HPA were dissolved are highly stable and no symptoms of degradation were observed even after 2 years. Therefore the MO/D cubic phases represent an excellent nanodevice for the compartmentalization of hydrophobically derivatized nucleotides.

These findings represent a promising result, in view of the formulation of novel lipid-based carriers for amphiphilic nucleotide analogues. The combination of the high biocompatibility and bioadhesivity of MO bicontinuous cubic phase dispersions, together with the excellent stability of the drug-loaded mesophases, can open new perspectives, in terms of increased payload, bioavailability, and sustained release.

## Chapter 5

# Temperature- and pressure- dependent phase behavior of MO/W/XMP cubic phases

### 5.1 Introduction

The monoolein-water binary system was investigated for the effects of changes of temperature,<sup>59,67</sup> and more recently for phase stability and the phase transitions related to pressure changes.<sup>68</sup> Structural transitions induced by pressure and temperature usually display opposite trends: pressure increases the order of the acyl chain which results in a decrease of molecular wedge shape, a decrease of interfacial curvature, an increase of bilayer thickness thus promoting an increase of the cubic lattice constant, whereas temperature increases the molecular wedge shape, thus favoring reverse curvatures.

Pressure jumps were used to investigate the cubic-to-cubic phase transition and kinetics of phase transitions.<sup>69</sup> Pressure was also used to study the interaction of cytochrome *c*<sup>70</sup> and  $\alpha$ -chymotrypsin<sup>71</sup> with MO/W cubic phase. Currently, pressure has become a thermodynamic variable of growing interest because it represents an additional tool for understanding phase behavior, stability and energetics of amphiphilic molecules. Moreover pressure only change intermolecular distances and affect conformations but do not change covalent bond distances or bond angles. Therefore covalent structure of lipids and small molecules is not perturbed.

The present study is directed towards a better understanding of the effect of nucleotide inclusion on the stability of cubic mesophases. To obtain an extended description of stability and phase behavior of cubic liquid crystalline phases, thermotropic and barotropic effects have here been investigated. The *la3d* cubic

phases with 30 wt % of water and the  $Pn3m$  cubic phases with 40 wt % of water, both containing 1.5 wt % of nucleotides, were selected for this study. The structural aspects of the cubic phases were investigated by using the SAXRD and NMR techniques within a wide range of temperatures (25-85 °C) and pressures (1–1000 bar).

## 5.2 Analysis of structural parameters

Assuming distinct lipid and water regions within the unit cell, the internal structural dimensions of the lipid-containing phases can be calculated from the measured unit cell dimensions and the sample concentration. Bicontinuous cubic phases can be described as lipid bilayers lying on Infinite Periodical Minimal Surfaces (IPMS). In this model, the surface where the terminal methyl groups of acyl chains from adjacent lipid monolayers meet defines the IPMS. Since dealing with inverted mesophases, the cross-sectional area per lipid molecule is a maximum at the minimal surface and decreases progressively along the length of the hydrocarbon chain to reach a minimum value at the glycerol headgroup. The projected cross-sectional area reduces to zero at the center of the water channel.

For a cubic phase of the type under discussion,<sup>72</sup> have shown that the molecular cross-sectional area evaluated on a surface parallel to and at a distance  $\xi$  from the minimal surface and integrated over one of the two monolayers within the unit cell,  $A(\xi)$ , is related to the experimentally measurable lattice parameter  $a$  as follows:

$$A(\xi) = \sigma a^2 + 2\pi\chi\xi^2 \quad \text{eq. 5.1}$$

where  $\sigma$  is a unitless quantity that describes the ratio of the minimal surface in a unit cell to the quantity (unit cell volume)<sup>2/3</sup>, and  $\chi$  is the Euler–Poincarè characteristic of the IPMS geometry ( $Ia3d$ ,  $\sigma = 3.091$ ,  $\chi = -8$ ;  $Pn3m$ ,  $\sigma = 1.919$ ,  $\chi = -2$ ). Accordingly, the area of the minimal surface in the unit cell is given by  $\sigma a^2$  and defined as  $A_0$ .

According to Turner and co-workers,<sup>73</sup> in the IPMS model the monolayer thickness  $l$  for a given cubic phase, considered constant throughout the structure, can be



calculated using the lattice parameter  $a$ , determined by SAXRD, the known sample composition (volume fraction of the lipid  $\phi_{lip}$ ), and by using the following relation:

$$\phi_{lip} = 2\sigma \left( \frac{l}{a} \right) + \frac{4\pi\chi}{3} \left( \frac{l}{a} \right)^3 \quad \text{eq. 5.2}$$

The unit cell surface area at the headgroup  $A$ , that is, at the lipid-water interface, which is assumed to be parallel to the minimal surface, can be obtained using:

$$A = A_0 \left( 1 + \langle K \rangle_0 l^2 \right) \quad \text{eq. 5.3}$$

Where  $\langle K \rangle_0$  is the surface averaged Gaussian curvature on the minimal surface.  $\langle K \rangle_0$  is related to the lattice parameter through the Gauss-Bonnet theorem:

$$\langle K \rangle_0 = \frac{2\pi\chi}{A_0} \quad \text{eq. 5.4}$$

Other parameters, that are also necessary to describe a complete curvature free energy for the lipid layer are the Gaussian  $\langle K \rangle$  and the Mean  $\langle H \rangle$  curvatures at the lipid-water interface, both averaged over the unit cell. Their values can be calculated using:

$$\langle K \rangle = \frac{2\pi\chi}{A} \quad \text{eq. 5.5}$$

$$\langle H \rangle = \frac{2\pi\chi}{A} l \quad \text{eq. 5.6}$$

The lipid length in the fluid lamellar  $L_\alpha$  phase is given by:

$$l = \frac{a_{lam} \phi_{lip}}{2} \quad \text{eq. 5.7}$$

where  $a_{lam}$  is the lamellar lattice parameter.

### 5.3 Results and discussion

The barotropic and thermotropic phase behavior of MO/D cubic phases (*Ia3d* and *Pn3m*) upon incorporation of 1.5 wt % of nucleotides (AMP, GMP, CMP and UMP) were investigated through SAXRD and NMR techniques. Results obtained for nucleotide-containing samples were compared with the pure lipid system. The SAXRD pressure-dependent studies were carried out at 25 °C from 1 to 1000 bar at 200 bar intervals, whereas temperature-dependent studies were performed at 1 bar from 25 to 85 °C.  $^{31}\text{P}$  and  $^2\text{H}$  NMR spectra were acquired at 1 bar from 25 to 80 °C.

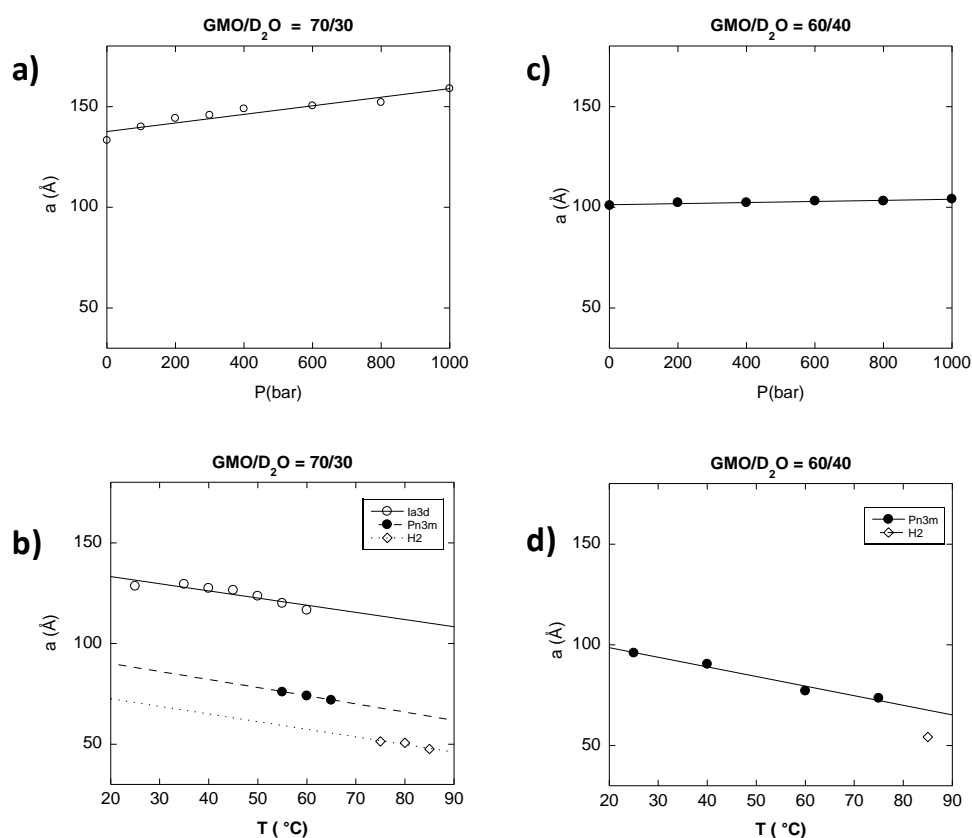


Figure 5.1 Lattice parameter pressure and temperature dependence of the cubic phases of the systems MO/D = 70/30 ( a, b) and MO/D = 60/40 (c, d). Lines are guides to the eyes to show the general trends.

### 5.3.1 *1a3d* cubic phase

Temperature and pressure scans were performed on the sample MO/D = 70/30. The sample was used as reference and compared to those containing nucleotides. Results are shown in figure 5.1 a-b. With increasing pressure the sample undergoes an increase of unit cell dimension from 133.2 Å (1 bar) to 157.2 Å (1000 bar). No phase transitions are observed. At 1 bar the effect of temperature is to induce the formation of a *Pn3m* phase at about 50 °C. At about 85 °C the system evolves towards a reverse hexagonal structure.

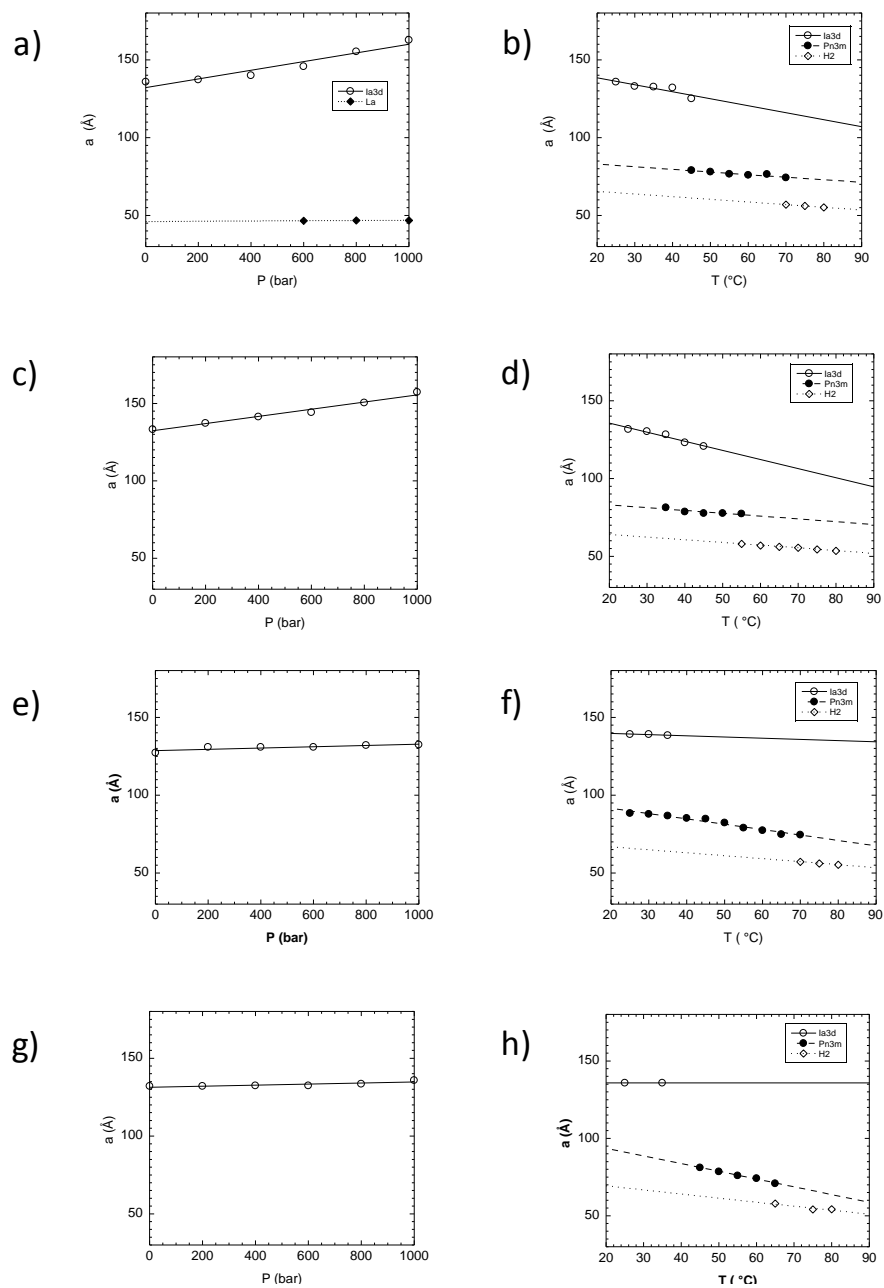


Figure 5.2 Lattice parameter pressure (left) and temperature (right) dependence of the lamellar, cubic and hexagonal phases of the systems MO/D/XMP = 68.9/29.6/1.5 (a, b) AMP, (c, d) GMP, (e, f) CMP and (g, h) UMP. Lines are guides to the eyes to show the general trends.

The lattice parameter pressure and temperature dependence in the *la3d* systems MO/D/XMP = 68.9/29.6/1.5 is shown in figure 5.2.

In the sample containing AMP (fig. 5.2a) pressure induces an increase of the unit cell dimension from 135.8 Å (1 bar) to 162.7 Å (1000 bar). Moreover, in the pressure range of 600-1000 bar the cubic phase coexists with a lamellar phase. Here, it is worth recalling that the wide-angle profiles can be useful in obtaining information on the packing arrangement of the acyl chains in a lamellar phase. For instance, a sharp peak is representative for hexagonally packed hydrocarbons chains in a lamellar gel ( $L_\beta$ ) phase, while a broad peak is the clear signature of the liquid-like hydrocarbons chains arrangement in the lamellar fluid  $L_\alpha$  phase.<sup>74</sup> It should be also noted that, differently from lamellar phases based on lipids particularly suited for WAXS analysis like phospholipids, broadening can make this peak hardly detectable. Since no peaks were recorded in the wide-angle region, the lamellar phase was definitely identified as  $L_\alpha$ . Its lattice parameter increases from 46.5 Å (600 bar) to 46.8 Å (1000 bar).

Differently from the sample containing AMP, where a cubic to lamellar transition is observed, the inclusion of GMP (fig. 5.2c), CMP (fig. 5.2e) and UMP (fig. 5.2g) preserves the *la3d* cubic structure in the range of pressure under study. No lamellar phase is formed. Different trends for the variation of the lattice parameter as a function of pressure are observed. With GMP the lattice increases from 133.2 Å (1 bar) to 157.2 Å (1000 bar), whereas in presence of CMP from 127.2 Å (1 bar) to 132.4 Å (1000 bar) and with UMP from 132.0 Å (1 bar) to 135.8 Å (1000 bar).

Temperature-dependent SAXRD experiments show a reduction of the lattice parameter value with increasing temperature. From 25 °C to 45 °C the *la3d* sample containing AMP (fig. 5.2b) decreases its size from 135.8 Å to 125.1 Å, where a  $Pn3m$  cubic phase starts to form. A small biphasic region of *la3d* and  $Pn3m$  is present in the temperature range of 45-50 °C, after which a pure  $Pn3m$  phase is formed. The lattice parameter decreases from 79.0 Å (45 °C) to 74.2 Å (70 °C). Above 70 °C the  $Pn3m$

cubic phase transforms into a reverse hexagonal phase having a lattice parameter of 56.9 Å.

The transition to  $Pn3m$  cubic phase takes place at different temperatures depending on the nucleotide included: 40 °C with AMP and UMP (fig. 5.2h), 30 °C with GMP (fig. 5.2d) and 25 °C with CMP (fig. 2f). After the transition to  $Pn3m$ , the evolution to the  $H_{II}$  phase takes place at about 65 °C in samples containing AMP, CMP and UMP, whereas in the sample containing GMP the formation of the hexagonal phase is already seen at 55 °C.

### 5.3.2 $Pn3m$ cubic phase

Results obtained from temperature and pressure scans on samples containing nucleotides and prepared in the  $Pn3m$  region of the phase diagram were compared with the sample MO/D = 60/40. Results are shown in figure 5.1c-d. With increasing pressure the sample undergoes an increase of unit cell size from 100.9 Å (1 bar) to 104.1 Å (1000 bar). No phase transitions are observed. Temperature induces a phase transition towards a reverse hexagonal phase at about 85 °C.

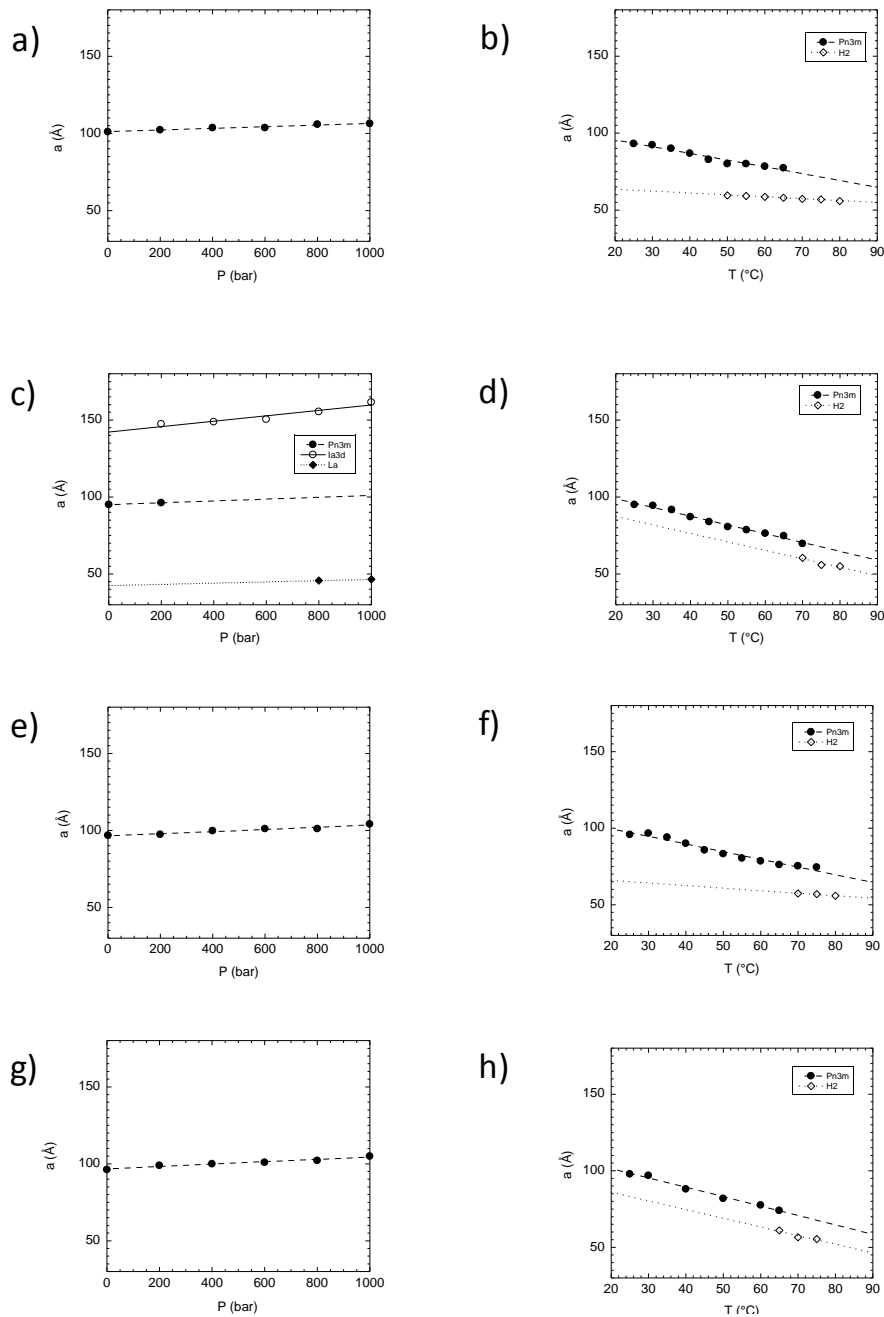


Figure 5.3 Lattice parameter pressure (left) and temperature (right) dependence of the lamellar, cubic and hexagonal phases of the systems MO/D/XMP = 59.1/39.4/1.5 (a, b) AMP, (c, d) GMP, (e, f) CMP and (g, h) UMP. Lines are guides to the eyes to show the general trends.

Figure 5.3 shows the pressure and temperature dependence of the lattice parameter of the  $Pn3m$  systems  $MO/D/XMP = 59.1/39.4/1.5$ .

In the pressure range under investigation the  $Pn3m$  lattice parameter of the sample containing AMP increase from 101.0 Å (1 bar) to 106.3 Å (1000 bar). Differently, the  $Pn3m$  sample containing GMP undergoes a transition from the  $Pn3m$  phase to the  $Ia3d$  (200 bar) and then to the  $L_\alpha$  phase (800 bar). As in case of AMP, samples containing CMP and UMP preserve their structure in the range of 1-1000 bar. With CMP the lattice increases from 96.8 Å (1 bar) to 104.1 Å (1000 bar) and with UMP from 96.2 Å (1 bar) to 104.9 Å (1000 bar).

With increasing temperature, as shown in fig. 5.3b, in the sample containing AMP at about 45 °C a reverse hexagonal phase is formed.  $Pn3m$  and  $H_{II}$  phases coexist up till 65 °C. Above 65 °C the system becomes completely hexagonal. Except for the sample containing AMP, the  $Pn3m$ -to- $H_{II}$  phase transition take place at about 65 °C.

The cubic phases evolution toward hexagonal phase induced by temperature is clearly shown also by the appearance of  $^{31}\text{P}$  CSA and  $^2\text{H}$  quadrupolar splitting in  $^{31}\text{P}$  and  $^2\text{H}$  NMR spectra (figure 5.4).<sup>75</sup>

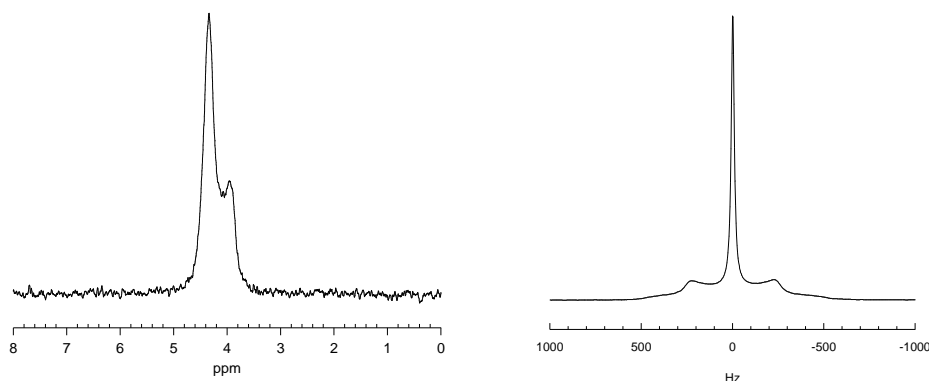


Figure 5.4  $^{31}\text{P}$  and  $^2\text{H}$  NMR spectra of a  $MO/D/AMP = 59.1/39.4/1.5$  sample at 65 °C.



Structural parameters, that are lipid length, Gaussian and Mean curvature, were calculated as a function of pressure and temperature for the various samples under investigation.

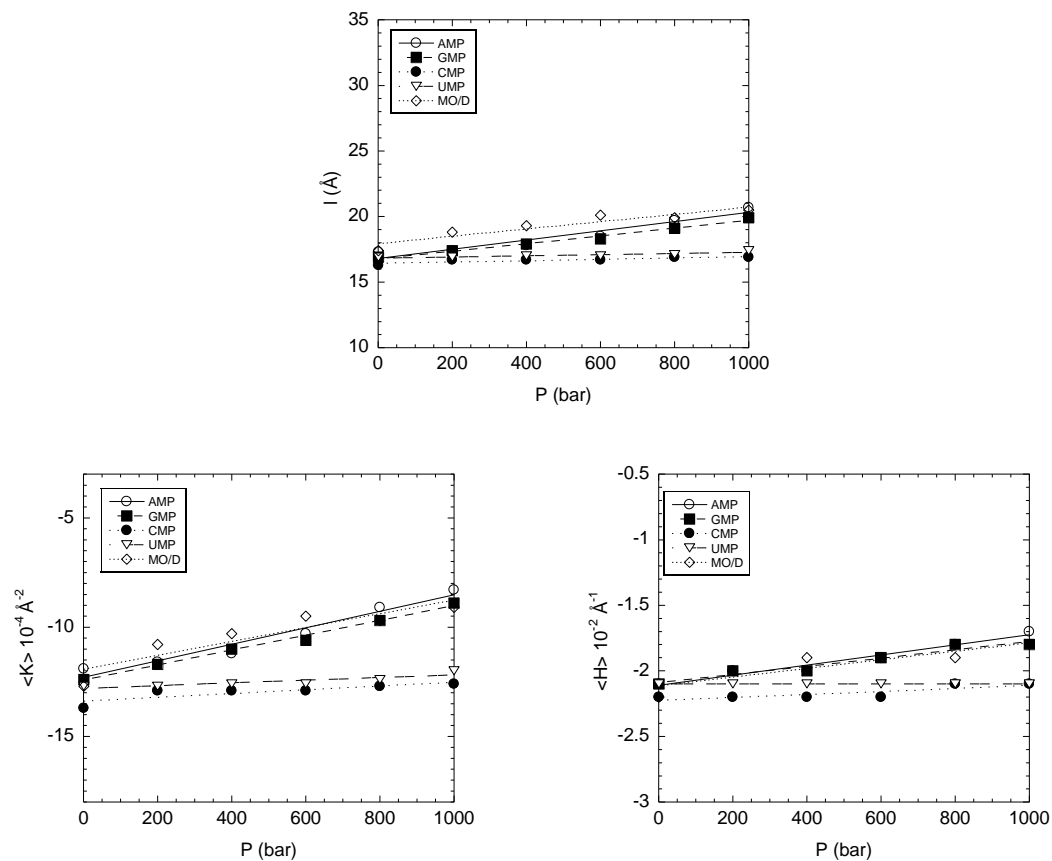
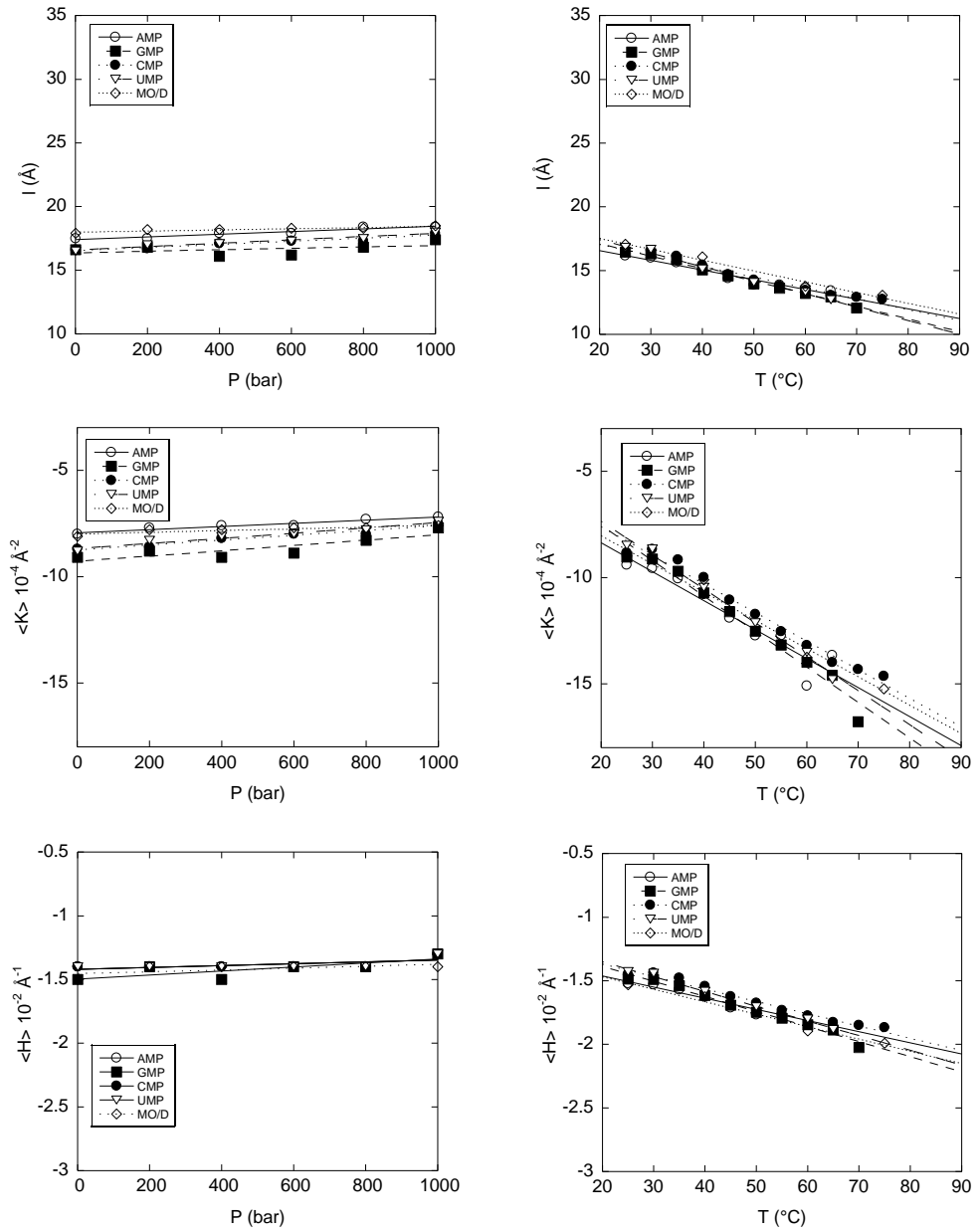


Figure 5.5 Pressure dependence of the structural parameters of the *la3d* cubic phase having composition MO/D/XMP = 68.6/29.9/1.5.  $l$  is the thickness of the monolayer,  $\langle K \rangle$  and  $\langle H \rangle$  are, respectively, the average over the unit cell of the Gaussian and of the mean curvature, calculated at the water-lipid interface. Lines are guides to the eyes to show the general trends.



**Figure 5.6** Pressure and temperature dependence of the structural parameters of the  $Pn3m$  cubic phase having composition MO/D/XMP = 59.1/39.4/1.5.  $I$  is the thickness of the monolayer,  $\langle K \rangle$  and  $\langle H \rangle$  are, respectively, the average over the unit cell of the Gaussian and of the mean curvature, calculated at the water-lipid interface. Lines are guides to the eyes to show the general trends.

Figures 5.5 and 5.6 show the effect of pressure on hydrocarbon chains, Gaussian and mean curvature calculated by equations (5.2), (5.5) and (5.6) respectively on samples prepared in the *la3d* and *Pn3m* regions of the phase diagram. Experimental results are in good agreement with previous results.<sup>68</sup> In both kind of cubic phases, the bilayer thickness, Gaussian and mean curvature increase when pressure increases. The opposite trend is observed when temperature increase.

Nevertheless the presence purine nucleotides (AMP and GMP) and pyrimidine nucleotides (CMP and UMP) seems to influence phase behavior of *la3d* cubic samples differently (figure 5.5). The same dependence is not present in the *Pn3m* samples and no considerable differences are visible (see fig. 5.6) among the various samples in both pressure- and temperature-dependent SAXRD measurements.

The effect of pressure and temperature on lipid structures can be explained with simple molecular packing arguments.<sup>76</sup> The surfactant packing parameter  $v/al$  ( $v$  is the hydrophobic chain volume,  $a$  is the head group area and  $l$  is the chain length, taken as 80% of the fully extended chain) is useful to predict which phase can be preferentially formed by a given surfactant since it connect the molecular properties with the favored curvatures of the aggregate interface. Moreover pressure and temperature variations, changes in composition or the introduction of a new component can strongly affect the molecular wedge shape of the surfactant and then the packing parameter value. An increased wedge shape of the lipid molecules is a result of increasing temperature, whereas pressure exert the opposite effect.

In the cubic phase the reduction in chain wedge shape induced by pressure tends to reduce the magnitude of the (negative) interfacial curvature, thereby swelling the phase if it is in contact with an excess water phase.<sup>77,78</sup> Effects due to pressure increase depend on the nature of the additive and on the type of cubic phase involved: in the *la3d* cubic phase, where the interface curvature is higher, pressure more strongly affects the lattice parameter in comparison to the *Pn3m*, where the curvature is smaller.

The nucleotide tendency to adhere to the lipid interface<sup>75</sup> induces an increase of the surfactant effective packing parameter favoring then the formation of inverted curvatures. This effect is clearly seen during temperatures jumps, where the transition to reverse hexagonal phase is shifted 20 °C toward lower temperatures.

#### **5.4 Conclusions**

SAXRD and NMR spectroscopy were used to study the interaction of nucleotides with the lipid system monoolein/water. The influence of nucleotides incorporation on the thermotropic and barotropic phase behavior of monoolein (MO) cubic phases was investigated. The pressure and temperature dependent studies were conducted on monoolein/D/nucleotide systems at constant D content (30 wt % and 40 wt %) and at fixed nucleotide concentration (1.5 wt %).

Incorporation of nucleotides into the bicontinuous cubic *Ia3d* and *Pn3m* phases doesn't affect the structure and lattice constants significantly but has pronounced effects on the temperature and pressure stability of the systems, changing the phase transition temperatures and pressures. As a general effect, nucleotides tend to increase the monoolein effective packing parameter, favoring inverse curvatures with increasing temperature.

## Chapter 6

# Hydrolysis of nucleotides at the *Ia3d* cubic interface. Part 1

### 6.1 Introduction

The combination of the high biocompatibility and bioadhesivity of MO bicontinuous cubic phases, together with their excellent stability and the capacity to encapsulate both hydrophilic and hydrophobic molecules can open new perspectives, in terms of increased payload, bioavailability, and sustained release. Taking into account the promising applications of these mesophases, it is important to investigate the long-term stability of the lipid matrixes after incapsulation of guest molecules.

Here the long-term stability of MO/D/XMP (HPA and POPA) systems was evaluated. Samples were investigated by means of  $^{31}\text{P}$  and  $^2\text{H}$  NMR, optical microscopy under polarized light and SAXRD, in order to monitor phase transitions and modifications at the molecular level.

The monoolein-water cubic samples where POPA and HPA were dissolved are highly stable and no symptoms of degradation were observed even after 2 years. Therefore the monoolein-water cubic samples represent an excellent nanodevice for the compartmentalization of hydrophobically derivatized nucleotides. These findings represent a promising result, in view of the formulation of novel lipid-based carriers for amphiphilic nucleotide analogues.

Differently, the cubic samples containing the XMP molecules remain stable up to 4 months, if only the visual aspect is considered. In fact, 3-4 weeks after preparation a second isotropic signal in the  $^{31}\text{P}$  NMR spectra starts to grow.

## 6.2 Results and discussion

In chapter 4 it was shown that the MO/D cubic samples where POPA and HPA were dissolved are highly stable and no symptoms of degradation were observed even after 2 years.

Here the potential alterations of the LC matrix induced by nucleotides inclusion is evaluated. It was found that the cubic samples containing the XMP molecules remain stable up to 4 months, if only the visual aspect is considered. In fact, 3-4 weeks after preparation a second isotropic signal in the  $^{31}\text{P}$  NMR spectra starts to grow. The new signal is located around 1 ppm upfield with respect to the XMP NMR signal, and its intensity gradually increases with sample aging.

In order to assign the new signal, some  $^{31}\text{P}$  NMR self-diffusion measurements were performed. For MO/D/XMP samples containing about 30 wt% of water a self-diffusion coefficient ( $D$ ) in the range  $0.28 - 0.33 \times 10^{-10} \text{ m}^2 \text{ s}^{-1}$  for the different XMP species, and a  $D$  value in the range  $0.8 - 1.0 \times 10^{-10} \text{ m}^2 \text{ s}^{-1}$  for the upfield signal were measured. The assignment of the latter to a new phosphate species was achieved by measuring the  $^{31}\text{P}$  NMR self-diffusion coefficient in a MO/D/ $\text{Na}_2\text{HPO}_4$  sample with composition 70/29.2/0.8 (wt%), for which the  $\text{Na}_2\text{HPO}_4$  salt has the same molarity in water ( $\sim 0.2 \text{ M}$ ) as the XMP in the MO/D/XMP samples. Indeed a  $D$  value of  $(0.87 \pm 0.05) \times 10^{-10} \text{ m}^2 \text{ s}^{-1}$  was measured for the  $\text{HPO}_4^{2-}$  phosphate species entrapped in the MO/D cubic LC phase. This finding strongly suggests the occurrence of significant hydrolysis of XMP inside the water channels of the bicontinuous cubic phase. The possibility that hydrolysis occurs at the ribose-base bond level was definitely ruled out observing that the  $^{31}\text{P}$  NMR signals of AMP and ribose phosphate within the cubic phase display almost the same chemical shift while the  $\text{HPO}_4^{2-}$  signal resonates approximately 0.8 ppm upfield.

The hydrolysis progresses with time slowly. As an example, figure 6.1 shows the evolution of a sample containing CMP (2 weeks, 1 and 2 months ageing).

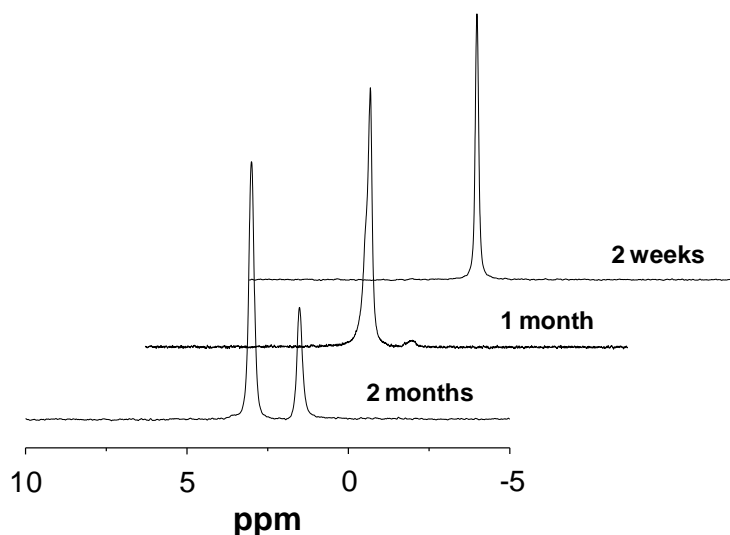


**Figure 6.1**  $^{31}\text{P}$  NMR stack plot spectra of a cubic MO/D/CMP sample (30 wt% water content) recorded upon ageing.

Samples remain apparently homogeneous and isotropic for at least 4 months, afterwards traces of birefringence start to appear at visual inspection through crossed polaroids. Optical microscopy textures and SAXRD patterns indicate the occurrence of a hexagonal phase (see figure 6.2), whereas the  $^{31}\text{P}$  NMR spectra of MO/D/XMP and MO/D/ $\text{Na}_2\text{HPO}_4$  samples show clear CSA features. It is noteworthy that, as revealed by SAXRD analysis, the solubilization of  $\text{Na}_2\text{HPO}_4$  within the water of a MO/W = 70/30 (wt%) cubic phase induces a gyroid-to-diamond transition ( $a = 90 \text{ \AA}$ ) even in the freshly prepared sample. Moreover, also the sample containing the  $\text{Na}_2\text{HPO}_4$  salt becomes hexagonal 4 months after preparation. Therefore, it can be deduced that  $\text{HPO}_4^{2-}$  anion plays a primary role in the phase transition. Since the establishment of a hexagonal arrangement of the interface necessarily requires an increase of the surfactant effective packing parameter, it can be suggested that the hydrogen phosphate dianion works as a bridge between two MO molecules thus favoring a reduction of the polar head area.

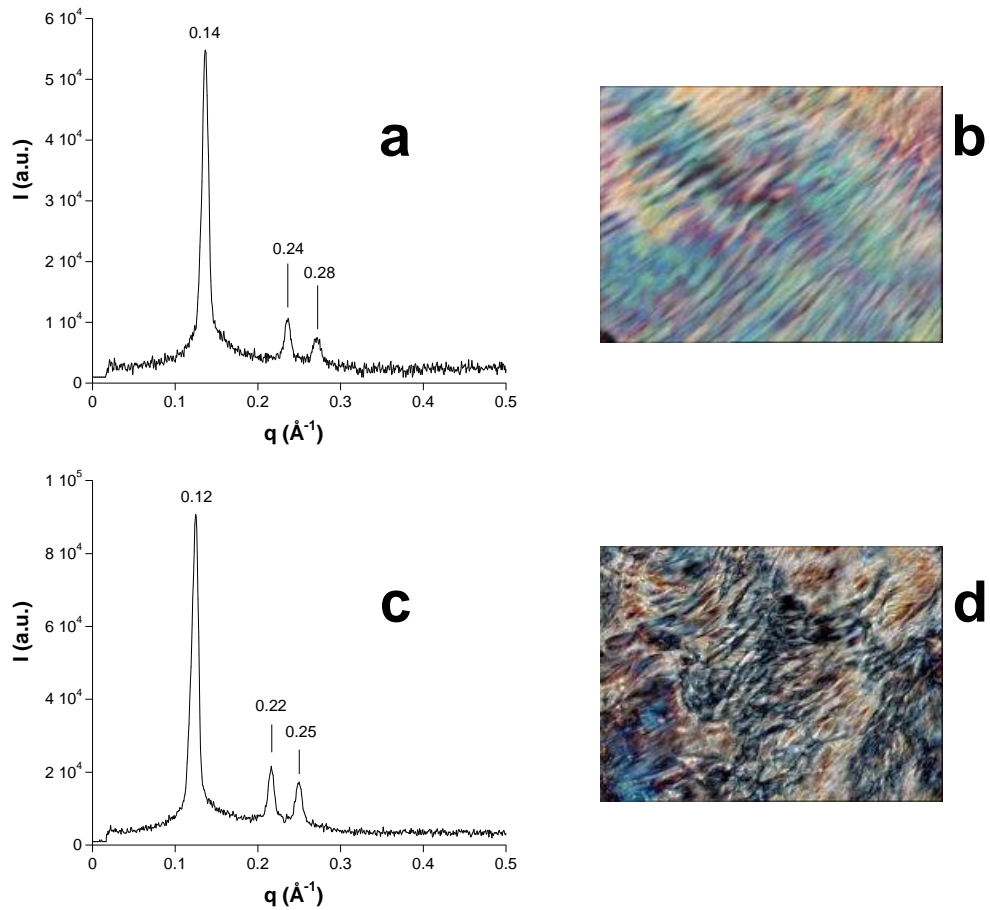


**Figure 6.2** Selected reverse hexagonal SAXRD patterns and optical micrographs at 25 °C of originally cubic samples recorded after 5 months ageing: a), b) MO/D/CMP = 80.8/17.7/1.5; c), d) MO/D/Na<sub>2</sub>HPO<sub>4</sub>= 69.4/29.8/0.8.

Table 6.1 shows the spacing calculated from SAXRD patterns recorded for some selected samples after the cubic-hexagonal phase transition. The water channel radii of the reverse cylinders of these hexagonal phases are calculated according to eq 6.1.<sup>79,80</sup>

$$r_w = a(1 - \Phi_{lip})^{1/2} \left( \frac{\sqrt{3}}{2\pi} \right)^{1/2} \quad \text{eq. 6.1}$$



Table 6.1 SAXRD data of some selected samples after cubic-to-hexagonal phase transition.

Sample Composition	$\Phi_{lip}$	Space group	$a$ (Å)	$r_w$ (Å)
MO/D/CMP = 80.8/17.7/1.5	0.841	H <sub>II</sub>	51.0 ± 0.1	11.1
MO/D/AMP = 59.1/39.4/1.5	0.611	H <sub>II</sub>	61.0 ± 0.1	19.6
MO/D/Na <sub>2</sub> HPO <sub>4</sub> = 69.4/29.8/0.8	0.725	H <sub>II</sub>	56.0 ± 0.1	15.4

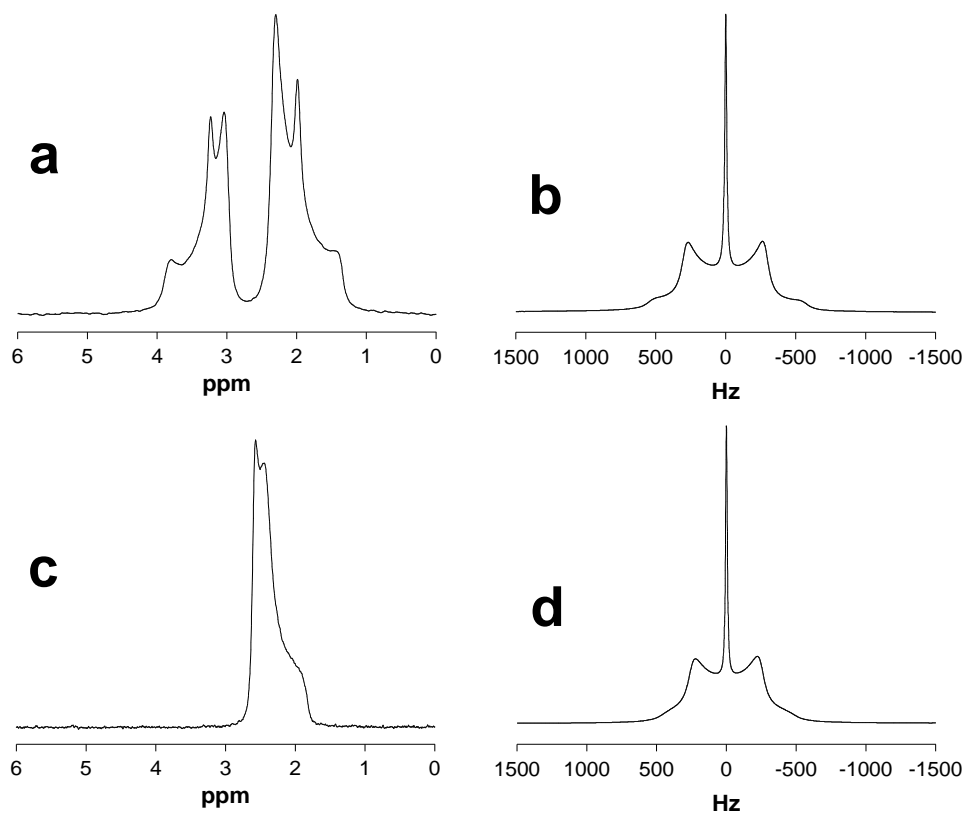


Figure 6.3 NMR spectra showing the cubic-to-hexagonal phase transition induced by the XMP hydrolysis and the HPO<sub>4</sub><sup>2-</sup> anion. MO/D/UMP sample after 5 months ageing: a) <sup>31</sup>P NMR spectrum, b) <sup>2</sup>H NMR spectrum; MO/D/Na<sub>2</sub>HPO<sub>4</sub> sample after 4 months ageing: c) <sup>31</sup>P NMR spectrum, d) <sup>2</sup>H NMR spectrum.

Figure 6.3 shows the  $^{31}\text{P}$  and the  $^2\text{H}$  NMR spectra of MO/D/UMP and MO/D/ $\text{Na}_2\text{HPO}_4$  samples collected few months after their preparation. Taken all the previous considerations together the impressive  $^{31}\text{P}$  NMR pattern of the MO/D/UMP sample (emblematic for all the MO/D/XMP systems) shown in figure 6.3a can be easily interpreted as follows.

As previously discussed, the hydrolysis of XMP bases can be accounted for by the formation of the hydrogen phosphate dianion which originates a new upfield NMR signal at first. Then, the cubic LC phase becomes hexagonal. Therefore, the spectrum in figure 6.3a is representative for a two-phase regions sample where the nucleotide and its hydrolysis product are incorporated both in the cubic phase still present (as revealed by the isotropic signal) and in the coexisting hexagonal phase (recognizable via the CSA feature). The coexistence of the two phases is furthermore corroborated by the isotropic signal superimposed to the deuterium quadrupolar splitting reported in figure 6.3b. Note that, as already observed in the  $L_\alpha$  phase, here the  $^{31}\text{P}$  CSA of UMP is opposite (negative  $\Delta\sigma$  value) to what commonly reported for phosphate bearing molecules entrapped in a hexagonal phase. On the contrary, the upfield signal shows the expected CSA orientation as in the case of MO/D/ $\text{Na}_2\text{HPO}_4$  two-phase sample (see figure 6.3c,d). It should be stressed that, differently from the lamellar, in the hexagonal phase the XMPs are not sterically forced to assume a preferential orientation since here the water channels are large enough to suitably accommodate the mononucleotides (see table 6.1). Therefore, the peculiar orientations demonstrated by the  $^{31}\text{P}$  CSA must reflect specific interactions (via hydrogen bond) with the MO polar head experienced by the XMPs and their hydrolysis product at the interface. In other words, in the hexagonal phase, the XMPs adhesion to the MO interface is revealed by the CSA interaction itself. In fact, if the XMP molecules were simply dispersed within the water channels the rapid molecular motions would mediate the CSA to zero. It is noteworthy that also the  $\text{HPO}_4^{2-}$  anion

displays a preferential orientation in the hexagonal phase, that, again, indicates a close interaction with the MO interface.

Evidences of the existence of such hydrogen bonds in the cubic phases were indirectly obtained by comparing the self-diffusion coefficients of the nucleotides in XMPs 0.2 M  $^2\text{H}_2\text{O}$  solutions and in the cubic phases. Results are shown in table 6.2. To put these results into an appropriate context it is worth considering that a realistic modeling of the mononucleotides adhesion to the interface should imply two different diffusional states of the XMPs. Although with the constraint of a mono-dimensional displacement induced by the *la3d* topology, XMPs may experience either free (within the bicontinuous water channels) or hindered diffusion (when bound to the MO polar head). In such a case the observed self-diffusion coefficient ( $D^{obs}$ ) would be a weighted value expressed as

$$D^{obs} = pD^{bound} + (1-p)D^{free} \quad \text{eq. 6.2}$$

where  $D^{free}$  and  $D^{bound}$  represent the XMPs self-diffusion coefficient in the free and the bound state respectively, and  $p$  indicates the molar fraction of molecules bound to the interface.

In the absence of specific interactions, in a bicontinuous cubic environment, theory predicts a 2/3 reduction of  $D^{free}$  only. Clearly, this is not the case. Conversely, since  $D^{free}$  and  $D^{bound}$  commonly differ for at least one order of magnitude, the observed self-diffusion coefficients can properly be explained assuming that a significant fraction of XMPs tightly adheres to the MO interface.

**Table 6.2 Phosphorous self-diffusion coefficients ( $\times 10^{10} \text{ m}^2 \text{ s}^{-1}$ ) measured in XMPs 0.2 mol L $^{-1}$   $^2\text{H}_2\text{O}$  solutions and in MO/D = 70/30 cubic phases containing 1.5% of XMPs.**

	$^{31}\text{P } D_{\text{AMP}}$	$^{31}\text{P } D_{\text{GMP}}$	$^{31}\text{P } D_{\text{CMP}}$	$^{31}\text{P } D_{\text{UMP}}$
Solution	$2.7 \pm 0.1$	$2.6 \pm 0.1$	$3.3 \pm 0.1$	$3.3 \pm 0.1$
<i>la3d</i> phase	$0.32 \pm 0.02$	$0.33 \pm 0.02$	$0.33 \pm 0.02$	$0.53 \pm 0.03$

Catalyzed by more or less specific enzymes (phosphatases),<sup>81-83</sup> the phosphoester hydrolysis has been a well-known process since many decades and the related thermodynamic and kinetic aspects have been the target of a huge number of studies.<sup>84,85</sup> In principle, the phosphoester hydrolysis may proceed through two distinct mechanisms classified as associative or dissociative. The former implies the attack from a suitable nucleophile (such as a hydroxide ion) to the phosphorus nucleus thus leading to a phosphorane intermediate which in turn eliminates an alkoxide as a leaving group. On the contrary, the dissociative mechanism involves a transient metaphosphate anion that directly leaves the phosphoester with the possible aid of a chemical species capable of stabilizing the transition state for the reaction. As a general rule, the associative mechanism prevails at low pH values, whereas the dissociative one becomes important in neutral or alkaline environment, where the phosphoester exists as the monoanion or the dianion, respectively.<sup>85</sup>

On such a basis, and taking into account that, as previously stated, XMPs tend to adhere to the interface, it can reasonably be hypothesized that the phosphoryl moiety is forced to interact with the primary –OH groups of the MO at the interface. This should substantially favor the formation of a six-membered cyclic transition state, perfectly analogous to that reported as the key step in the water-assisted dissociative hydrolysis of monomethyl phosphate.<sup>86</sup>

Further studies are in progress to obtain deeper insights on the mechanism that regulates the observed mononucleotides hydrolysis. Nevertheless, it can be concluded that XMP molecules undergo a slow hydrolysis process, very likely induced by specific H-bonding mediated interactions between the phosphate moiety and the MO polar interface.

### 6.3 Conclusions

The MO-based LC phases here used can be easily regarded as membrane models as a result of lipid type and bilayer occurrence. These lipid LC systems have been shown to constitute suitable matrices to entrap either hydrophilic nucleotides or amphiphilic nucleolipids, and are therefore promising lipid-based nanovectors to protect and deliver nucleotide-analogue drugs. However a drastically different behavior regarding the long-term stability of the nanodevice is displayed. All these molecules contain a phosphate moiety. It has been ascertained that in the case of the amphiphilic additives, which locate at the MO polar-apolar interface, the MO LC systems were found endowed of high stability, more than two years. Differently, the XMP molecules, which are located in the aqueous domain of the MO LC phases, undergo a hydrolysis process at the phosphoester bond, due to a preferential orientation with respect to the MO interface. The XMPs degradation, within about four months, causes an impressive alteration of the interface arrangement. Indeed, the relatively small amount of  $\text{HPO}_4^{2-}$  anion resulting from the XMPs hydrolysis is sufficient to induce a cubic-to-hexagonal phase transition as a result of different, and specific interactions at the polar-apolar interface that favors a reverse curvature. This conclusion arises from the opposite orientation in the hexagonal phase of the  $^{31}\text{P}$  CSA tensor of XMPs with respect to  $\text{HPO}_4^{2-}$  that evidences a different dislocation of the phosphate group in the proximity of the interface.

Besides the peculiar scientific results, a clear message can be emphasized, particularly for drug molecules such as aptamers: the presence of unesterified phosphate groups in fully hydrophilic drug molecules (for instance our XMPs) may have dramatic effects on the stability of the lipid bilayer of a biological membrane.



## Chapter 7

# Hydrolysis of nucleotides at the *Ia3d* cubic interface. Part 2

### 7.1 Introduction

In the previous chapter it was reported that, when entrapped within a monoolein (MO)-based *Ia3d* cubic phase, AMP, GMP, UMP and CMP nucleotides (adenosine, guanosine, uridine and cytidine 5'-monophosphate disodium salts, respectively) undergo a slow but significant phosphate ester hydrolysis, plainly induced by specific interactions at the monoolein-water interface. Bearing in mind the natural inertness toward hydrolysis displayed by phosphate monoesters dianions in the absence of catalytic agents, such a result was really surprising. In addition, upon ageing a cubic to hexagonal phase transition of the samples was detected at room temperature, while in the MO/water binary system hexagonal liquid crystals form only above 70 °C. Here, kinetics of the hydrolysis reaction and interactions between the lipid matrix and the mononucleotide adenosine 5'-monophosphate (AMP) and its 2'-deoxy derivative (dAMP) are thoroughly investigated in order to shed some light on the mechanism of the nucleotide recognition and phosphate ester hydrolysis. Samples were analyzed through FTIR, NMR and SAXRD techniques.

## 7.2 Results and Discussion

As previously reported on a qualitative base, inclusion of AMP within a MO-based *la3d* cubic phase results in the slow hydrolysis of the ribose-phosphate ester bond caused by specific interactions at the MO-water interface. The occurrence of the hydrolysis reaction was revealed by the growth of a new resonance in the  $^{31}\text{P}$  NMR spectrum upon the samples aging, while the reaction product ( $\text{HPO}_4^{2-}$ ) was basically assessed through the determination of its chemical shift and self-diffusion coefficient.

The present investigation started with some preliminary NMR experiments conducted on a MO/D = 70/30 *la3d* sample containing 1.5 wt % of dAMP to ascertain possible differences at either the macroscopic or the molecular level with respect to the AMP-containing system. As a matter of fact, no differences were noted in the  $^{31}\text{P}$  NMR chemical shifts nor in the self-diffusion coefficient values of the nucleotide, as determined through  $^{31}\text{P}$  NMR PGSTE experiments ( $D_{\text{dAMP}} = (3.1 \pm 0.1) \times 10^{-11} \text{ m}^2/\text{s}$ , to be compared with the value  $D_{\text{AMP}} = (3.2 \pm 0.2) \times 10^{-11} \text{ m}^2/\text{s}$ ).<sup>75</sup> More significantly, in much the same way as AMP, dAMP molecules when entrapped within the water channels of the liquid crystalline matrix undergo the hydrolysis process upon sample aging. These results essentially confirm, on a qualitative basis, that dAMP behaves similarly to AMP.

To shed some light on the reaction mechanism, the hydrolysis of the two nucleotides entrapped in the MO/D *la3d* cubic phase was quantitatively followed by recording the  $^{31}\text{P}$  NMR spectra of the samples at 25 °C over a period of 1 month. In addition, considering the possible biological implications of this study, experiments were repeated at 37 and 42 °C.

Since variations in temperature may induce phase transitions, the temperature dependence of the MO/D = 70/30 samples containing either AMP or dAMP was investigated through SAXRD. Results related to AMP are depicted in Figure 7.1a. The system under study is a pure *la3d* phase up to at least 42 °C, whereas



an *la3d* to *Pn3m* intercubic phase transition takes place starting from 45 °C. A slightly different phase behavior is detected for dAMP, as reported in Figure 7.1b. Actually, in the latter case the phase transition begins at 50 °C. It is here worth noticing that, in the MO/D = 70/30 binary system, this kind of phase transition was not observed up to 55 °C (data not shown). Therefore, from these experiments it can be concluded that interactions of nucleotides with the lipid matrix favor the *la3d* to *Pn3m* phase transition, and this effect is stronger for AMP than for dAMP.

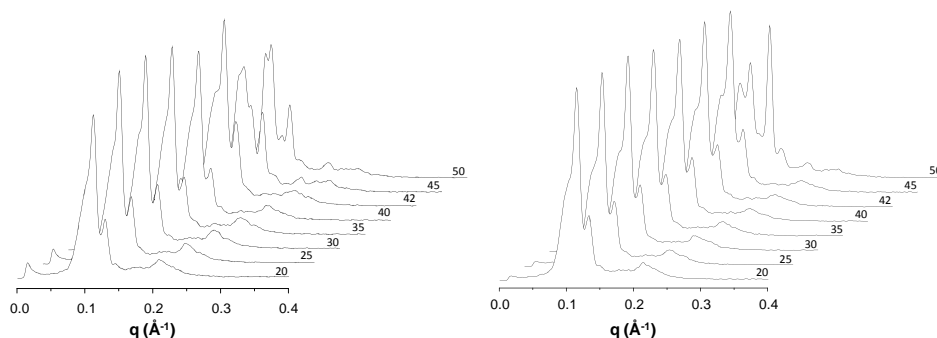


**Figure 7.1** Stack plot of SAXRD diffractograms recorded at different temperatures (reported in °C) of the MO/D = 70/30 *la3d* cubic phase containing either AMP (a, left) or dAMP (b, right).

Results concerning the  $^{31}\text{P}$  NMR quantitative analysis are shown in Figure 7.2. As can be clearly noted, the exponential consumption of AMP and dAMP during the time course confirmed that the hydrolysis reaction occurs as a first-order process with respect to the substrate, meaning that MO acts like a catalyst rather than a reactant. This finding is in agreement with the self-diffusion coefficient value of the hydrolyzed phosphate moiety,<sup>75</sup> which rules out the possibility that the new phosphorus-bearing species is covalently bound to the MO molecules. Accordingly, no changes were observed in the MO  $^{13}\text{C}$  NMR spectra recorded immediately after sample preparations and several months after the conclusion of the experiments.

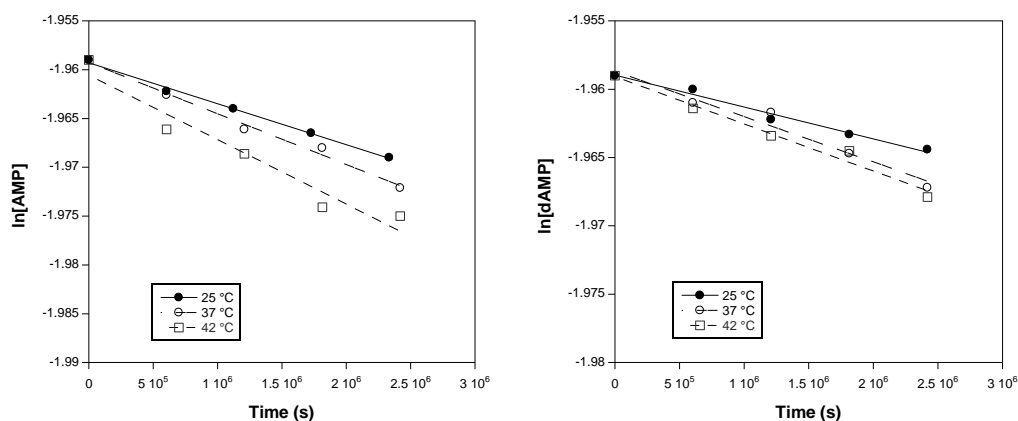


**Figure 7. 2** Kinetic plots obtained at various temperatures for the hydrolysis of 1.5 wt % AMP (left) or dAMP (right) nucleotides entrapped within the MO/D = 70/30 *la3d* cubic phase.

The apparent kinetic rate constants,  $k$ , for both nucleotides were determined by taking the slope of a fitted linear regression curve. Results are reported in Table 7.1.

**Table 7.1** Apparent Kinetic Rate Constants,  $k$  ( $\times 10^9 \text{ s}^{-1}$ ), of the Nucleotide Hydrolysis Reaction Estimated at Different Temperatures, Indicated in  $^{\circ}\text{C}$  as Subscripts (Also Reported Are the Standard Errors Determined by Regression)

Nucleotide	$k_{25}$	$k_{37}$	$k_{42}$
AMP	$4.2 \pm 0.2$	$5.2 \pm 0.3$	$6.6 \pm 0.9$
dAMP	$2.3 \pm 0.2$	$3.3 \pm 0.3$	$3.4 \pm 0.3$

As commonly observed, the rate of the hydrolysis increases as the temperature increases. Nevertheless, and quite remarkably, compared to AMP, the dAMP  $k$  values are almost halved. Repeated experiments gave a percentage error on the estimated  $k$  values around 10%; therefore, the striking difference found for the apparent kinetic rate constants of the two nucleotides should be considered as highly significant. This implies that the simple absence of the hydroxyl group in the 2'-position of the dAMP molecule strongly affects the hydrolysis process rate.

The temperature dependence of a kinetic rate constant is typically described in terms of the Arrhenius equation:  $k = Ae^{-E_a/RT}$ . The activation energy  $E_a$  was evaluated from the Arrhenius plot shown in Figure 7.3. The calculated  $E_a$  values were 18.9 and 18.0 kJ/mol for the AMP and the dAMP molecules, respectively. Although activation energies for the phosphoester bond hydrolysis previously reported in both experimental and theoretical works covered a quite broad range, from 9.5 (for a very efficient inositol monophosphatase)<sup>87</sup> to about 180 kJ/mol,<sup>84,88</sup> values here obtained appear to be rather low. Indeed, it is hard to believe that the system under investigation may lower the activation barrier of the hydrolysis reaction with an efficiency close to that of enzymes, even considering the important role that the discrete water structures found in MO-based cubic phases<sup>89</sup> may express in stabilizing the transition state. Nevertheless, bearing in mind the peculiar morphological characteristics of the cubic phase (which closely resembles that of porous catalysts like zeolites) where the hydrolysis reaction takes place, the observed  $E_a$  values seem less surprising. In fact, these low  $E_a$  values can be considered as the signature of a diffusion-controlled process, a regime where the *measured*  $E_a$  is expected to be lower than that in the absence of diffusion processes which constitute the rate-determining step.<sup>90</sup> Consequently,  $E_a$  values (and  $k$  as well) reported here should be taken as *apparent* rather than absolute.

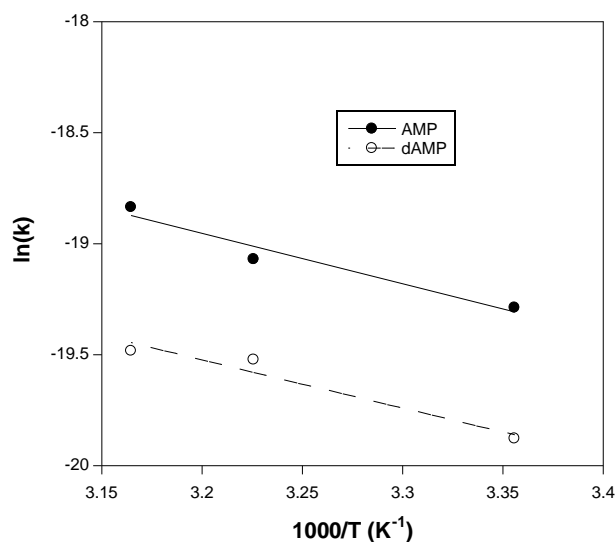


**Figure 7.3. Arrhenius plot of the apparent kinetic rate constants of either 1.5 wt % AMP or dAMP nucleotides entrapped within the MO/D = 70/30 *la3d* cubic phase.**

Though based on three temperatures only, results indicate that the same apparent activation energy pertains to the hydrolysis reaction of both nucleotides and, consequently, strongly suggest that the mechanism underlying the process is the same. Hence, a different probability (enclosed in the pre-exponential factor  $A$ ) in the formation of the reaction intermediates can be called into play to justify the observed apparent kinetic rate constants. Moreover, the MO–water interface undoubtedly plays a crucial role in the reaction mechanism; thus, every reasonable hypothesis aimed at clarifying the retardation in the dAMP hydrolysis should consider the slightly different hydrophilicity of the two nucleotides and its implication on the molecular adhesion and displacement at the lipid interface. This deduction can be corroborated by the FT-IR analysis of the samples.

The FT-IR spectrum of the *la3d* cubic phase with composition MO/D = 70/30 is shown in Figure 7.4. FT-IR spectra of lipid aggregates are conveniently analyzed by separately observing the hydrophobic acyl chain and the hydrophilic headgroup regions. The stretching mode of CH=CH can be found at  $3004\text{ cm}^{-1}$  and the

symmetric stretching mode of the methylene group at  $2853\text{ cm}^{-1}$ .<sup>91,92</sup> The methylene wagging modes of *n*-alkanes are observed in the range  $1330\text{--}1390\text{ cm}^{-1}$ .<sup>57,93-95</sup> The bands of interest represent the *gauche-trans-gauche* (kink,  $1368\text{ cm}^{-1}$ ), double *gauche* (gg,  $1353\text{ cm}^{-1}$ ), and end *gauche* (eg,  $1341\text{ cm}^{-1}$ ) conformations. The bending of terminal  $\text{-CH}_3$  (umbrella mode) is found at  $1378\text{ cm}^{-1}$  and can be used for normalization of other intensities, being insensitive to the lipids' conformation state.<sup>92</sup> Previous studies<sup>57</sup> suggested that insertion of polar probes into the liquid-crystalline cubic phases could affect the acyl chain order, modifying the proportion of these conformers. However, no significant difference was detected in nucleotides-containing samples, suggesting their possible action to be limited to the polar region. In this region, four major MO vibrational modes can be observed, related to the stretching of the bonds *sn-1* CO-O (ester,  $\sim 1180\text{ cm}^{-1}$ ), *sn-1* C=O (carbonyl,  $\sim 1720$  and  $1740\text{ cm}^{-1}$ , respectively H-bonded and free C=O), *sn-2* C-OH ( $\sim 1120\text{ cm}^{-1}$ ), and *sn-3* C-OH ( $\sim 1050\text{ cm}^{-1}$ ).<sup>70,92,94-96</sup> With regard to the first band, its frequency shifts were proposed as a result of a slight deviation from the dihedral angle of  $180^\circ$  in  $\text{C}_3\text{-C}_2\text{-C}_1\text{O-O-C}$  segment.<sup>57,95,97</sup> Also in this case, no significant changes were observed because of inclusion of mononucleotides within the liquid-crystalline cubic phases. Analogous results were also recorded for *sn-1* C=O bands, in good agreement with previously reported studies on protein inclusion on similar lipid phases.<sup>57</sup> In that work, a low-frequency shift of the *sn-3* C-OH band was correlated with more polar surroundings of the bond. In the samples under investigation, as reported in Table 7.2, a similar significant shift was observed only for the *sn-2* C-OH band, apparently suggesting a similar effect.

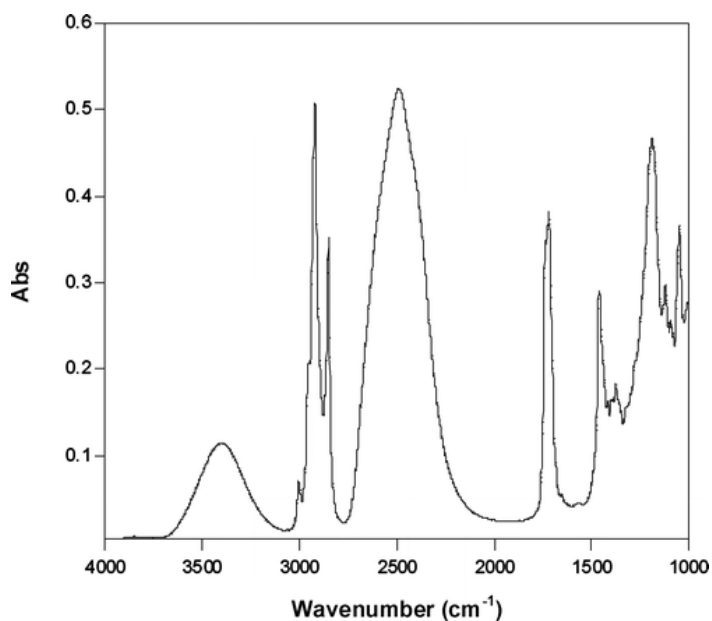


Figure 7.4 FT-IR spectrum of the *Ia3d* cubic phase with composition MO/D = 70/30 at  $T = 25\text{ }^{\circ}\text{C}$ .

Table 7.2 Peak Frequencies and Bandwidths of Lipid Alcoholic *sn*-2 and *sn*-3 C–OH Bands in MO/D = 70/30 Cubic Samples Also Containing 1.5 wt % of Nucleotide

sample	peak frequency <sup>a</sup> (cm <sup>-1</sup> )	bandwidth <sup>a</sup> (cm <sup>-1</sup> )	band
MO/D	1121.2	17.1	<i>sn</i> -2 C–OH
MO/D/AMP 1.5 wt %	1120.3	18.5	
MO/D/dAMP 1.5 wt %	1120.2	17.9	
MO/D	1050.8	25.7	<i>sn</i> -3 C–OH
MO/D/AMP 1.5 wt %	1051.0	24.4	
MO/D/dAMP 1.5 wt %	1051.1	24.3	

<sup>a</sup> Uncertainty is lower than  $\pm 0.1\text{ cm}^{-1}$ .

More remarkable information on the nucleotide interactions with the MO polar head was obtained from the changes induced on the *sn*-2 and *sn*-3 C–OH bandwidths.

While it was previously noted that cytochrome *c* inclusion in MO cubic phases broadened both bands,<sup>57</sup> here a diverse effect on *sn*-2 and *sn*-3 C–OH bands was observed. Indeed, the former was broadened by the presence of both AMP and

dAMP, but to different extents. Conversely, a noteworthy narrowing of the latter was detected in both nucleotide-containing samples. These experimental findings can be associated with a close interaction between MO polar heads and nucleotides. The absence of the 2'-hydroxyl group somewhat modifies the degree of this interaction.

On the whole, FT-IR data indicate that inclusion of 1.5 wt % of nucleotide does not affect the organization of the cubic-phase hydrophobic portion. On the contrary, nucleotides/MO interactions take place at the lipid polar head region, with the specific involvement of the *sn*-2 and the *sn*-3 alcoholic OH groups. Particularly, the measured variations in the bandwidths of these groups suggest that the nucleotides/interface interactions are stronger for AMP than dAMP. However, since only small differences were observed between AMP- and dAMP-containing cubic phases, it can be concluded that very similar interactions occur in both samples.

In order to further clarify the subtle interactions occurring between the nucleotides and the MO interface, two samples with composition MO/D = 70/30 and containing 6.0 wt % of either AMP or dAMP were also prepared. As revealed by SAXRD analysis (see Figure 7.5), the inclusion of such an amount of nucleotides within the cubic samples is sufficient to induce the occurrence of a *Pn3m* cubic phase, even in freshly prepared samples. It deserves note that this kind of intercubic transition is identical to that provoked by the addition of 0.8 wt % of Na<sub>2</sub>HPO<sub>4</sub> to the MO/D = 70/30 cubic phase.<sup>75</sup>

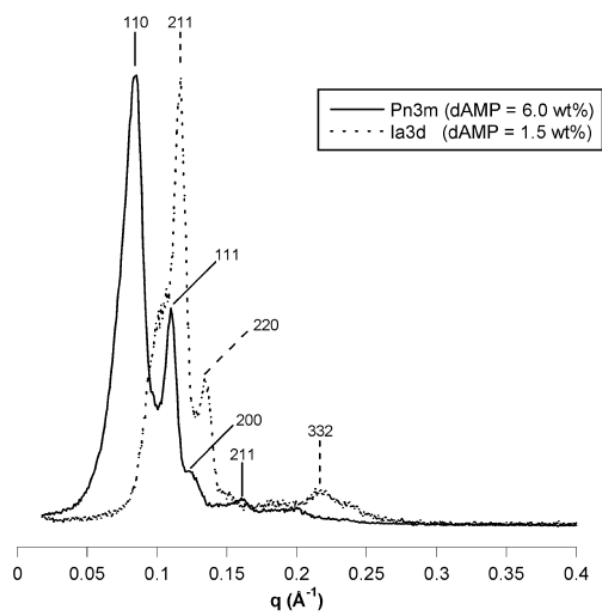
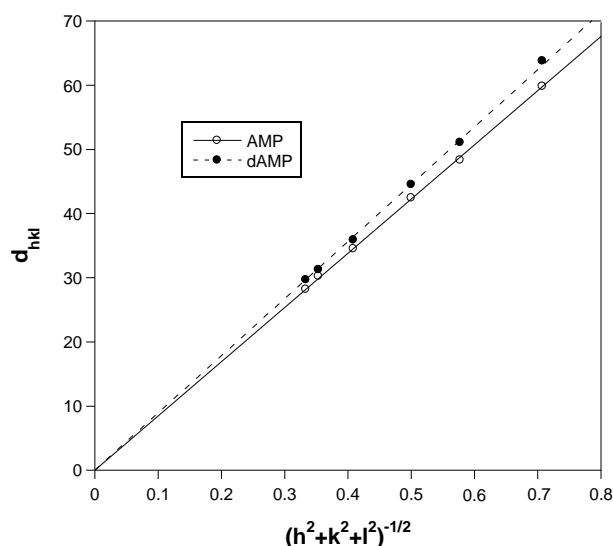


Figure 7.5 SAXRD diffractograms at  $T = 25\text{ }^{\circ}\text{C}$  of samples with composition MO/D = 70/30 containing 1.5 wt % (dotted line) and 6.0 wt % (continuous line) of dAMP. The Miller indices  $hkl$  are given for each reflection.

FT-IR measurements performed on samples containing 6.0 wt % of nucleotides were affected by a high uncertainty due to the growing phosphate peak in the proximity of the *sn*-2 and *sn*-3 OH peaks.





**Figure 7.6** Plot of  $d_{hkl}$  (Å) vs  $(h^2 + k^2 + l^2)^{-1/2}$  of the reflections observed in the SAXRD analysis of the *Pn3m* samples obtained loading the MO/D = 70/30 system with either 6.0 wt % AMP or dAMP.

Turning the attention to the SAXRD data, the structural investigation of the *Pn3m* phase gives, from the linear fit of the  $d_{hkl}$  vs  $(h^2 + k^2 + l^2)^{-1/2}$  plot reported in Figure 7.6, the lattice parameters  $a = 84.5 \pm 0.4$  and  $89.1 \pm 0.6$  Å (correlation coefficients  $r_{AMP} = 0.9998$  and  $r_{dAMP} = 0.9994$ ) and water channel radius  $R_w = 16.0$  and  $17.9$  Å for the AMP- and dAMP-containing systems, respectively. Recalling here that the hydrophobic portion of the cubic phase remains unaltered by inclusion of the nucleotides (from the FT-IR analysis), and since the  $v/a_0$  ratio is bigger for the *Pn3m* than for the *Ia3d* cubic phase,<sup>98</sup> the observed phase behavior necessarily requires a decrease of the effective polar head area. This fact is in accordance with the proposed mechanism for the phase transition, which entails a phosphate bridging between two MO molecules that favors the reduction of the polar head area. Nevertheless, the small differences in  $a$  and  $R_w$  values, assessed through the SAXRD analysis, strongly suggest different specific interactions of the two nucleotides, as dictated by the presence/absence of the hydroxyl group in the 2'-position. Indeed, these results implicitly support the existence of stronger interactions between the

MO interface and AMP with respect to dAMP since a decrease of the (reverse) interface curvature (smaller  $R_w$ ) can be assumed as a straightforward consequence of a greater  $v/a_0l$  ratio. This result perfectly matches the previously discussed nucleotides-induced effects on the temperature dependence of the phase transition (cf. Figure 7.1) and hydrolysis rate (cf. Table 7.1 and Figure 7.2) observed in the two MO/W/(d)AMP systems.

$^{31}\text{P}$  NMR PGSTE experiments on cubic samples loaded with 6.0 wt % of either AMP or dAMP yield self-diffusion coefficients of  $(1.20 \pm 0.06) \times 10^{-11} \text{ m}^2/\text{s}$  for both nucleotides. Compared with the self-diffusion coefficient of  $(3.2 \pm 0.2) \times 10^{-11} \text{ m}^2/\text{s}$  measured for the AMP molecules in an *Ia3d* cubic phase containing 1.5 wt % of nucleotide, this value indicates that nucleotides diffusion is reduced to about one-third. This experimental finding deserves some consideration.

The concept that underpins the study of the molecular motions is based on the simple observation that the self-diffusion coefficient of a molecule is altered by a specific interaction with another molecule or by a restriction of the molecular displacement. In the present investigation, molecular motions within the bicontinuous cubic environment are subjected to the monodimensional constraint imposed by the peculiar topology of these systems. Therefore, with respect to molecules that can freely move along all possible directions (e.g., in a water solution), since they are forced to move within the water channels, a two-thirds reduction of the self-diffusion coefficient is predictable (and usually observed) for molecules residing within *Ia3d* or *Pn3m* cubic phases. Moreover, if specific interactions causing molecules to bind to the interface occur, a further decrease of the observed  $D$  value ( $D^{\text{obs}}$ ) is expected according to the well-known Lindman equation:

$$D^{\text{obs}} = pD^{\text{bound}} + (1-p)D^{\text{free}} \quad \text{eq. 7.1}$$

where  $p$  is the molar fraction of the molecules bound to the interface while  $D^{\text{bound}}$  and  $D^{\text{free}}$  represent the molecules' self-diffusion coefficients in the bound and free states.

Slightly overestimated  $p$  values may be calculated from eq 7.1, assuming that the nucleotide  $D^{\text{bound}}$  equals the MO self-diffusion coefficients. These were assessed through  $^1\text{H}$  PGSTE measurements and found equal to  $(1.12 \pm 0.04) \times 10^{-11}$  and  $(0.90 \pm 0.03) \times 10^{-11} \text{ m}^2/\text{s}$  in the *la3d* and *Pn3m* cubic phases, respectively, containing 1.5 and 6.0 wt % of nucleotide. Therefore, taking one-third of the  $D$  value measured for the nucleotides in a 0.2 M water solution ( $(2.68 \pm 0.06) \times 10^{-10} \text{ m}^2/\text{s}$ ) as  $D^{\text{free}}$ ,  $p$  values of 0.73 and 0.96 were calculated for the *la3d* (1.5 wt % of nucleotide) and *Pn3m* (6.0 wt % of nucleotide) cubic phases, respectively. Within the uncertainties posed by the assumptions made, these values undoubtedly show the high affinity of the nucleotides for the lipid interface and, at the same time, evidence the shift toward the bound state of the nucleotide upon increasing its concentration.

A 4-fold increase of the nucleotide concentration along with a stronger binding to the MO interface would have resulted in an increase of the hydrolysis rate. Surprisingly, the opposite effect was observed. Indeed, even after 2 months, no hydrolysis was detected in both AMP- and dAMP-loaded MO/W samples. Nevertheless, as noted for the case of the cubic phases containing 1.5 wt % of nucleotide, samples remain isotropic for at least 1 month, and then traces of birefringence start to appear at visual inspection through crossed polaroids. These apparently counterintuitive results can be properly contextualized as follows.

The *la3d* to *Pn3m* intercubic transition was previously observed in freshly prepared samples upon 0.8 wt % addition of  $\text{Na}_2\text{HPO}_4$ .<sup>75</sup> Here, the same effect can be observed upon 6.0 wt % addition of (d)AMP. These findings lead to the logical conclusion that both nucleotides and their hydrolysis products can be called into play for the phase transition, but the hydrogen phosphate anion accelerates this process. On the other hand, to explain the absence of hydrolysis detected in *Pn3m* samples, it is necessary to admit that the different local constraints imposed at the lipid molecules in the double diamond liquid-crystalline phase do not allow the mechanism at the basis of the hydrolysis reaction to be explicated.

### 7.2.1 Mechanism of the Hydrolysis Reaction

Both AMP and dAMP uncatalyzed hydrolysis was found to be extraordinarily slow, regardless of the presence or absence of 2'-OH. However, their phosphoester bond can easily be hydrolyzed by some enzymes known as 5'-nucleotidases that have been studied in detail.<sup>99</sup> Chemical, base-catalyzed hydrolysis of the 5'-phosphoester linkage is a well-known phenomenon for di- and polyribonucleotides such as RNA, where the 2'-OH gives an anchimeric assistance for the hydrolysis of the 5'-ester linkage with the *adjacent* ribose. The reaction goes through a 2',3'-cyclic phosphoester, and the reaction product is a mixture of 3'-and 2'-monoesters. Also the enzyme ribonuclease uses a quite similar mechanism where the base is a histidine residue in the active site, but the 3'-monoester is the sole reaction product. Clearly, the deoxyribonuclease uses a completely different mechanism, as DNA lacks any 2'-OH that the enzyme could exploit. In contrast to RNA, DNA is resistant against base-catalyzed hydrolysis of its phosphodiester linkages: that is probably why Nature has selected the comparatively stable DNA for the storage of genetic information, whereas the more reactive mRNA is well suited for temporary information transport. In the present work, it was found that inclusion of AMP and dAMP (as the respective disodium salts) within a MO-based *Ia3d* cubic phase had some unexpected consequences: (i) both AMP and dAMP were hydrolyzed at rates that were found to be exceptionally high when compared to those observed under similar conditions of pH, temperature, and concentration in aqueous solutions; (ii) hydrolysis reaction proceeded much faster for AMP- than for dAMP-containing samples; (iii) both nucleotides were effective in reducing the MO polar head area, thus inducing either the intercubic or the cubic to hexagonal phase transitions; (iv) the former is accelerated by the hydrogen phosphate dianion arising from AMP/dAMP hydrolysis under the described conditions; (v) the high concentration (6.0 wt %) of AMP and dAMP used in the second series of experiments induced an intercubic phase transition, even in freshly prepared samples; (vi) the *Pn3m* cubic phase obtained

under these conditions did not present nucleotide hydrolysis rates comparable to those observed with the *la3d* cubic phase. Possibly, hydrolysis does not occur at all. These findings trigger a number of considerations that could add information to the fascinating topic of phosphorylation/dephosphorylation control in biological contexts. The straightforward conclusion that can be drawn from the results outlined above is that the *la3d* cubic phase was specifically responsible for the observed hydrolysis. This deduction is corroborated by FT-IR and self-diffusion experiments that highlight the existence of specific interactions between the oxygen atoms of the phosphate moieties of the nucleotides and the hydroxyl groups of monoolein. The finding that specific interactions between phosphoesters and hydroxyl-containing molecules could take place, and in certain cases catalyze hydrolysis, is not new. Such a catalytic activity was definitely found for lanthanum hydroxide gels<sup>100</sup> (where the hydroxide character of the hydroxyl groups should be relatively low). Also ascorbic acid was found capable of promoting phosphoester hydrolysis (although in some cases it acts as a hydrolysis inhibitor!).<sup>100</sup>

It is also worth noticing that the nucleotide phosphoryl was not transferred onto whatever nucleophile was present in our system (water, monoolein, and (deoxy)ribose hydroxyl groups), but exclusively to water: no transphosphorylation products were found at all, but only (deoxy)adenosine and hydrogen phosphate dianion. The last observation, taken together with the others above, indicates that a hydroxyl group of monoolein is involved in the phosphoester bond hydrolysis through a dissociative mechanism (possibly through a six-membered transition state): indeed, if the same hydroxyl group was involved in the formation of a phosphorane-like intermediate (thus following an associative mechanism), a phosphorylated monoolein should be the main reaction product. As a point of fact, not even traces of phosphoryl monoolein could be found at the end of the observation time, but only remaining (d)AMP and  $\text{HPO}_4^{2-}$ .

But above all, the most interesting finding of the present study is the sharp difference in the hydrolysis rates of AMP and dAMP: to our knowledge, this is the first report of a substantial difference in the chemical behavior of the two nucleotides, exclusively based on the presence/absence of the 2'-hydroxyl group.

What could be the role of the 2'-OH in substantially enhancing the hydrolysis of AMP with respect to dAMP? On the nucleotides side, it should be envisaged how their inclusion in the *lα3d* cubic phase could force or at least favor one (or more?) conformation, prone to closely interact with the MO-water interface to form the hypothesized key six-membered cyclic transition state. The possible conformations of the investigated nucleotide couple could be *syn* or *anti* with regard to the respective positions of the adenine base and the (deoxy)sugar, the former being more favored in solution whereas the latter may become important within the relatively narrow water channels of the studied phase. At any rate, the putative presence of the more compact *syn* conformation could well favor the close proximity between the phosphoryl moiety and the MO interface but should conceivably be void of any consequence in differentiating between the nucleotide couple AMP/dAMP. With concern to the (deoxy)ribose allowed conformations, the most common are C(3')-*endo* and C(2')-*endo*,<sup>101</sup> also keeping in mind that in dAMP the lack of the 2'-OH relieves some substituent crowding, and therefore the deoxyribose ring is presumably more flexible than the ribose is. On the other hand, in the C(3')-*endo* the 2'-OH would be somewhat less hindered than it would be in the alternative C(2')-*endo* conformation. Plainly, it is difficult to imagine that a *more flexible* molecule is *more hindered* with regard to its interaction with monoolein hydroxyls. Rather, the absence of the 2'-hydroxyl group may account for a different positioning at the interface of the dAMP species, which renders less probable (but not impossible) the formation of the six-membered cyclic transition state that is believed to play a key role in the dissociative phosphoester hydrolysis.

### 7.3 Conclusions

Here, the hydrolysis of two nucleotides included within a cubic lipid matrix, namely AMP and its 2'-deoxy derivative dAMP, and the phase behavior provoked by their interaction with the lipid-water interface were thoroughly investigated.

As demonstrated by the FT-IR experiments, on the lipid side molecular recognition occurs essentially through the *sn*-2 and the *sn*-3 alcoholic OH groups of the MO polar head. Regarding the nucleotides, as indicated mainly by the <sup>31</sup>P NMR self-diffusion measurements, the orthophosphate group is without any doubt involved in the recognition process. Nevertheless, at least to a certain extent, recognition must occur also via the sugar hydroxyl groups, as demonstrated by the dissimilar phase behavior reported for the inclusion of the two nucleotides. Clearly, the stronger or weaker adherence of the nucleotides to the interface caused by the different specific interactions comes into sight as the observed temperature-dependent phase behavior (at 1.5 wt %) and the different structural parameters (at 6 wt %) emphasized by SAXRD.

The nucleotides-induced phase behavior can be visualized as follows. Anchorage of nucleotides to MO molecules at the lipid-water interface via hydrogen bonds reduces the thermal motions of the MO polar heads, thus causing a shrinking of the effective polar head areas. In turn, this phenomenon leads either to the intercubic *Ia3d* to *Pn3m* or to the cubic-hexagonal phase transitions. Upon hydrolysis reaction, the released hydrogen phosphate dianion accelerates the cubic-hexagonal phase transition.

Although far from the extraordinary rate enhancement caused by catalytic activity of enzymes, the nucleotides hydrolysis reaction observed here within the cubic lipid matrix occurs, according to a dissociative mechanism, several orders of magnitude faster than that in aqueous solution. As also suggested by the apparent activation energies, the mechanism underlying the hydrolysis reaction is the same for AMP and dAMP, though the reaction proceeds slower for the latter. This finding highlights a

substantial difference in the chemical behavior of the two nucleotides which has never previously been observed. Remarkably, the hydrolysis mechanism appears to be highly specific for the *Ia3d* phase. In fact, within the limits imposed by the experimental technique used, no hydrolysis was detected in the *Pn3m* phase.

On the whole, the results discussed here evidenced that the function of the lipid matrix constituting the water channel walls may not be just passively structural. Indeed, lipid molecules at the interface can also interact with defined substrates operating as a highly specific catalyst. Such a conclusion becomes particularly significant if the biological role of these bicontinuous cubic phases is taken into account.



## Chapter 8

# Nanoparticles from MO-Based Liquid Crystals: Emulsifier Influence on Morphology and Cytotoxicity

### 8.1 Introduction

In previous works MO based cubic and reverse hexagonal LC phases systems were prepared as lipid nanoparticle (LNP) dispersions stabilized by Pluronic F127 (PF127) as emulsifier.<sup>11,19,102</sup> Surprisingly, cryo-TEM (cryogenic-temperature transmission electron microscopy) and AFM (atomic force microscopy) have shown that this process generates nanoparticles of cubic (cubosomes) and hexagonal (hexosomes) shape.<sup>102,103</sup> Nonetheless, the intrinsic cubic or hexagonal nanostructure, as determined via <sup>13</sup>C NMR relaxation,<sup>104</sup> and SAXRD (Small Angle X-Ray Diffraction)<sup>20</sup> is retained.

This work focuses on the influence of the emulsifier in addressing morphological features and biocompatibility of LNPs prepared through direct fragmentation of a bulk cubic LC phase using a high-speed homogenizer. The kinetic stabilization of the dispersions is achieved through the use of Pluronic F127 (PF127), a non-ionic triblock copolymer PEO-PPO-PEO based on polyethylene oxide (PEO) and polypropylene oxide (PPO), or lauroylcholine chloride (LCh), a short chain cationic surfactant. The morphology and the topology of the LNP dispersions were characterized by cryo-TEM,<sup>105</sup> while the structural arrangement of the interface was investigated via <sup>13</sup>C NMR relaxation techniques. The evaluation of the cytotoxicity was performed using different cell lines, namely mouse 3T3 fibroblasts (M3T3), human epithelial cervical carcinoma (HeLA) and human embryonic kidney (HEK 293T), and two different

procedures based on image analysis after treatment with the fluorescent probes Nile Red and Hoechst, and on the modified Alamar Blue assay.

## 8.2 Results

### 8.2.1 Phase behavior of the bulk liquid crystalline phase

Since polarity, shape, and concentration of additives may induce geometrical and topological modifications on the MO/W system,<sup>106,107</sup> the consequence of the incorporation of both PF127 and LCh on the bulk cubic LC phases used to prepare the nanoparticles dispersion was investigated via SAXRD experiments (Figure 8.1). Consider the two emulsifiers under investigation: in water PF127 (MW = 12,600) forms large micelles that are stabilized by an extensive solvation of the EO groups, while LCh (MW = 321.9) forms very small micelles stabilized by solvation and electrostatic interactions. A MO/W (70/30 w/w) system forms a  $C_G$  cubic phase.<sup>31</sup> In the presence of PF127 and in excess of water the MO/W system evolves towards the  $Pn3m$  phase, coexisting with the  $Im3m$  phase.<sup>108</sup> Figure 8.1a shows the SAXRD diffractogram of a MO/W/PF127 sample containing 6 wt% of PF127 for which the expected combination of  $Pn3m$  (lattice parameter  $a = 90 \text{ \AA}$ ) and  $Im3m$  (lattice parameter  $a = 126 \text{ \AA}$ ) nanostructures is identified. Conversely, the addition of 2-6 wt% of LCh does not modify the original  $la3d$  phase, even in excess of water. The MO/W system in the presence of 3 wt% of LCh shows a large region of lamellar phase ( $L_\alpha$ ) in the range 2-18 wt% of water, a  $L_\alpha + la3d$  two-phase region in the range 18-32 wt% of water, and a pure  $la3d$  phase for water content greater than 32 wt%.

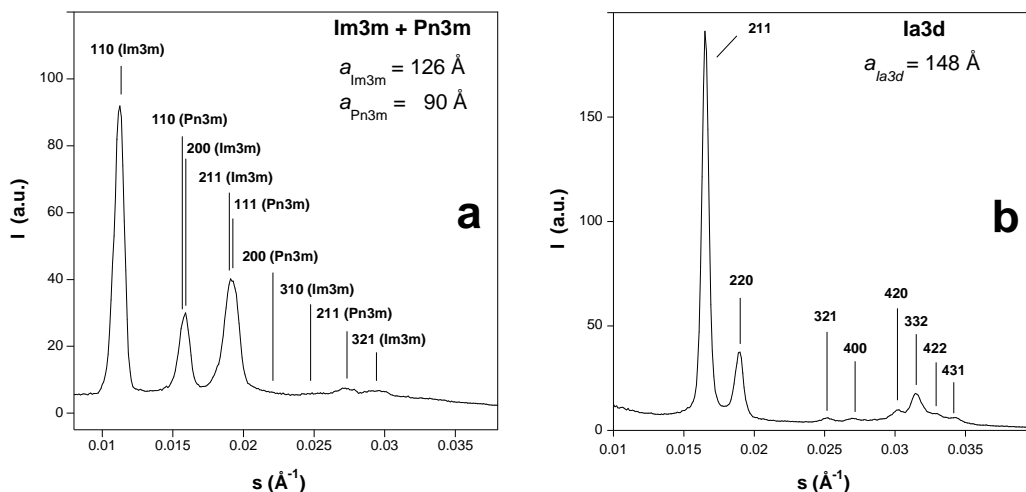


**Figure 8.1** SAXRD patterns at 25 °C. (a) MO/W/PF127 (56.4/37.6/6.0 wt%) sample, (b) MO/W/LCh (60.1/36.9/3.0 wt%) sample. The Miller indices  $hkl$  are given for each reflection.

Figure 8.1b shows the  $Ia3d$  SAXRD pattern of a MO/W sample containing 3 wt% of LCh (lattice parameter  $a = 148 \text{ \AA}$ ). The addition of LCh to MO/W system prevents the formation of the  $Pn3m$  nanostructure due, presumably, to the embedment of the hydrophobic chain among the MO chains. This increase of the hydrophobic volume fraction favors the unexpected existence of a  $Ia3d$  nanostructure also in excess of water.

### 8.2.2 Characterization of the lipid nanoparticles

The LNP dispersions were prepared via the top-down approach. The water-to-dispersed-phase ratio (MO/W = 70/30  $Ia3d$  phase plus the emulsifier) was 95/5 (w/w), while the  $Ia3d$ /PF127 or LCh ratio was 94/6 (w/w). It is worth mentioning that, differently from PF127 that must constitute the 6-20 wt% of the lipid fraction to properly exert its stabilizing function,<sup>19</sup> LCh can be used at only 1-2 wt%. Moreover, the resulting LCh-stabilized dispersions were particularly stable also at temperatures lower than those found for PF127-stabilized dispersions, presumably due to the important electrostatic contribution that prevents the coagulation.

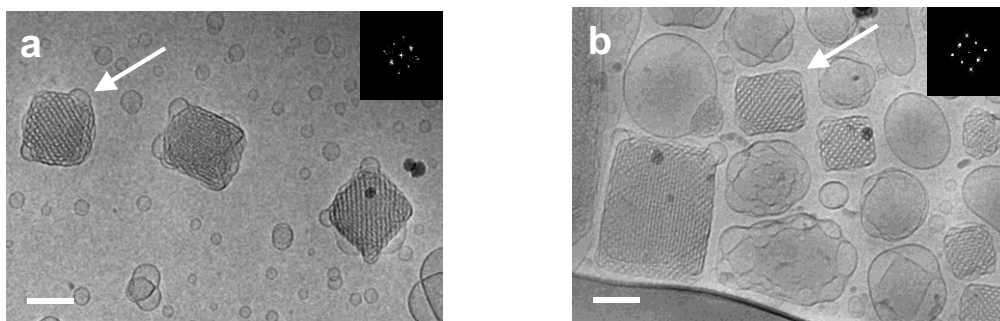


**Figure 8.2 Cryo-TEM images of cubic phase nanoparticles (cubosomes) dispersed in the aqueous solution of PF127. Fast Fourier transformations of the domains indicated by the arrows are shown in the insets. Scale-bars correspond to 100 nm.**

The cryo-TEM images shown in Figure 8.2, typical of the PF127-stabilized LNP sample, show numerous objects with the characteristic shape of cubosomes, along with the vesicular material commonly observed in previous preparations.<sup>13,24,104,109</sup> On the basis of repeated observations, although some cubic particles exceeding 400 nm in size were detected, this LC dispersion was found to be of low polydispersity, with cubosome dimensions estimated in the range 100-200 nm. As often reported for these kinds of dispersions, SAXRD diffractogram was characterized by the absence of clear reflections patterns (data not shown) due to the low number of reflection planes available for each cubosome particle. Nevertheless, the retention of the LC organization of the interface after the dispersion process is strongly corroborated by the inner long-range order well distinguishable in cryo-TEM images, where water channels (bright spots) alternate to oil channels (dark matrix). Moreover, the cubic arrangement may unambiguously be inferred by the Fast Fourier Transform (FFT); insets in Figure 2 show the  $\{110\}$  and the  $\{200\}$  reflections from the cubosomes indicated by the arrows as seen along the  $[100]$  viewing direction of the cubic lattice. Through FFT analysis performed on a number of cubosomes, a mean lattice

parameter of 136 Å was calculated, in agreement with the value previously obtained by SAXRD for the bulk  $Im3m$  LC phase.

Remarkably, the use of LCh leads to an innovative method of preparation of cationic liposomes. Indeed, the dispersion process of the  $la3d$  phase in the LCh aqueous solution induces the formation of a liposome system: in this case the cubic LC nanostructure of the original phases is completely lost.

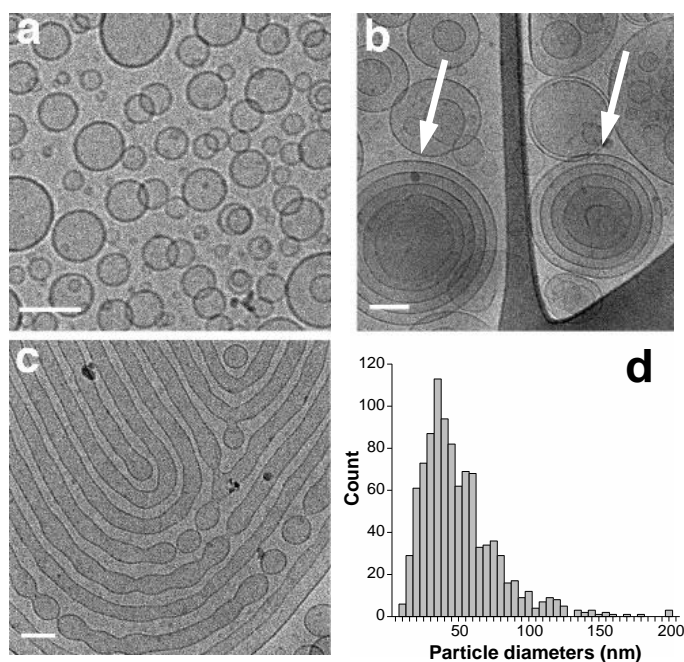


**Figure 8.3** Cryo-TEM images of the LCh-based dispersion showing (a) unilamellar, (b) onion-like (indicated by arrows), and (c) tubular liposomes. Also shown is the unilamellar liposomes size distribution (d). Scale-bars correspond to 100 nm.

As ascertained through cryo-TEM (Figure 8.3), despite the sporadic occurrence of onion-like and tubular liposomes (estimated less than 0.1% of the total particles number), the LCh-stabilized LNP sample mainly consists of a homogeneous dispersion of unilamellar liposomes, characterized by a log-norm size distribution (calculated on 1000 nanoparticles measurements) with a median of about 44 nm (Figure 8.3d). The

bilayer thickness, determined by image analysis, was found of  $36 \pm 3 \text{ \AA}$ , in excellent agreement with values (34-35  $\text{\AA}$ ) elsewhere reported.<sup>75</sup>

The presence of a still structured MO interface was also proven by  $^{13}\text{C}$  NMR relaxation. Figure 8.4 shows the highly resolved  $^{13}\text{C}$  NMR spectra of the dispersions obtained in the presence of PF127 (Figure 8.4a) and LCh (Figure 8.4b) and the spin-lattice  $^{13}\text{C}$  NMR relaxation times measured for the various carbon atoms (Figure 8.4c).

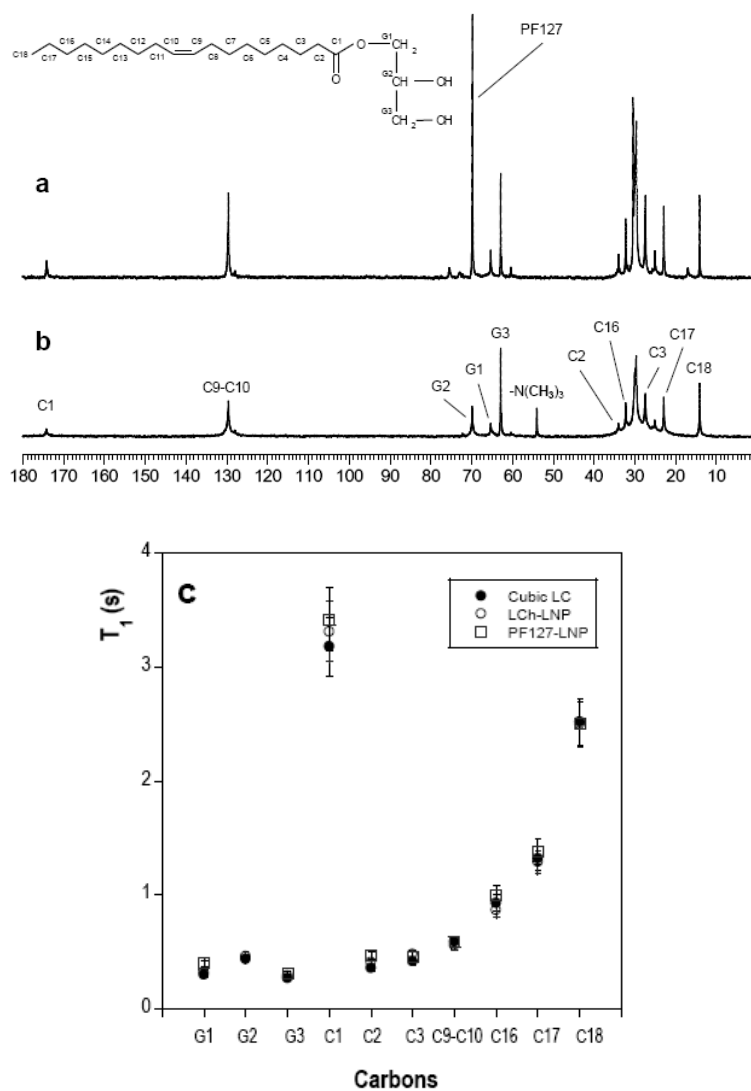


Figure 8.4  $^{13}\text{C}$  NMR data at 25 °C. (a)  $^{13}\text{C}$  NMR Spectrum of the PF127-stabilized LNPs, (b)  $^{13}\text{C}$  NMR Spectrum of the LCh-stabilized LNPs, (c)  $^{13}\text{C}$  NMR spin-lattice relaxation times of the MO/W cubic LC phase (● Cubic LC) and of the LNPs stabilized by PF127 (□ PF127-LNP) and LCh (○ LCh-LNP). Error bars represent standard deviations.

$^{13}\text{C}$  NMR relaxation data demonstrate that the molecular arrangement and the time-dependent interactions are very close in the *Ia3d* LC phase and in the nanoparticle dispersions stabilized either by PF127 or by LCh, despite the different morphologies

and topologies observed by cryo-TEM. Indeed, relaxation times are rather sensitive to modifications of the local intermolecular interactions and to molecular dynamics. Therefore strong alterations of their values are not expected if the aggregates under analysis, though having different-long range order, share the same interfacial arrangement of the bilayer type. As a general comment, it should be noticed that moving from the polar head towards the end of the hydrophobic tail, and independently of the sample, the various carbons show similar mobilities.<sup>110</sup> Most remarkable is the persistence, after the dispersion process, of the local interactions in the polar-head region as well as along the hydrophobic tail of the MO molecules which prove that the bilayer nanostructure is retained in the nanoparticles, as previously demonstrated for cubosomes and hexosomes<sup>104</sup> prepared via different methods.<sup>13,110</sup>

### *8.2.3 Biological assays*

The biological assays to evaluate the impact of these nanoparticles on the cell viability constitute an important aim of this work. Two different methodologies, image analysis and Alamar Blue assay, were applied in investigating the cytotoxicity of the LNPs. Studies were performed using three different cell lines, namely, Swiss 3T3 mouse fibroblasts (3T3), human epithelial cervical carcinoma (HeLa) and human embryonic kidney (HEK 293T) cells. Treatments were applied to actively proliferating cells (1 day after seeding).

In the case of 3T3 cell line observations were made through an inverted fluorescence microscope. Cell integrity was determined, after incubation with the nanoparticle dispersion, by staining for 15 min with the supravital fluorescent probe NR and with Hoechst 33258. NR (9-diethylamino-5H-benzo [ $\alpha$ ] phenoxazine-5-one) is a fluorescent lipophilic dye characterized by a shift of emission spectrum from red to green in the presence of polar and non-polar lipids. Cytoplasmic membranes (mostly composed of phospholipids) are stained by NR red emission (referred to as NR-590)



whereas intracellular lipid droplets (composed of apolar lipids) are stained in NR green emission (referred to as NR-535). Lipid droplets, fat-storing organelle present in all eukaryotic cells, represent an intracellular reservoir of triglycerides and esterified cholesterol.<sup>111,112</sup> Selective determination of cell damage was performed using Hoechst 33258 to visualize cells showing much higher nuclear fluorescence. The assay is based on the assumption that cells apoptosis is preceded by membrane permeability loss and nuclear chromatin condensation. The number of apoptotic cells and the number of healthy cells were counted. Results are expressed as percent ratio of damaged versus total number of cells.

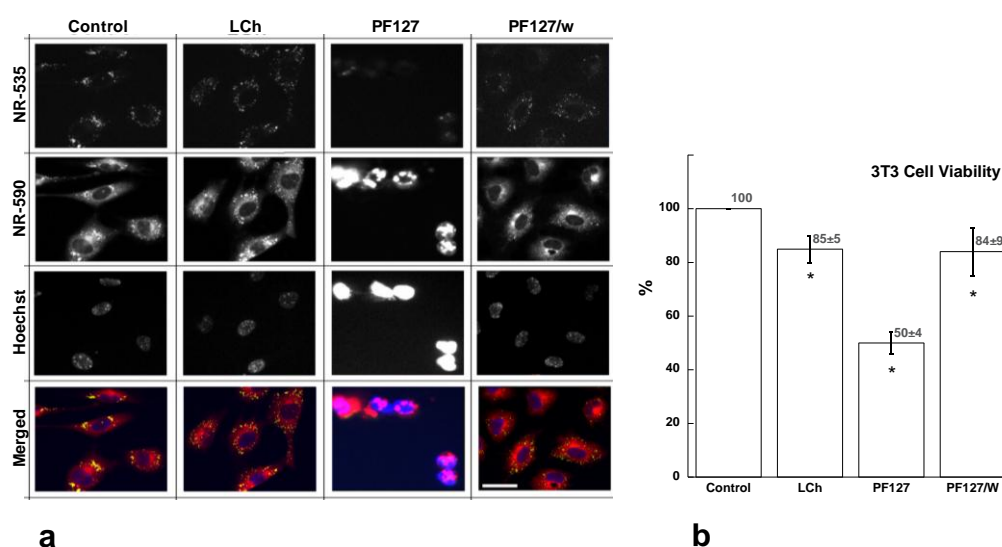
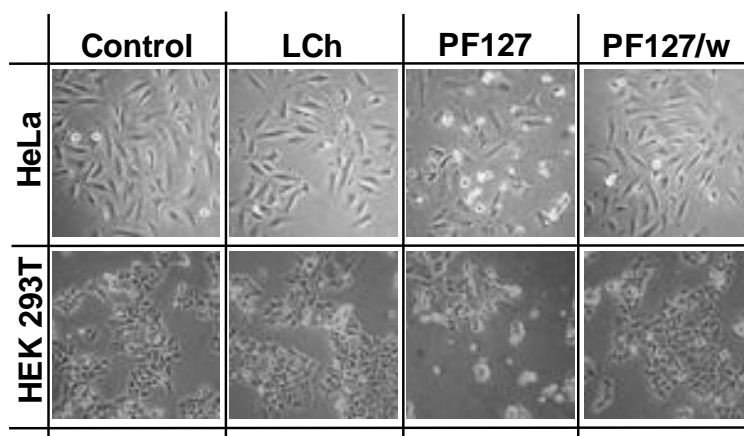


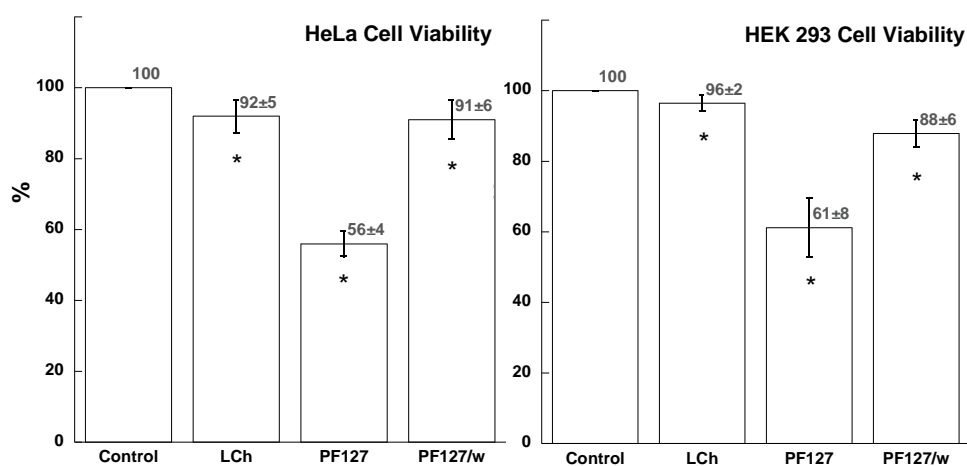
**Figure 8.5** The 3T3 cell line. (a) Effect the MO/W dispersions stabilized by PF127 and LCh. The panel shows the lipid droplets with NR-535, the cytoplasmic membranes with NR-590, DNA stain with Hoechst. Color images were obtained merging NR-535 (green), NR-590 (red) and Hoechst (blue). The scale bar is 30  $\mu\text{m}$ . (b) Effect of the MO/W dispersions stabilized by PF127 and LCh on the cell viability of 3T3 cells as determined from Hoechst 33258 data analysis. (\*)  $p < 0.05$ , compared to non-treated control cells.

Results from these experiments are shown in Figure 8.5a. Surprisingly, LNP dispersions stabilized by PF127 show a remarkable toxicity towards 3T3 cell line, as demonstrated by the images recorded after the treatment with both NR and Hoechst 33258 probes. The global effects of the dispersions stabilized by PF127 and LCh on the viability of 3T3 cells, determined on the basis of observations after 1 h incubation with the different formulations, are summarized in Figure 8.5b. The cytotoxicity of the LNPs stabilized by PF127 is evident. Less than 60% of 3T3 cells are detectable, and most of them show apoptosis/necrosis features. In contrast, LCh-based LNP dispersions as well as the PF127 water solution affect the viability of 3T3 fibroblasts at a much lesser extent.

A different method was used to evaluate the toxicity of the dispersions stabilized by PF127 and LCh in HeLa and HEK 293T cells. Cell viability was assessed by a modified Alamar Blue assay.<sup>113</sup>



**a**



**b**

**c**

**Figure 8.6** The HeLa and HEK 293 cell lines. (a) Morphological analysis of HeLa and HEK 293 cell lines treated with the MO/W dispersions stabilized by PF127 and LCh or PF127 alone in water (PF127/W). The scale bar is 50  $\mu$ m. (b) Effect of the MO/W dispersions stabilized by PF127 and LCh on the cell viability of HeLa cell line (Alamar Blue assay). (c) Effect of the MO/W dispersions stabilized by PF127 and LCh on the cell viability of HEK 293 cell lines (Alamar Blue assay). (\*)  $p < 0.05$ , compared to non-treated control cells.

Figure 8.6a shows representative images of HeLa and HEK cell lines incubated with various formulations as well as the respective controls (untreated cells). As observed

in 3T3 cells, in the case of LNPs stabilized by PF127 a significant toxicity is observed as clearly demonstrated by cell viability reported in Fig. 8.6b and 8.6c. Both HeLa and HEK cell lines retain proliferating capacity of about 60% after incubation with PF127-stabilized LNP dispersions. Formulations stabilized by LCh, as well as the water solution of PF127, in comparison with untreated cells, did not influence cell viability notably.

### 8.3 Discussion

The influence of the emulsifier used to stabilize the LNP dispersion is quite remarkable. Whereas PF127 allows for the formation of cubosomes as reported in previous works,<sup>13,24,104,109</sup> the evolution of the system's nanostructure toward unilamellar cationic liposomes upon LCh addition deserves some comments. In the latter case, the loss of the original cubic liquid crystalline matrix may be explained calling into play the effective packing parameter ( $P_{\text{eff}}$ ).<sup>114</sup> This parameter is defined as the ratio of the volume of the surfactant tail to the product of the cross-sectional area of the surfactant polar head and the length of the surfactant hydrophobic tail. Besides the shape of the surfactant,  $P_{\text{eff}}$  is controlled by a number of factors such as the degree of hydration, the temperature, electrostatic effects and the presence of hydrophobic/hydrophilic guest molecules.<sup>107</sup> Taking into account that MO LC aggregates in water show  $P_{\text{eff}} \geq 1.0$ ,<sup>115</sup> while a suitable  $P_{\text{eff}}$  value for the vesicular arrangement of the bilayer is 0.5-1.0, according to our experimental result it is clear that LCh incorporation into the MO/W system must induce a consistent decrease of  $P_{\text{eff}}$ . This logical deduction is also supported by the broadening of the  $L_{\alpha}$  region and the disappearance of the  $Pn3m$  phase from the pseudo-binary MO/W/LCh diagram ( $Ia3d$  has a smaller  $P_{\text{eff}}$  than  $Pn3m$ ). Moreover, the intercalation of the short-chain LCh molecule within the MO palisade will disturb the regular arrangement of both the lipid tails and the polar head thus increasing the bilayer flexibility. During the dispersion process, these two effects (decreased  $P_{\text{eff}}$  and increased bilayer flexibility)

cooperatively act to allow for the bilayer folding towards the liposomal nanostructure. In conclusion, both the morphology and the topology of the LNPs, obtained here through the direct fragmentation of massive liquid crystalline phases, strongly depend on the chemical nature of the emulsifier. However, due to the peculiar nature of the involved molecules, organized (bilayer) interfaces are still produced. In consideration of the huge interest of this kind of LNPs as carriers in pharmaceutical formulations, the in-vitro evaluation of their biocompatibility seems to be quite important.

Independent of the incubation time used in the different assays, it is clear that PF127-stabilized LNPs induced significant toxicity. Since PF127 dissolved in water does not induce appreciable toxic effects on the three types of cell lines, toxicity should not be ascribed to PF127 itself, that in the various assays always had a concentration in the range 0.5-1.3  $\mu\text{moles/l}$  (i.e., below the cmc of 40  $\mu\text{moles/l}$  at 35 °C), but rather to its combination with the monoglyceride. MO, a membrane lipid, is not expected to exert any toxicity. Since MO promotes bioadhesion and internalization, it can be concluded that MO-based nanoparticles behave as a Trojan horse, thus promoting the internalization of PF127, otherwise less probable. Once inside the cells, PF127 may exert toxic activity towards mitochondrial and nuclear membranes, thus leading to cell death. Although the mechanism that drives cell apoptosis/necrosis is beyond the scope of this paper, it might be expected that this is a consequence of the amphiphilic nature of PF127. Indeed, PF127 has an HLB (hydrophilic-lipophilic balance) number around 24.<sup>116</sup> This implies a tendency to bury the rather large hydrophobic part (about 60 propylenoxide groups) into some biological compartment, for instance into the mitochondrial or the nuclear membranes. This finding is in agreement with the use of various types of Pluronic (for instance P85 of MW around 4600 and HLB in the range of 12-18) to promote chemosensitization in multidrug resistant cancer cells towards antineoplastic agents.<sup>117</sup> In addition, a more hydrophobic variety of Pluronic, Pluronic L81 (MW

2750 and HLB 1-7), was suggested to accumulate in the cytosol thus causing triglycerides (TG) assimilation, and, consequently, inhibition of the microsomal TG transfer protein activity.<sup>118</sup> In the present work the association MO-PF127 decreases the hydrophilicity of PF127, therefore processes similar to those reported for Pluronic P85 and L81 may occur. Although these can partly explain the experimental results, the biological mechanism by which MO/PF127 induces cell apoptosis/necrosis (in terms of involved molecular entities, and specific interactions) is not clear.

Regarding the LNPs stabilized by LCh, it should be highlighted that, besides the role of MO, the bioadhesion process is likely to be functionally driven by molecular recognition between the biological membrane and the cationic polar head of the emulsifier that resembles the behavior of a charged peptide. LCh acts as a cell-penetrating peptide. This additional interaction does not produce any remarkable toxic effect, at least in a short term treatment.

#### **8.4 Conclusions**

Due to the pressing demand for innovative pharmaceutical outcomes endowed of fine-tuned properties, it is expected that lipid based nano-systems will be widely exploited. This is due to their biocompatibility, and, more importantly, to the wide range of possible nanostructures that can modulate both drug entrapment and controlled release.

In this work two different nanoparticle dispersions obtained from the same LC matrix have been formulated and their short term cytotoxicity evaluated. Interestingly, the use of LCh resulted in a new and easy-to-deal-with route to prepare small unilamellar cationic liposomes that contribute to enlarge the class of liposome formulations based on single-chained surfactants. In fact, liposomes are classically obtained using double-chained surfactants (mainly phospholipids), while their counterparts based on single-chained surfactants are much less common (mixtures of cationic and

anionic surfactants, known as catanosome,<sup>119</sup> are an example). The possibility of forming MO-based vesicles in excess of water was already reported, but only highly polydisperse multilamellar large vesicles were obtained.<sup>115,120</sup> As a further remark, it was observed that liposomes with size smaller than 100 nm show decreased uptake by the mononuclear phagocyte system (hence, circulate longer in the blood), thus increasing target efficiency in tumors and favoring therapeutic activity of liposomal antitumor drugs.<sup>121</sup> Therefore, the liposome formulation here reported can be considered as suitable candidate for being used in this field. Indeed, LCh-based LNPs showed very low toxicity towards different cell lines after a relatively short incubation time. On the contrary, the toxicity of the PF127-stabilized LNP dispersion has been demonstrated by means of two different biological assays.

As it is included in the FDA inactive ingredients guide, MO is extensively used as additive in food and pharmaceutical formulations. Moreover, cubosomes may definitely be regarded as the non lamellar analogs of the liposomes. Consequently, the role of both their molecular constituents and their peculiar nanostructures in the observed cell damage can be safely excluded. Therefore, the toxic effect, even though clearly carried out by the synergistic action of MO and PF127, can be entirely ascribed to the non-ionic triblock copolymer. The importance of such an observation resides on the fact that, within the variety of emulsifiers used in cubosome preparation (i.e., bile salts, casein, phospholipids<sup>122</sup> and, very recently, modified cellulose<sup>123</sup>), PF127 is undoubtedly the most common. It deserves also noticing that PF127 is not usually considered a hazardous molecule.

This finding emphasizes the importance of establishing rigorous protocols devoted to assess the possible toxic effects of these innovative nanostructures, also when all constituents are generally recognized as safe.





## Concluding Remarks

In recent years, the liquid crystalline phases formed by polar lipids have been shown to accommodate biologically active molecules such as vitamins, enzymes, and other proteins. This high solubilization capacity opens new opportunities for utilizing liquid crystalline phases in food and pharmaceutical applications.

Among the various liquid crystalline phases that can be formed, the cubic phase is the most fascinating. The unique structure and physicochemical properties makes it suitable as a drug delivery matrix. The ability to incorporate and slowly release a variety of drugs with different physicochemical properties by a variety of routes of administration has been demonstrated. The similarity of cubic phase to physiological lipid membranes and its ability to incorporate and maintain proteins in their native bioactive conformation is a unique attribute, extremely desirable for macromolecule drug delivery.

Adding a third component to MO/W binary system may result in dramatic changes of the microstructure, stability and location of phase boundaries. As shown in chapter 4, the MO/W cubic samples where two different amphiphilic nucleotides (nucleolipids) were dissolved are highly stable and no symptoms of degradation were observed even after 2 years. Conversely, the solubilization of nucleotides in the same system strongly affect the long-term stability of the lipid mesophase, causing a cubic-to-hexagonal phase transition with time (chapters 6-7).

Experimental results evidenced that the function of the lipid matrix constituting the water channel walls of the cubic phase may not be just passively structural, but it can operate as a highly specific catalyst. Indeed, the nucleotide molecules, which are located in the aqueous domain of the MO LC phases, undergo a hydrolysis process at the phosphoester bond, due to a specific interaction between the phosphate-ribose groups and the MO interface. This induces the phosphate moiety to assume a preferential orientation, that is perpendicular to that found for nucleolipids and

phospholipids, at the MO/W interface. Such a conclusion becomes particularly significant if the biological role of these bicontinuous cubic phases along with that of nucleotides is taken into account.

Finally, interfacial phenomena have been shown to be crucial during the preparation of MO-based nanoparticles. Indeed, starting from the same MO/W cubic LC matrix two different types of LNP were obtained, depending on the emulsifier chosen to stabilize the system in water. The kinetic stabilization of the dispersions was achieved through the use of Pluronic F127 (PF127), a nonionic triblock copolymer PEO-PPO-PEO based on polyethylene oxide (PEO) and polypropylene oxide (PPO), or lauroylcholine chloride (LCh), a short chain cationic surfactant. The use of LCh, resulted in a new and easy-to-deal-with route to prepare small unilamellar cationic liposomes. Indeed, they showed very low toxicity towards different cell lines after a relatively short incubation time. On the contrary, a relatively high toxicity was demonstrated for the PF127-stabilized LNP dispersion. The toxic effect, even though clearly carried out by the synergistic action of MO and PF127, can be entirely ascribed to the non-ionic triblock copolymer. The importance of such an observation resides on the fact that, within the variety of emulsifiers used in cubosome preparation (i.e., bile salts, casein, phospholipids and, very recently, modified cellulose), PF127 is undoubtedly the most common. It deserves also noticing that PF127 is not usually considered a hazardous molecule.

## Acknowledgements

It is a pleasure to thank many people who made this thesis possible.

First of all, I would like to thank my supervisor Maura Monduzzi for giving the opportunity to do PhD and for supporting and encouraging me during the last three years.

I must give special thanks to Sergio Murgia, for introducing me to the world of NMR spectroscopy and for fruitful discussions, allowing me to grow through my work.

Also, thanks to my colleagues Rossella, Pradip, Maura, Marianna, Francesca, and to all the members of the Biocatalysis group.

I would like to thank all the co-authors of the publications included in this thesis, in particular Debora Berti who assisted me during my SAXRD experiments in Florence.

Thanks also to Marco Piludu and Monica Piras for preliminary TEM analysis.

A special thank to my family, Fabrizio and all the friends who always supported, encouraged and gave thoughtful advice.

Thanks are due to Projects MIUR DM28142 of the Sardinian Biomedicine District, MIUR Prin 2008, grant number 2006030935, for financial support. Sardegna Ricerche Polaris is thanked for free access to the instruments belonging to the Nanobiotechnology laboratories. In addition thanks are due to CSGI and CNBS for general expertise support.



## References

- (1) Schwartz, A. M.; Perry, J. W.; Bartell, F. E. *The Journal of Physical Chemistry* **1949**, *53*, 1467-1467.
- (2) Schwartz, A. M.; Perry, J. W.; Berch, J. *Surface Active Agents and Detergents: Volume II*; RE Krieger Pub. Co., 1977.
- (3) Evans, D. F.; Wennerström, H. *The colloidal domain: where physics, chemistry, and biology meet*; Wiley-VCH New York, 1994.
- (4) Tanford, C. *The Hydrophobic Effect: Formation of Micelles and Biological Membranes 2d Ed*; J. Wiley., 1980.
- (5) Mitchell, D. J.; Ninham, B. W. *J. Chem. Soc. Faraday Trans. II* **1981**, *77*, 601.
- (6) Hyde, S.; Andersson, S.; Larsson, K.; Blum, Z.; Landh, T.; Lidin, S.; Ninham, B. W. *The Language of Shape*; Elsevier: Amsterdam, 1997; Vol. chap. 1-5.
- (7) Drummond, C. J.; Fong, C. *Current Opinion in Colloid & Interface Science* **1999**, *4*, 449-456.
- (8) Larsson, K. *Current Opinion in Colloid & Interface Science* **2009**, *14*, 16-20.
- (9) Spicer, P. T. *Current Opinion in Colloid & Interface Science* **2005**, *10*, 274-279.
- (10) Yaghmur, A.; Glatter, O. *Advances in colloid and interface science* **2009**, *147*, 333-342.
- (11) Barauskas, J.; Johnsson, M.; Tiberg, F. *Nano Lett.* **2005**, *5*, 1615-1619.
- (12) de Campo, L.; Yaghmur, A.; Sagalowicz, L.; Leser, M. E.; Watzke, H.; Glatter, O. *Langmuir* **2004**, *20*, 5254-5261.
- (13) Gustafsson, J.; Ljusber-Wahren, H.; Almgren, M.; Larsson, K. *Langmuir* **1997**, *13*, 6964-6971.
- (14) Larsson, K. *Curr. Opin. Colloid Interface Sci.* **2000**, *5*, 64-69.
- (15) Spicer, P. T.; Hayden, K. L.; Lynch, M. L.; Ofori-Boateng, A.; Burns, J. L. *Langmuir* **2001**, *17*, 5748-5756.
- (16) Dong, Y.-D.; Larson, I.; Hanley, T.; Boyd, B. J. *Langmuir* **2006**, *22*, 9512-9518.

- (17) Yagmur, A.; de Campo, L.; Sagalowicz, L.; Leser, M. E.; Glatter, O. *Langmuir* **2005**, *21*, 569-577.
- (18) Barauskas, J.; Misiunas, A.; Gunnarsson, T.; Tiberg, F.; Johnsson, M. *Langmuir* **2006**, *22*, 6328-6334.
- (19) Barauskas, J.; Johnsson, M.; Joabsson, F.; Tiberg, F. *Langmuir* **2005**, *21*, 2569-2577.
- (20) Nakano, M.; Sugita, A.; Matsuoka, H.; Handa, T. *Langmuir* **2001**, *17*, 3917-3922.
- (21) Spicer, P. T.; Hayden, K. L.; Lynch, M. L.; Ofori-Boateng, A.; Burns, J. L. *Langmuir* **2001**, *17*, 5748-5756.
- (22) Landh, T.; Larsson, K.; U.S. Patent 5,531,925: 1996.
- (23) Ganem-Quintanar, A.; Quintanar-Guerrero, D.; Buri, P. *Drug Develop. Ind. Pharm.* **2000**, *26*, 809-820.
- (24) Popescu, G.; Barauskas, J.; Nylander, T.; Tiberg, F. *Langmuir* **2007**, *23*, 496-503.
- (25) Strashun, S. I.; U.S. Patent 2,557,155 assigned to USDA: 1951.
- (26) Larsson, K. *J. Phys. Chem.* **1989**, *93*, 7304-7314.
- (27) Larsson, K. *Z. Physik Chem. Neue Folge* **1967**, *56*, 173-198.
- (28) Larsson, K.; Gabrielsson, K.; Lundberg, B. *J. Sci. Fd. Agric.* **1978**, *29*, 909-914.
- (29) Larsson, K.; Lindblom, G. *J. Disp. Sci. Technol.* **1982**, *3*, 61.
- (30) Larsson, K. *Nature* **1983**, *304*, 664.
- (31) Hyde, S. T.; Andersson, S.; Ericsson, B.; Larsson, K. *Z. Kristallogr.* **1984**, *168*, 213-219.
- (32) Larsson, K. *Lipids — Molecular Organization, Physical Functions and Technical Applications.*; The Oily Press Ltd.: Dundee, 1994.
- (33) Chung, H.; Kim, J.; Um, J. Y.; Kwon, I. C.; Jeong, S. Y. *Diabetologia* **2002**, *45*, 448-451.
- (34) Chang, C. M.; Bodmeier, R. *Pharm. Res* **1994**, *11*.

- (35) Lopes, L. B.; Lopes, J. L. C.; Oliveira, D. C. R.; Thomazini, J. A.; Garcia, M. T. J.; Fantini, M. C. A.; Collett, J. H.; Bentley, M. *European Journal of Pharmaceutics and Biopharmaceutics* **2006**, *63*, 146-155.
- (36) Engstrom, S.; Ericsson, B.; Landh, T. *Proceedings of the Controlled Release Society* **1996**, 89-90.
- (37) Chang, C.; Bodmeier, R. J. *Controlled Release* **1997**, *46*, 215-222.
- (38) Boyd, B. J.; Whittaker, D. V.; Khoo, S. M.; Davey, G. *International journal of pharmaceutics* **2006**, *309*, 218-226.
- (39) Almsherqi, Z. A.; Kohlwein, S. D.; Deng, Y. *The Journal of Cell Biology* **2006**, *173*, 839-844.
- (40) Landh, T., Lund University, Sweden, 1996.
- (41) Landh, T. *FEBS letters* **1995**, *369*, 13-17.
- (42) Bouligand, Y. J. *Phys. Colloques* **1990**, *51*, 35-52.
- (43) Larsson, K.; Fontell, K.; Krog, N. *Chemistry and Physics of Lipids* **1980**, *27*, 321-328.
- (44) Luzzati, V. *Current opinion in structural biology* **1997**, *7*, 661.
- (45) Robins, R. K. *Pharmaceutical Research* **1984**, *1*, 11-18.
- (46) De Clercq, E. *Advances in Drug Research* **1988**, *17*, 1-59.
- (47) Herdewijn, P. *Antiviral research* **1992**, *19*, 1-14.
- (48) Chu, C. K.; Baker, D. C. *Nucleosides and nucleotides as antitumor and antiviral agents*; Plenum press New York, 1993.
- (49) Holý, A. *Advances in Antiviral Drug Design* **1994**, 179-232.
- (50) Lindblom, G. In *Advances in Lipid Methodology-Three*; Christie, W. W., Ed.; The Oily Press Ltd: Dundee, 1996; Vol. 7, chap. 5, p 133-210.
- (51) Liu, L.; John, V.; McPherson, G.; Maskos, K.; Bose, A. *Langmuir* **2005**, *21*, 3795-3801.
- (52) Bleasdale, T. A.; Tiddy, G. J. T. In *Organized Solutions*; Friberg, S. E., Lindman, B., Eds.; M. Dekker: New York, 1992; Vol. 44, p 125 and references therein.

- (53) Ambrosone, L.; Murgia, S.; Cinelli, G.; Monduzzi, M.; Ceglie, A. *J. Phys. Chem. B* **2004**, *108*, 18472-18478.
- (54) Nostro, P. L.; Murgia, S.; Lagi, M.; Fratini, E.; Karlsson, G.; Almgren, M.; Monduzzi, M.; Ninham, B. W.; Baglioni, P. *The Journal of Physical Chemistry B* **2008**, *112*, 12625-12634.
- (55) Keresztes, I.; Williard, P. G. *J. Am. Chem. Soc* **2000**, *122*, 10228-10229.
- (56) Razumas, V.; Talaiykt, Z.; Barauskasa, J.; Larsson, K.; Mieziš, Y.; Nylander, T. *Chemistry and physics of lipids* **1996**, *84*, 123-138.
- (57) Razumas, V.; Larsson, K.; Mieziš, Y.; Nylander, T. *J. Phys. Chem* **1996**, *100*, 11766-11774.
- (58) Giorgione, J. R.; Huang, Z.; Epand, R. M. *Biochemistry* **1998**, *37*, 2384-2392.
- (59) Briggs, J.; Chung, H.; Caffrey, M. *J. Phys. II France* **1996**, *6*, 723-751.
- (60) Qiu, H.; Caffrey, M. *Biomaterials* **2000**, *21*, 223-234.
- (61) Alberola, C.; Blümich, B.; Emeis, D.; Wittern, K. P. *Colloids Surf. A* **2006**, *290*, 247-255.
- (62) Chupin, V.; Boots, J. W. P.; Killian, J. A.; Demel, R. A.; Kruijff, B. d. *Biophys. J.* **2002**, *82*, 843-851.
- (63) Caboi, F.; Murgia, S.; Monduzzi, M.; Lazzari, P. *Langmuir* **2002**, *18*, 7916-7922.
- (64) Terao, T.; Matsui, S.; Akasaka, K. *J. Am. Chem. Soc.* **1977**, *99*, 6136-6138.
- (65) Scherer, P. G.; Seelig, J. *Biochemistry* **1989**, *28*, 7720-7728.
- (66) Andersson, S.; Hyde, S. T.; Larsson, K.; Lidin, S. *Chem. Rev.* **1988**, *88*, 221-242.
- (67) Czeslik, C.; Winter, R.; Rapp, G.; Bartels, K. *Biophysical Journal* **1995**, *68*, 1423-1429.
- (68) Pisani, M.; Bernstorff, S.; Ferrero, C.; Mariani, P. *J. Phys. Chem. B* **2001**, *105*, 3109-3119.
- (69) Conn, C. E.; Ces, O.; Squires, A. M.; Mulet, X.; Winter, R.; Finet, S. M.; Templer, R. H.; Seddon, J. M. *Langmuir* **2008**, *24*, 2331-2340.



- (70) Lendermann, J.; Winter, R. *Physical Chemistry Chemical Physics* **2003**, *5*, 1440-1450.
- (71) Kraineva, J.; Nicolini, C.; Thiyagarajan, P.; Kondrashkina, E.; Winter, R. *Biochimica et Biophysica Acta (BBA)-Proteins & Proteomics* **2006**, *1764*, 424-433.
- (72) Anderson, D. M.; Gruner, S. M.; Leibler, S. *Proceedings of the National Academy of Sciences of the United States of America* **1988**, *85*, 5364.
- (73) Turner, D.; Wang, Z. G.; Gruner, S.; Mannock, D.; McElhaney, R. *Journal de Physique II* **1992**, *2*, 2039-2063.
- (74) Chachaty, C.; Rainteau, D.; Tessier, C.; Quinn, P. J.; Wolf, C. *Biophysical journal* **2005**, *88*, 4032-4044.
- (75) Murgia, S.; Lampis, S.; Angius, R.; Berti, D.; Monduzzi, M. *J. Phys. Chem. B* **2009**, *113*, 9205-9215.
- (76) Israelachvili, J. *Intermolecular and Surface Forces 2nd Ed.*; Academic Press: San Diego, 1992.
- (77) Duesing, P. M.; Templer, R. H.; Seddon, J. M. *Langmuir* **1997**, *13*, 351-359.
- (78) Winter, R.; Erbes, J.; Templer, R. H.; Seddon, J. M.; Syrykh, A.; Warrender, N. A.; Rapp, G. *Physical Chemistry Chemical Physics* **1999**, *1*, 887-893.
- (79) Luzzati, V. In *Biological Membranes, Physical Facts and Function*; Chapman, D., Ed.; Academic Press: New York, 1968.
- (80) Rand, R. P.; Fuller, N. L. *Biophys. J.* **1994**, *66*, 2127-2138.
- (81) Coleman, J. E. *Annu. Rev. Biophys. Biomol. Struct.* **1992**, *21*, 441-483.
- (82) Aquino, M. A. S.; Lim, J.-S.; Sykes, A. G. *Chem. Soc., Dalton Trans.* **1992**, 2135-2136.
- (83) Bradford, D.; Das, A. K.; Egloff, M. P. *Annu. Rev. Biophys. Biomol. Struct.* **1998**, *27*, 133-164.
- (84) Bel'skii, V. E. *Russ. Chem. Rev.* **1977**, *46*, 828-841.
- (85) Florián, J.; Warshel, A. *J. Phys. Chem. B* **1998**, *102*, 719-734.
- (86) Benkovic, S. J. *Comprehensive Chemical Kinetics* **1972**, *10*, 1-56.
- (87) Nigou, J.; Dover, L. G.; Besra, G. S. *Biochemistry* **2002**, *41*, 4392-4398.

- (88) Klähn, M.; Rosta, E.; Warshel, A. *J. Am. Chem. Soc.* **2006**, *128*, 15310-15323.
- (89) Jongjoo, K.; Wenyun, L.; Weihong, Q.; Lijuan, W.; Caffrey, M.; Dongping, Z. *J. Phys. Chem. B* **2006**, *110*, 21994-22000.
- (90) Thomas, J. M.; Thomas, W. J. *Heterogeneous Catalysis*; VCH: Weinheim, 1997.
- (91) Mantsch, H. H.; Martin, A.; Cameron, D. G. *Biochemistry* **1981**, *20*, 3138-3145.
- (92) Nilsson, A.; Holmgren, A.; Lindblom, G. *Chemistry and Physics of Lipids* **1994**, *69*, 219-227.
- (93) Senak, L.; Davies, M. A.; Mendelsohn, R. *The Journal of Physical Chemistry* **1991**, *95*, 2565-2571.
- (94) Nilsson, A.; Holmgren, A.; Lindblom, G. *Chemistry and Physics of Lipids* **1994**, *71*, 119-131.
- (95) Razumas, V.; Talaikytė, Z.; Barauskas, J.; Miežis, Y.; Nylander, T. *Vibrational Spectroscopy* **1997**, *15*, 91-101.
- (96) Holmgren, A.; Lindblom, G.; Johansson, L. B. A. *The Journal of Physical Chemistry* **1988**, *92*, 5639-5642.
- (97) Hübner, W.; Mantsch, H. H. *Biophysical journal* **1991**, *59*, 1261-1272.
- (98) Razumas, V.; Niaura, G.; Talaikytė, Z.; Vagonis, A.; Nylander, T. *Biophys. Chem.* **2001**, *90*, 75-87.
- (99) Zimmermann, H. *Biochemical Journal* **1992**, *285*, 345-365.
- (100) Butcher, W. W.; Westheimer, F. H. *Journal of the American Chemical Society* **1955**, *77*, 2420-2424.
- (101) Govil, G.; Saran, A. *J. Theoretical Biology* **1971**, *32*, 399-406.
- (102) Ljusberg-Wahren, H.; Nyberg, L.; Larsson, K. *Chimica Oggi* **1996**, *June*, 40-43.
- (103) Neto, C.; Aloisi, G.; Baglioni, P.; Larsson, K. *J. Phys. Chem. B* **1999**, *103*, 3896-3899.
- (104) Monduzzi, M.; Ljusberg-Wahren, H.; Larsson, K. *Langmuir* **2000**, *16*, 7355-7358.

- (105) Talmon, Y. *Giant Micelles*; Zana, R., Kaler, EW, ed.; CRC Press: New York, 2007.
- (106) Caboi, F.; Nylander, T.; Razumas, V.; Talaikyte', Z.; Monduzzi, M.; Larsson, K. *Langmuir* **1997**, *13*, 5476-5483.
- (107) Caboi, F.; Amico, G. S.; Pitzalis, P.; Monduzzi, M.; Nylander, T.; Larsson, K. *Chem. Phys. Lipids* **2001**, *109*, 47-62, and references therein.
- (108) Landh, T. *J. Phys. Chem.* **1994**, *98*, 8453-8467.
- (109) Gustafsson, J.; Ljusberg-Wahren, H.; Almgren, M.; Larsson, K. *Langmuir* **1996**, *12*, 4611-4613.
- (110) Murgia, S.; Caboi, F.; Monduzzi, M. *Chem. Phys. Lipids* **2001**, *110*, 11-17.
- (111) Diaz, G.; Melis, M.; Batetta, B.; Angius, F.; Falchi, A. M. *Micron* **2008**, *in press*.
- (112) Diaz, G.; Batetta, B.; Sanna, F.; Uda, S.; Reali, C.; Angius, F.; Melis, M.; Falchi, A. M. *Histochem. Cell Biol.* **2008**, *129*, 611-621.
- (113) Fields, R. D.; Lancaster, M. V. *Am. Biotechnol. Lab.* **1993**, *11*, 48-50.
- (114) Angius, R.; Murgia, S.; Berti, D.; Baglioni, P.; Monduzzi, M. *J. Phys.: Cond. Matter* **2006**, *18*, S2203-S2220.
- (115) Borné, J.; Nylander, T.; Khan, A. *Langmuir* **2001**, *17*, 7742-7751.
- (116) Evans, D. F.; Wennerstrom, H. *The colloidal domain: where Physics, Chemistry, Biology, and Technology meet*; VCH Publish.: New York, 1994.
- (117) Kabanov, A.; Batrakova, E.; Alakhov, V. *Adv. Drug deliv. Rev.* **2002**, *54*, 759-779.
- (118) Fatma, S.; Yakubov, R.; Anwar, K.; Hussain, M. M. *J. Lipid Res.* **2006**, *47*, 2422-2432.
- (119) Yang, Y. M.; Wu, K. C.; Huang, Z. L.; Chang, C. H. *Langmuir* **2008**, *24*, 1695-1700.
- (120) Ferreira, D. A.; Bentley, M.; Karlsson, G.; Edwards, K. *International journal of pharmaceutics* **2006**, *310*, 203-212.
- (121) Nagayasu, A.; Uchiyama, K.; Kiwada, H. *Advanced drug delivery reviews* **1999**, *40*, 75-87.

- (122) Johnsson, M.; Barauskas, J.; Tiberg, F. *J. Am. Chem. Soc.* **2005**, *127*, 1076-1077.
- (123) Uyama, M.; Nakano, M.; Yamashita, J.; Handa, T. *Langmuir* **2009**, *25*, 4336-4338.